Dissertation

submitted to the

Combined Faculties of the Natural Sciences and Mathematics
of the Ruperto-Carola University of Heidelberg, Germany

for the degree of

Doctor of Natural Sciences

Put forward by

Veronica Pizzella

born in: Rome

Oral examination: 3rd November 2021

Sub-ppb xenon purity control and study of PTFE surface contamination towards the first results of XENONnT

1st Referee: Prof. Dr. Dr. h.c. Manfred Lindner
2nd Referee: Jun.-Prof. Dr. Loredana Gastaldo

Abstract

Abstract The XENONnT experiment, successor of XENON1T, aims at probing the cross sections of the interaction between a WIMP, a well-motivated dark matter candidate, and a xenon nucleus down to 1.4×10^{-48} cm^2; in addition, it will allow to distinguish if the electronic event excess observed by XENON1T was due to new physics or a new standard model background. XENONnT employs 8.5 tonnes of xenon in a dual-phase Time Projection Chamber (TPC) and it needs both ultra-pure xenon and an ultra-low background for increasing the sensitivity. Some of the impurities of concern are: radioactive impurities such as ^{85}Kr, ^{222}Rn and its progenies, and ^{3}H, since they increase the background rate; electronegative impurities such as oxygen, since they reduce the amount of electrons in the TPC.

In the first part of this thesis, we present an offline purity monitor, able to detect trace impurities at sub-ppb level. The setup uses a combination of Atmospheric Pressure Ionization Mass Spectrometry (APIMS), with a commercial APIX dQ from ThermoFisher, and a custom-made gas chromatography setup. The setup is used to measure xenon samples from the start of the science run of XENONnT. First results are given on oxygen and hydrogen contamination of the gaseous phase. In the second part, a study of deposition of ^{222}Rn daughters on Polytetrafluoroethylene (PTFE) is presented. The study was conducted in the framework of the assembly of the XENONnT TPC, as PTFE is the most abundant material. Results are given for several PTFE samples that were deployed during the XENON1T TPC construction phase.

Zusammenfassung Das XENONnT-Experiment, der Nachfolger von XENON1T, hat sich die Untersuchung des Wirkungsquerschnitts von Wechselwirkungen zwischen einem WIMP, welches ein gut motivierter Dunkle-Materie-Kandidat ist, und einem Xenon-Atomkern bis hin zu Werten so klein wie $1,4 \times 10^{-48}$ cm^2 zum Ziel gesetzt. Desweiteren wird das Experiment es ermöglichen, zu bestimmen, ob der von XENON1T beobachtete Überschuss an Elektronrückstoßereignissen von neuer Physik oder von einem bislang nicht berücksichtigten Standardmodell-Untergrund verursacht wurde. XENONnT beinhaltet 8,5 Tonnen Xenon in Zweiphasen-Zeitprojektionskammern (TPCs) und benötiget sowohl außergewöhnlich reines Xenon als auch außergewöhnlich kleine Untergrundraten, um eine höhere Sensitivität erreichen zu können. Einige der relevanten Verunreinigugnen sind radioaktive Verunreinigungen wie ^{85}Kr, ^{222}Rn und seine Töchter sowie ^{3}H, da diese zur Untergrundrate beitragen. Dazu kommen elektronegative Verunreinigungen wie Sauerstoff, weil diese die Anzahl der Elektronen in der TPC reduzieren.

Im ersten Abschnitt dieser Dissertation wird ein Reinheits-Überwachungsdetektor vorgestellt, der in der Lage ist, Spuren von Verunreinigungen zu messen, die unterhalb einer Größenordnung von 1 ppb liegen. Der Detektor verwendet eine Kombination aus Atmosphärendruck-Ionisations-Massenspektrometrie (APIMS), für die ein kommerzielles APIX dQ von ThermoFisher verwendet wird, und einem individuell gefertigten Gaschromatographie-Aufbau. Der Detektor wird verwendet, um Xenon-Proben aus der Zeit der ersten XENONnT-Datennahmeperiode zu untersuchen. Es werden erste Resultate bezüglich der Verunreinigung der Gasphase mit Sauerstoff und Wasserstoff vorgestellt. Im zweiten Abschnitt wird eine Studie über die Ablagerung von ^{222}Rn-Töchtern auf Polytetrafluorethylen (PTFE) vorgestellt. Die Studie wurde im Kontext des Zusammenbaus der XENONnT-TPC durchgeführt, da diese vor allem aus PTFE besteht. Es werden Resultate für mehrere PTFE-Proben präsentiert, die während der Konstruktionsphase der XENONnT-TPC eingesetzt wurden.

Contents

Chapter 1

Physics case for dual-phase xenon detectors

The Standard Model of Particle Physics (SM) is a theory that is very successful in describing many physical phenomena that we observe. The last of its success is the measurement of the Higgs boson, postulated by, among other, Peter Higgs in 1964 [1], and finally observed at the Large Hadron Collider (LHC) at CERN in 2012 [2, 3].

Despite all the succesfull predictions of the SM, there are however some areas of physics where it is not able to provide a satisfactory explanation. In this chapter we explore some of the challenges unanswered by the SM in the topic of rare-events: dark matter, axions and the magnetic moment of neutrinos.

1.1 Dark matter

The name "Dark matter" was first invented by by Fritz Zwicky in 1933 when he found that some mass was missing from the Coma galaxy cluster [4]. Zwicky used the Doppler effect to calculate the velocity of the stars and the virial theorem to extrapolate the total mass. His calculation yielded a total value of the mass higher than the observed mass of the Coma galaxy cluster, leading him in defining a missing mass in opposition of the baryonic matter which is light emitting.

Since the first postulation from Zwicky, many other evidences of missing matter have led to the inclusion of Dark Matter in the current cosmological model, the Lambda Cold Dark Matter (ΛCDM) model. The first observations by Zwicky for the Coma galaxy cluster have been repeated for many other galaxies. In addition, the rotational velocity of the stars in these galaxies present the same missing mass problem as in the Coma galaxy cluster [5], which can easily be explained if inside the galaxies there is a halo of non-light-emitting mass, i.e., a dark matter halo (see figure 1.1).

A similar missing mass problem is also seen in clusters of galaxies. One of the most famous example is the Bullet cluster, in figure 1.2 [6]: this cluster is formed by the collision of two separate clusters, each formed by galaxies (that act as collisionless particles) and plasma (which slows down due the electromagnetic interaction). Since most of the mass of a

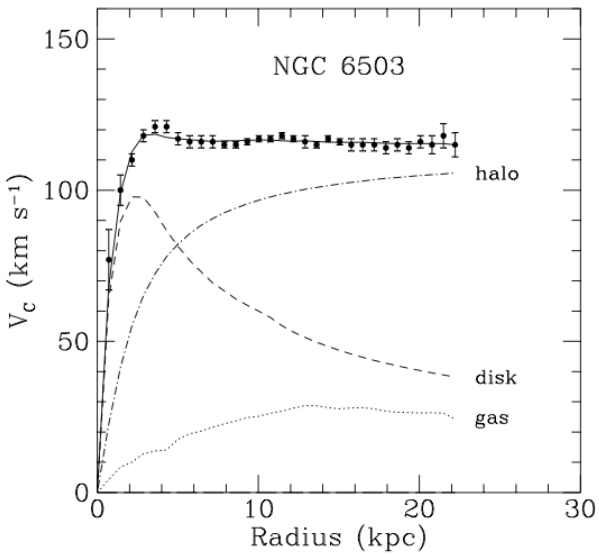

Figure 1.1.: Star rotational velocity distribution of the galaxy NGC 6503. The star velocities (black dots) do not follow the expected profile from the visible matter (dashed and dotted lines). A missing halo (dashed-dotted line) is needed to explain fully the profile. Figure taken from [5].

galaxy cluster lies in the plasma between galaxies, one would expect that the reconstructed the mass profile (using gravitational lensing) would follow the plasma (measured with X-rays). Instead, the mass profile is more similar to the one of the galaxies, which is a strong indication that an additional mass component exists. In addition, this missing mass does not interact strongly either with normal matter (the gas), nor with itself, and acts instead similar to the collisionless galaxies. Another successful prediction of the ΛCDM model are the measurements of the anysotropies of the Cosmic Microwave Background (CMB). The CMB is the relic photon radiation from the last scattering surface from the Big Bang. It has a spectrum of a black body with temperature 2.726 K [8], but it has very small anisotropies with order of magnitude 10^{-5} K [9].

Several experiments measure and fit the power spectrum of the anysotropies, and from the parameters of the ΛCDM model are calculated, including the density of baryonic matter, dark matter and dark energy. Figure 1.3 shows the latest data from the Planck collaboration, from which it is calculated that the density of baryonic and dark matter are $\rho_b = 4.5 \pm 0.5\%$ and $\rho_{DM} = 27.0 \pm 0.5\%$ respectively, making dark matter ~ 5 times more abundant than baryonic matter [10].

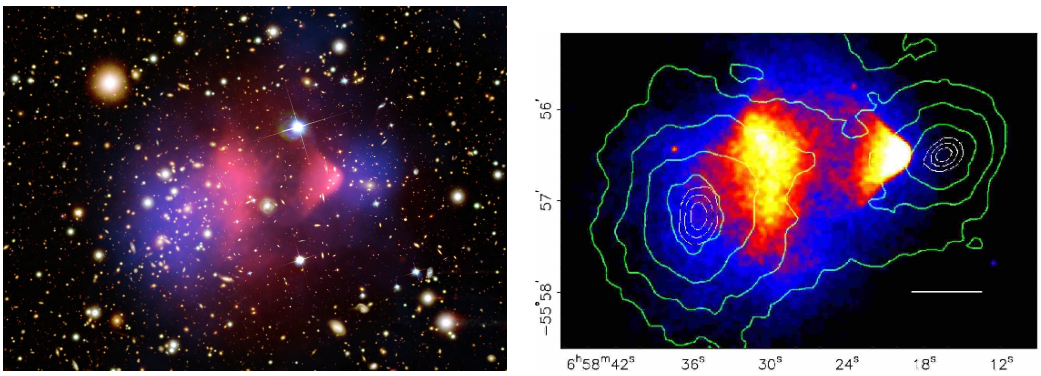

(a) (b)

Figure 1.2.: Left: artistic reconstruction of the bullet cluster from [7]. Right: the color scale indicates the plasma mass from X-rays, the green contours are the mass distribution reconstructed from weak gravitational lensing. Its center of mass is closer to the galaxies than to the plasma. Figure from [6].

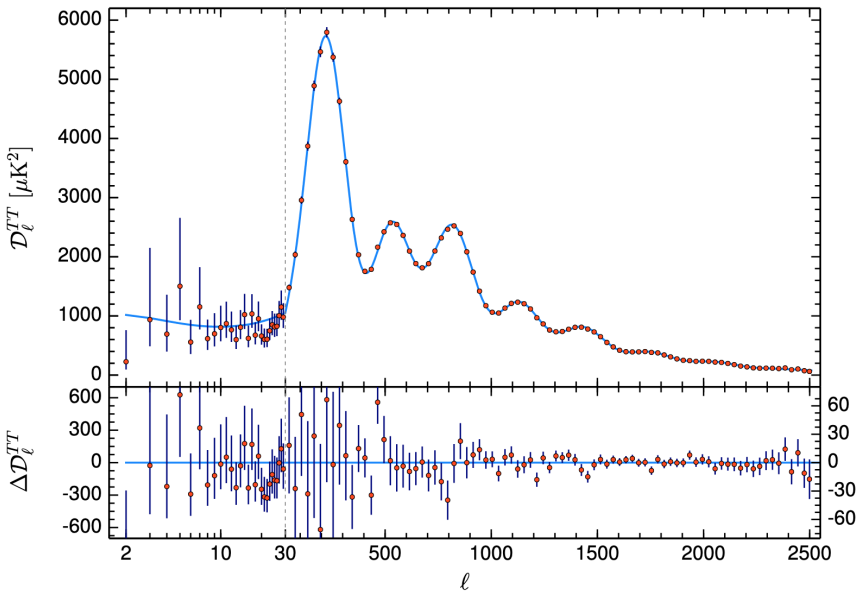

Figure 1.3.: Temperature power spectrum from the Planck collaboration [10]. The ΛCDM model theoretical spectrum is fitted (solid line) and used to compute the density of baryonic and dark matter.

1.1.1 Dark Matter candidates

Although there are proposal to modify the theory of general relativity to explain the astronomical and cosmological observations [11], a new particle would fit the best all the evidence for the missing matter. This new particle, or class of particles, must have the following characteristics:

- From the observations of the CMB, we know it is produced in the early universe.
- We see its effects until today, so it must be stable, or at least its lifetime must be longer than the age of the universe.
- It must interact gravitationally.
- It must not interact electromagnetically or strongly.
- It can at most interact weakly.
- Most of dark matter particles must have velocities $< 10^8 c$ (the so called "cold dark matter").

In addition, we know that dark matter clusters where baryonic matter also clusters. This is a consequence that dark matter is gravitationally attracted to baryonic matter. In fact, it is assumed that dark matter "helps" binding galaxies gravitationally, and therefore the velocity requirement is calculated from the formation of galactic structures [12].

Comparing the listed required properties with the 61 particles of the SM, the only particle that would fit all of them at first sight are neutrinos. Although the SM predicts massless neutrinos, we know from observing neutrino oscillation that they are massive [13], albeit their mass is very small (< 0.120 eV from cosmological constraints [14]). However, neutrinos can not fully fulfil the dark matter role for two reasons: the first is that they have speeds really close to the speed of light, which would make them a "hot dark matter" candidate. The second reason is that their total mass is too low and their phase space density[1] does not allow them to reach the necessary number density to reach the measured dark matter density. In conclusion, no particle in the SM can completely make up dark matter, which brings the hunt to particles beyond the standard model.

Some suggested dark matter candidates are the axions (which will be described in more details in section 1.2) and axion like-particles, sterile neutrinos (which are postulated to explain the masses of neutrinos [15]) and, most promising, WIMPs. We use the term Weakly Interactive Massive Particle (WIMP), denoted with the letter χ, to define a theoretical class of particles that comprise several candidates which fullfil all the requirements of a dark matter particle.

WIMPs are created in the early universe in the radiation dominated era [16, Ch. 7], in thermal equilibrium with baryonic matter. With the expansion of the universe, the temperature of the primordial plasma became too small to generate new WIMPs and at the same time their number density n_χ decreased. When n_χ was sufficiently low, the reaction rate with baryonic matter dropped and they "freeze-out", causing n_χ to stay constant.

To the WIMP category belong all the candidates from supersymmetry, the lightest one being the neutralino, the grativino and Kaluza-Klein particles. For a review of dark matter candidates, see [17]. For the remainer of this work, when we talk about a dark matter particle, we assume it is a WIMP.

[1] Neutrinos are fermions, which means that, from quantum mechanics, there is a limit on how many it is possible to fit in a finite volume.

1.1.2 Dark Matter detection

There are three paths to detect dark matter, assuming its interaction is not exclusively gravitational. Figure 1.4 sketches the paths: dark matter production(1), dark matter indirect detection (2) and dark matter direct detection(3). In this section, we focus on the two former methods, while the latter will be detailed in section 1.1.3.

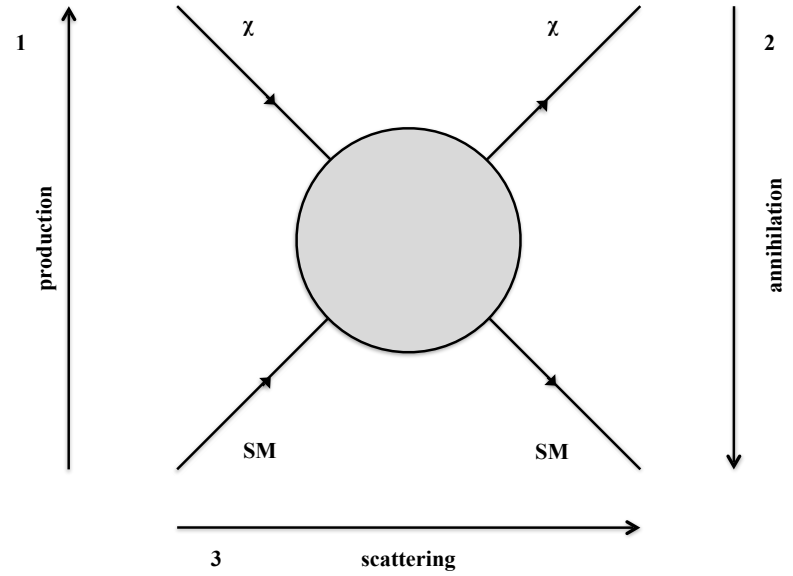

Figure 1.4.: Dark matter (χ) interaction with a SM particle. The three paths are indicated by the three arrows.

Dark matter production It is possible to produce dark matter by artificially recreating a similar environment as the one when they were first produced during the early universe. This dark matter creation is possible at particle colliders only at very high energy and it is done at LHC at CERN. The signature of the creation of a dark matter particle is missing energy after a collision. For a review of the current LHC searches, see [18]. This kind of searches comes with the caveat that it is not possible to measure the half-life of a particle created in such a manner, so it is not possible to verify one of the main requirements.

Dark matter indirect detection Although the average number density n_χ is too low for dark matter particles to find each other, dark matter particles are not equally distributed in the universe. Since they interact gravitationally, we expect that areas where the baryonic matter is very dense will also have a higher dark matter density. If it is high enough, there is the possibility of annihilation of two dark matter particles into SM particles. In addition, if a part of dark matter is composed of long-lived but unstable particles, there is the possibility that they decay in a stable state generating SM particles. The signature of dark matter would then be an unexpected flux of neutrinos, photons or particle-antiparticle couples. Several experiments have been looking for such signatures in

high density places, such as the Sun, the galactic halo and the galactic center. For this class of experiment, it is crucial to have a precise calculation of the flow of SM particles arising from SM processes. For a review of current indirect detection experiments, see [19].

1.1.3 Dark matter direct detection

The main focus of this work is the scattering of a WIMP particle on a SM target. We know from the star velocity observations that Earth is immersed in a dark matter halo, so we can try to detect the recoil of a standard model particle with a dark matter particle. The differential event rate of a WIMP(χ)-SM nucleus scattering per transferred energy can be written ([16, Ch. 17]):

$$\frac{\mathrm{d}R}{\mathrm{d}E} = N_N \frac{\rho_\chi}{m_\chi} \int_{v_{min}}^{v_{max}} \frac{\mathrm{d}\sigma}{\mathrm{d}E} v f(v)\, \mathrm{d}v\, \mathrm{d}E \tag{1.1}$$

Some of the parameters of equation 1.1 are depending only on the nature of a WIMP, such as its mass m_χ and its density in the milky way halo ρ_χ. Other parameters are astronomical constraints, such as v_{max}, the maximum velocity that a WIMP can have, which is the escape velocity from the milky way halo. Finally, some parameters depend on the target employed: N_N is the total number of target nuclei, which means that to boost the event rate it is very important to have as many nuclei as possible, and v_{min} is the minimum velocity required for a WIMP to cause a recoil of energy E and it varies for each kind of target employed.

We are interested in the differential cross section $\mathrm{d}\sigma/\mathrm{d}E$. Since the mass of a WIMP m_χ is unknown, the cross section is usually given as a function of the mass itself. It also depends on the interaction taken into account. The main focus is on the spin-independent scattering. In this case, for a nucleus with Z protons and $(A - Z)$ neutrons:

$$\sigma \simeq \frac{4\mu^2}{\pi} [Z f_p + (A - Z) f_n]^2 \tag{1.2}$$

where f_p and f_n are the WIMP couplings to protons and neutrons and μ is the reduced mass.

$$\frac{1}{\mu^2} = \frac{1}{m_\chi^2} + \frac{1}{M_n^2}$$

From equation 1.2, it is possible to see that a high atomic mass A and atomic number$Z$ lead to a bigger cross section, which is why, among other reasons, a heavy atom like xenon is a commonly used target for direct detection. For spin-dependent interaction, an extra term due to the spin needs to be taken into account, which lowers the cross section by around one order of magnitude.

Once a WIMP hits a nucleus, it can cause three type of signals:

- photons from the excitation of the nucleus;
- electrons from the ionization of the nucleus;
- phonons from the vibration of the nucleus.

Different experiments employ one or more channels in order to detect a nucleus recoil. In addition, other signatures can be used to discriminate for dark matter interaction, such as the annual modulation of the signal, the directionality of the collisions and the energy distribution. For a review about direct detection experiments, see [20].

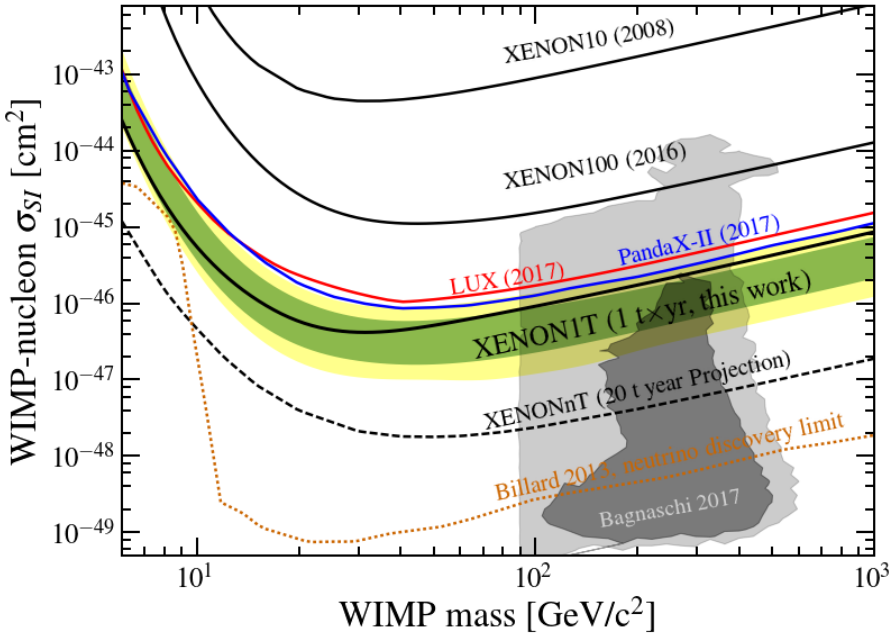

Figure 1.5.: Most updated limits for spin-independent scattering of WIMP-SM nucleus. Figure taken from [21].

The current status of WIMP direct detection is shown in figure 1.5. All the experiments featured employ Liquid xenon (LXe) as active target. So far, no WIMP has been detected, which means that every line is excluding the signal region above it. The limit of direct detection is a physical one: eventually, those experiments will become so sensitive that they will start detecting atmospheric neutrinos (orange line). At low energy, already the current detector generation is sensitive enough to detect solar neutrinos (the peak at low masses of the orange line). This background, the "neutrino fog", represents the final limit that it is possible to achieve with direct detection.

1.2 Axions

The axion is a beyond the standard model particle that arise from the Peccei-Quinn theory, formulated in 1977 to solve the strong CP problem of the Standard Model [22]. The strong CP problem is the fact that in the SM the Quantum Chromodynamics (QCD) is theoretically not expected to preserve the Charge-Parity (CP) symmetry. The CP-violating term however includes an angle, θ, that is not fixed by the SM theory and it has to be experimentally measured (as for most of the SM couplings). The way to quantify θ is by measuring the neutron electric dipole moment (nEDM) (d_n). However, experimentally no

nEDM has been observed, and at this point it is only possible to constrain its value to [23]

$$d_n < 0.13 \times 10^{-25} \text{e cm}$$

which leads to a θ of the order of 10^{-10}, virtually 0.

The Peccei-Quinn theory solves this puzzle by postulating the existence of a new global $U(1)$ symmetry which is spontaneously broken and generate a new massive pseudoscalar particle: the axion [24, 25]. As a light and massive particle, axions are good candidate for dark matter. Similarly to WIMPs, they are postulated to be produced in the early universe, but they would disperse energy until today, making them a cold dark matter candidate [16, Ch. 11].

Axions are theorized to couple with SM particles (photons, electrons, protons, neutrions, ...) with different coupling strenghts ($g_{a\gamma}$, g_{ae}, g_{ap}, g_{an}, ...). All the factors g are proportional to the axion mass m_a. The original Peccei-Quinn theory predicted g to be of the order of the electroweak scale, but this has since been ruled out experimentally. There are however more axion models that predict lighter axions which are still consistent with the current axion limits [26].

Many experiments are searching for axions with different detection techniques. Similarly to WIMPs, it is either possible to detect axions created in laboratories (the so called "light shining through a wall" experiments) or try to detect them from astronomical sources like the Sun (the "axion helioscopes"), or dark matter axions present in the galaxy halo ("axion haloscopes"). The creation and detection techniques exploit the Primakoff effect, which is the conversion of axions in photons when a strong magnetic field is present [27]. So far, despite the efforts, axions have not been observed, and the limits on their coupling strength varies over more than 20 orders of magnitudes of their mass (see figure 1.6). For a review of current axion experiments, see [28].

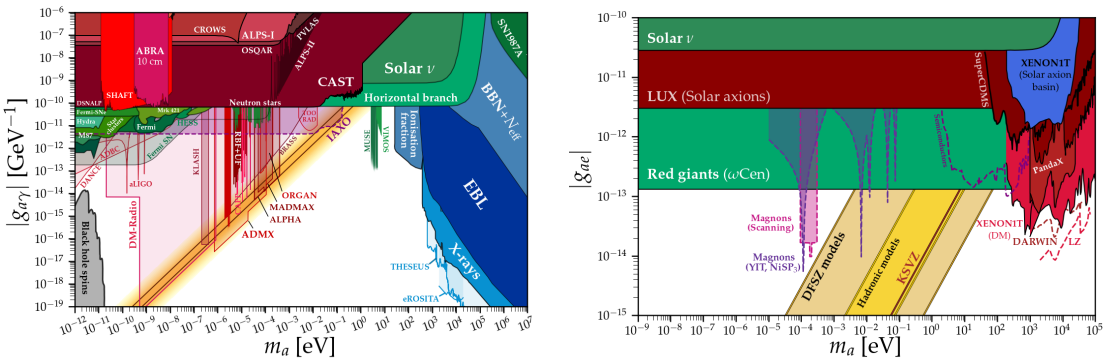

(a) (b)

Figure 1.6.: Coupling of axions with photons (left) and electrons (right). The solid color regions are existing experiments and the transparent regions are proposed and future experiments. Figure made with [29].

1.3 Neutrino magnetic moment

The SM predicts massless neutrinos, but we know from the observations of neutrino oscillations that this is not the case [13]. If the neutrinos have a mass, they also have have a (small) magnetic moment. The expectation is that the neutrino magnetic moment $\mu_\nu \sim 10^{-20} \times \mu_B$, where μ_B is the Bohr magneton [30]. The current best constraints come from indirect observations of stellar evolution and stands at $\mu_\nu < 2.6 \times 10^{-12} \mu_B$ [31]. A possible observation from XENON1T will be detailed in section 2.2.1.

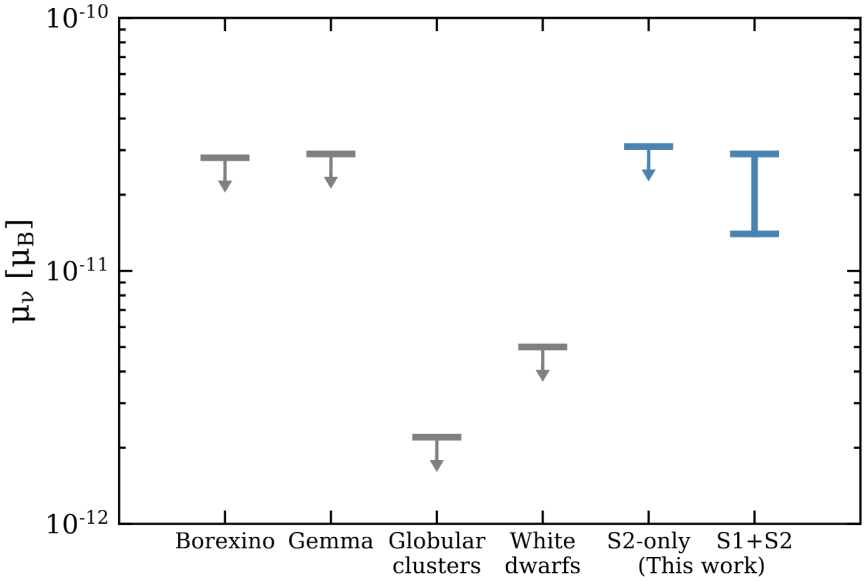

Figure 1.7.: Most updated measurements of the neutrino magnetic moment. The two right-most measurements (labelled "this work" in the plot) are the direct measurements from XENON1T, in tension with the indirect stellar evolution constraints. Figure taken from [32].

Chapter 2

Rare events searches with the Xenon experiments

The cross section of the beyond the standard model searches presented in 1 is expected to be at best of the order of the electro-weak interaction. In constructing a detector for such rare events, two factors come into play:

1. The target mass must be very large, in order to boost the new physics-standard model interaction rate.

2. The well-known SM physics must be completely under control and as low as possible, to make sure that any observed event is due to new physics.

In this regard, LXe is a very good candidate for a detector target. It is a noble gas, which means that it is not chemically reactive, and it is very stable. With a density of ~ 3 g/cm^3 when liquid, it provides a lot of mass in a relatively compact space, which both enhances the rate of a rare event and provides stopping power against external radiation. LXe has been successfully employed by the Xenon collaboration to build several detectors aimed at measuring the WIMP-SM cross section, using a dual-phase LXe and Gaseous xenon (GXe) Time Projection Chamber (TPC).

In this chapter, we explain in detail the working principle of dual-phase LXe and GXe TPC for detecting rare events (section 2.1). As this work is carryed on for the Xenon colaboration, a description of the Xenon detectors will be given in section 2.2. Finally, section 2.3 will discuss the most important "boring" physics, or backgrounds, for the Xenon experiments.

2.1 Dual-phase Time Projection Chamber working principle

When a xenon atom is hit by an external particle, the atom can get excited ($Xe^{\star}$) and/or ionized (Xe^{+}). Excited xenon will decay emitting scintillation light:

$$\begin{aligned} Xe^{\star} + Xe &\rightarrow Xe_2^{\star} \\ Xe_2^{\star} &\rightarrow 2Xe + h\nu \end{aligned}$$

where $h\nu$ is the light quanta output. Ionized xenon generates both electrons from the ionization and photons from the recombination:

$$\begin{aligned} Xe^{+} + Xe &\rightarrow Xe_2^{+} \\ Xe_2^{+} + e^{-} &\rightarrow Xe^{\star\star} + Xe \\ Xe^{\star\star} &\rightarrow Xe^{\star} + \text{heat} \\ Xe^{\star} + Xe &\rightarrow Xe_2^{\star} \\ Xe_2^{\star} &\rightarrow 2Xe + h\nu \end{aligned}$$

LXe is transparent to the light it emits, which means that it is possible to build a large LXe mass and place light detectors outside the LXe volume.

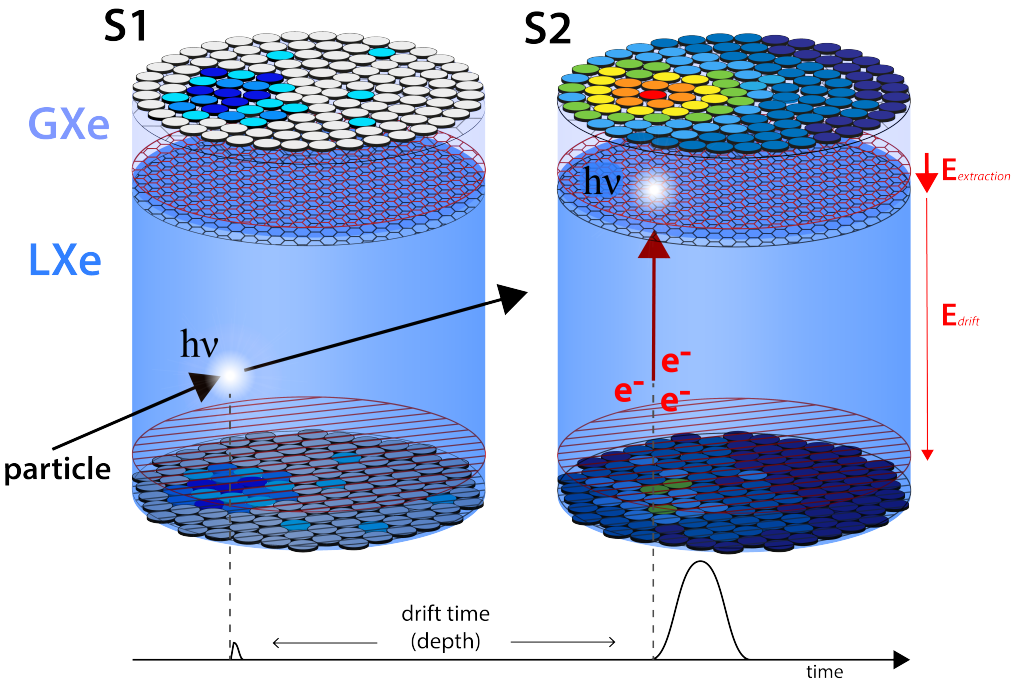

Figure 2.1.: Artistic depiction of the TPC working principle for XENON1T. A particle hitting a xenon atom generates scintillation light (left) and ionization electrons (right). The electron drift time allows to reconstruct the depth of the interaction (bottom). The Photo multiplier tubes (PMTs) pattern give the (x, y) position (top). Figure taken from [33].

The LXe target and is placed in a cylindrical vessel, usually constructed with stainless steel (see figure 2.1 for an artistic depiction). The light is detected by two arrays of photo multiplier tubes (PMTs), located at the top and at the bottom of the target. The first prompt signal from scintillation is called S1. Additionally, an electric field is applied in the vertical direction, drifting the electrons upwards towards the gaseous phase. At the liquid-gas interface, a second stronger electric field extracts the electrons, causing a cascade that proportionally multiplies photons. This second signal is called S2. Knowing the electric field, it is possible to measure the depth of the interaction, while from the PMTs hit pattern distribution it is possible to reconstruct the (x, y) position of the first interaction, allowing for a full 3-d reconstruction. This is crucial to exploit the self-veto properties of xenon: most of the backgrounds are expected to be external, meaning that by reconstructing the position of the hit, we can exclude the outermost xenon layer and reduce the rate of background events.

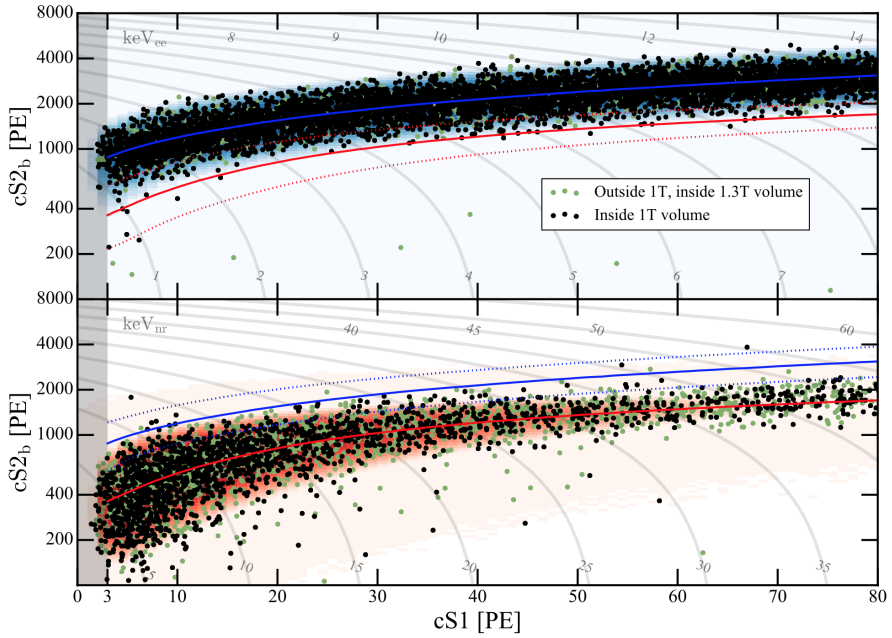

Figure 2.2.: Example of electronic recoil (top) and nuclear recoil (bottom) bands generated with an electronic recoil and nuclear recoil calibration source in XENON1T. Both S1 and S2 need to be corrected for detector artifacts, and the corrected signals are called cS1 and cS2. The median fit for the electronic and nuclear bands are in blue and red respectively. The grey curved lines represent the reconstructed total energy of each recoil. Figure taken from [34].

A second important feature of this design is the fact that a recoil happening on the nucleus of an atom and one happening on the electronic shell have a different S1/S2 ratio. For WIMPs we expect only nuclear recoil, while most of the backgrounds, as well as axions and neutrino scattering, have electronic recoil. This separation proves very important in reducing and identifying signals and backgrounds. Figure 2.2 shows the different distribution in space of S1 and S2 for electronic and nuclear recoil (from

calibration data). Since there is a partial overlap of the two bands, reducing the electronic background is an important task for increasing the sensitivity to a WIMP recoil.

2.1.1 Electron life-time

As illustrated so far, the secondary S2 signal is pivotal for the functioning of this type of TPC. It is very important that the electrons are able to reach the liquid-gas interface, which means that they have to survive in the LXe long enough to be able to travel to the surface. This survival time, or "electron life-time" τ_e as it is usually referred to, depends on the type of molecules an electron sees while it is drifting.

Xenon, as a noble element, is not reactive, thus the applied electric field is strong enough that the electron-xenon attachment rate negligible. However, if an electron meets another more reactive atom or molecule, it has a chance to get attached. This has the consequence of reducing the intensity of S2 signals and eventually making them disappear altogether. The deeper the initial scattering happens in the TPC, the more severe this problem is.

For most of dual-phase TPC experiments, we expect that the biggest contaminants of the system are the ones found in air (nitrogen, oxygen, argon, water, ...). Since the most electronegative is oxygen, it is assumed to be the main driver for the electron life-time. It is possible to define a relation between the electron life-time and the concentration of oxygen-equivalent impurities in xenon [35].

$$\tau_e = \frac{1}{N_{O_2} \cdot k_{O_2}} \tag{2.1}$$

Where N_{O_2} is the concentration of oxygen in mol(O_2)/liter(Xe) and k_{O_2} is the electron attachment rate to oxygen. k_{O_2} depends on the field applied in the LXe and is measured in [36].

2.2 The XENON experiments

The TPC working principle illustrated in section 2.1 was successfully employed by the XENON collaboration to probe the cross section of a hypothetical WIMP-SM particle scattering. The first experiment, XENON10, had a total active target of 15 kg of LXe and sucessfully set the lowest constrains at the time, setting an upper limit for the scattering of a WIMP with mass 30 GeV/c^2 at 4.5×10^{-44}cm^2 [37]. The next detector, XENON100, increased the total active mass to 65 kg and had a fiducial volume of 48 kg, which allowed, together with material screening [38], to improve the constraint for the cross section up to 1.1×10^{-45}cm^2 for a WIMP with mass 50 GeV/c^2 [39]. Its successor, XENON1T, has been decommissioned in 2019 to make space for the last detector XENONnT. This work is framed in the XENON1T and XENONnT experiments, so a more detailed description is given in the next sections.

One last mention goes to DARWIN, the "ultimate dark matter detector" [40]. This experiment plans to use 50 tonnes of xenon, of which 40 are in the active volume, with the goal to reach sensitivities up to the neutrino fog.

2.2.1 XENON1T

XENON1T is the third detector from the XENON collaboration. A detailed description is given in [41], and, during its life-time, provided several important results, both on dark matter [21, 42–44], neutrino physics [45] and other rare event searches [32]. Here we highlight the most important systems and results for this work.

XENON1T has a total inventory of 3.3 tonnes of xenon, of which 2 are in the active target and 1.3 in the fiducial volume. The extra xenon not employed in the target is used both for extra shielding and as a buffer for the xenon purification loop. The TPC has a cylindrical shape with 96 cm diameter and 97 cm height. The walls of the TPC are composed of 24 Polytetrafluoroethylene (PTFE) panels. PTFE is the material of choice for its high purity and reflectivity. In order to improve the reflectivity, the uppermost surface layer of the PTFE of the panels is removed using diamond tools, leaving a very smooth and reflective surface. The top and bottom of the cylinder are closed by two PMT arrays, the top with 127 PMTs and the bottom with 121. Both the arrays are covered with a PTFE plate between the PMTs windows. An electric field is applied in the LXe through a series of electrodes (cathode at the bottom of the TPC and anode at the top) and a series of field shaping rings along the length of the TPC. Figure 2.3a shows a sketch of the TPC.

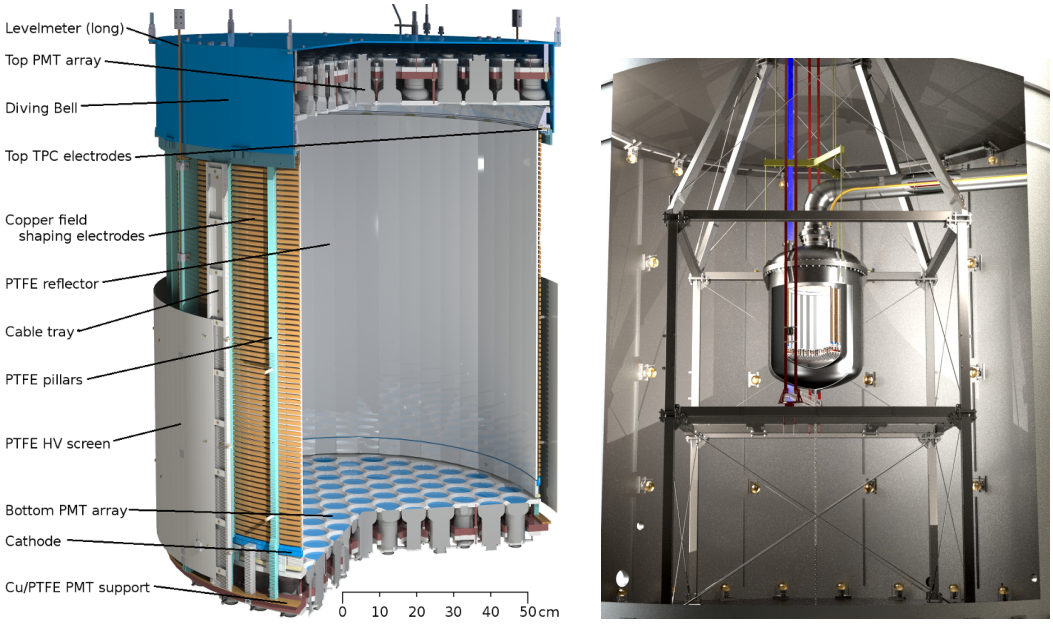

(a) (b)

Figure 2.3.: Left: rendering of the XENON1T TPC. Right: rendering of the cryostat in the water tank. Figures taken from [41].

The TPC is contained in a double cryostat which is vacuum insulated. The whole structure is suspended in the middle of a water tank for background reduction (see 2.3.1) and all the cables and pipes are contained in a big tube at the top of the cryostat. This includes all the signal and high voltage cables for the PMTs, the electrode cables and the

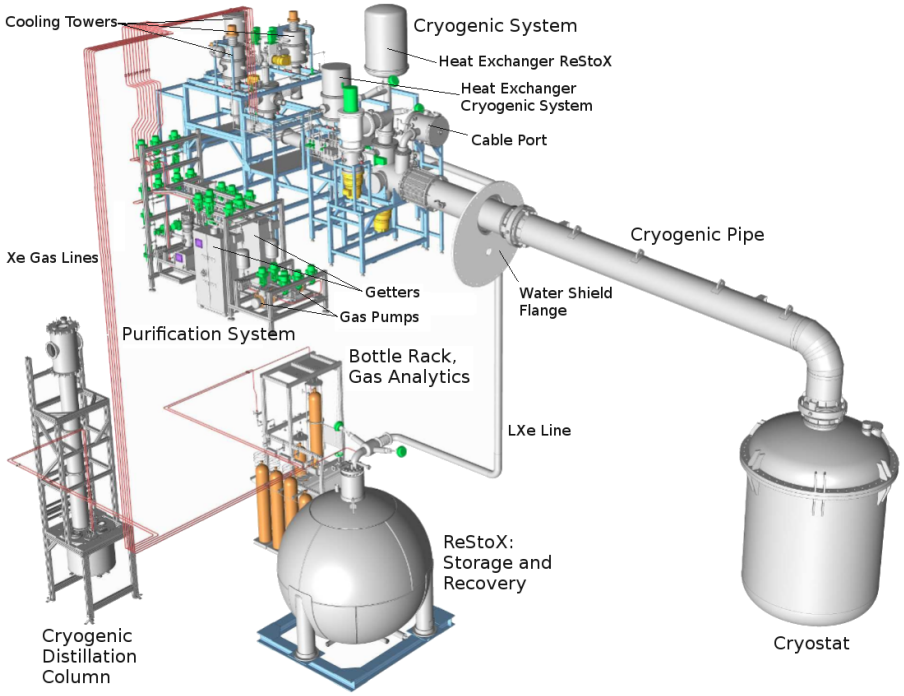

Figure 2.4.: Render of the gas system of XENON1T. Figure taken from [41].

pipes used for the flow of the xenon itself. A rendering of the TPC in the water tank can be seen in figure 2.5.

The XENON1T gas system is comprised of several subsystems that will be listed below. A rendering of the system is shown in figure 2.5.

Cryogenics It includes all the systems to liquify and keep the xenon cool. The temperature is controlled with two redundant pulse-tube refrigerators (PTRs).

Purification It contains the gas purifier system with two high-temperature rare-gas purifiers (getters) as well as the recirculation pumps. It works also as the main distribution system of xenon among the following subsystem.

Distillation column This column is used at the beginning of the science run to distill krypton from xenon (see 2.3.2).

ReStoX The Recovery and Storage of Xenon system (ReStoX) is used both for fast cooling of xenon and for fast recovery in case of emergency.

The electron life-time was constantly monitored during the life-time of XENON1T using two calibration sources, radon and krypton. Although there is a small discrepancy, from the two, we expect krypton to be more precise. At the end of the science run, it was measured an electron life-time of $\sim 650\,\mu s$, which corresponds to an oxygen concentration below ppb level. For a more detailed description of the electron life-time in XENON1T, see [34].

XENON1T improved the sensitivity for the cross section of the WIMP-nucleus interaction about one order of magnitude compared to XENON100, with its minimum for a WIMP

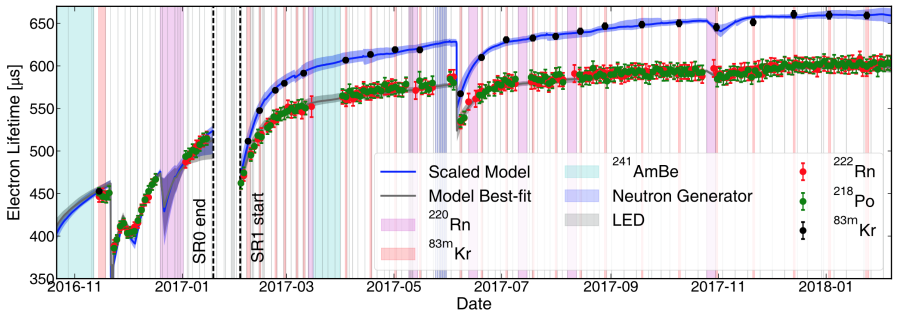

Figure 2.5.: Evolution of the electron life-time in XENON1T. The vertical colored bands indicate the several data taking mode, with white being dark matter mode. Figure taken from [34].

with mass 30 GeV/c^2 at 4.1×10^{-47}cm^2 (see figure 1.5) [21], making it the most sensitive WIMP detector at present time.

Although WIMP detection is the primary purpose of dual-phase TPC, several other physics channel are also taken into consideration. One major result is the first detection of the double electron capture of ^{124}Xe [45], with an half-life of 1.8×10^{22} years, which makes it the longest half-life ever observed. At low energies, XENON1T observed an excess of events in the electronic recoil band compared to what was expected from the background (see figure 2.6) [32]. The searches of excess electronic recoil events at low energies are motivated by both the search for axions and the neutrino magnetic moment.

XENON1T is not sensitive to dark matter axions since their energy is below XENON1T threshold, but we expect that axions created in the sun would appear in the keV range, to which XENON1T is sensitive. As there is no strong magnetic field in the XENON experiments, the Primakoff effect can not be used for axion detection. The way that axions can be detected in XENON1T is through the axio-electric effect, the equivalent of the photo-electric effect, which depends on g_{ae}. XENON1T is therefore sensitive to g_{ae} and its combinations with $g_{a\gamma}$ and g_{an}, depending on how the axion creation mechanism in the Sun [46]. If the excess is caused by axions, it would be the first detection of this particle.

The neutrino magnetic moment can be measured with XENON1T because it would enhance the neutrino flux from the Sun. The expected neutrino background in presence of no enhanced neutrino magnetic moment is calculated in [47] and this excess is compatible with a value of $\mu_\nu \in (1.4, 2.9) \times 10^{-11}\mu_B$ (see figure 1.7).

Finally, this excess can also be generated by some SM backgrounds not taken into consideration so far. As this will be the focus of this work, more details will be given in chapter 5.

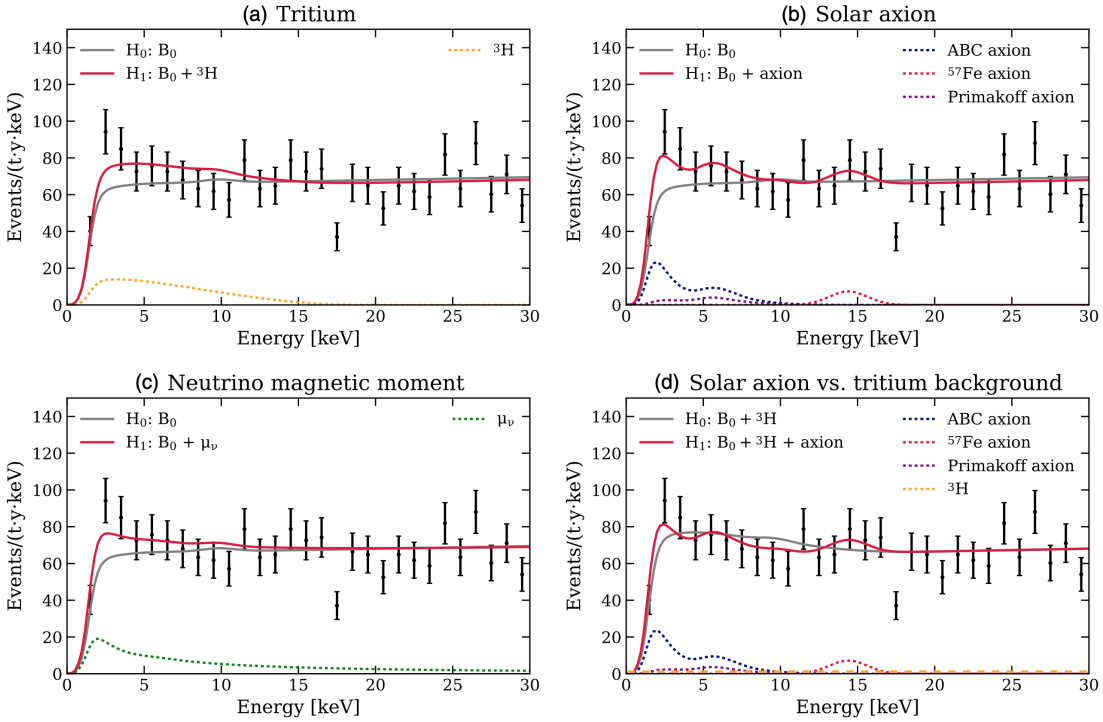

Figure 2.6.: Fits to the data of the low energy electronic recoil excess under various hypotheses. The null and alternative hypotheses in each scenario are denoted by gray (solid) and red (solid) lines, respectively. For the tritium (a), solar axion (b), and neutrino magnetic moment (c) searches, the null hypothesis is the background model B_0 and the alternative hypothesis is B_0 plus the respective signal. Contributions from selected components in each alternative hypothesis are illustrated by dashed lines. Panel (d) shows the best fits for an additional statistical test on the solar axion hypothesis, where an unconstrained tritium component is included in both null and alternative hypotheses. This tritium component contributes significantly to the null hypothesis, but its best-fit rate is negligible in the alternative hypothesis, which is illustrated by the orange dashed line in the same panel. Figure and caption taken from [32].

2.2.2 XENONnT

XENONnT is the last experiment in the XENON series [48]. This experiment has a total of 8.4 tonnes of xenon, of which 5.9 are part of the active target. The TPC design is similar to the one of XENON1T, with increased dimension: it is 149 cm high and it has a diameter of 133 cm. The two PMTs arrays have 253 PMTs (top) and 241 (bottom). The walls of the TPC are formed by 24 PTFE panels that partially overlap with 24 PTFE blocking panels, situated a the corners of the reflectors.

A technical paper on the XENONnT experiment is under preparation. Most of the subsystem are the same as in XENON1T. There are two main addition to the gas system:

- A new radon column is installed. For a more detailed description, see 2.3.2. The new column is also connected to the purification subsystem.

- A novel liquid-only purification system, using a high-efficiency oxygen filter for the first cleaning and a second low-radon filter for the standard operation. A paper is also in preparation about this system. This new purification is completely decoupled from the other gas system and it is used to circulate and purify specifically the LXe of the xenon. The system is also equipped with a purity monitor that allows to monitor the electron life-time (see figure 2.7).

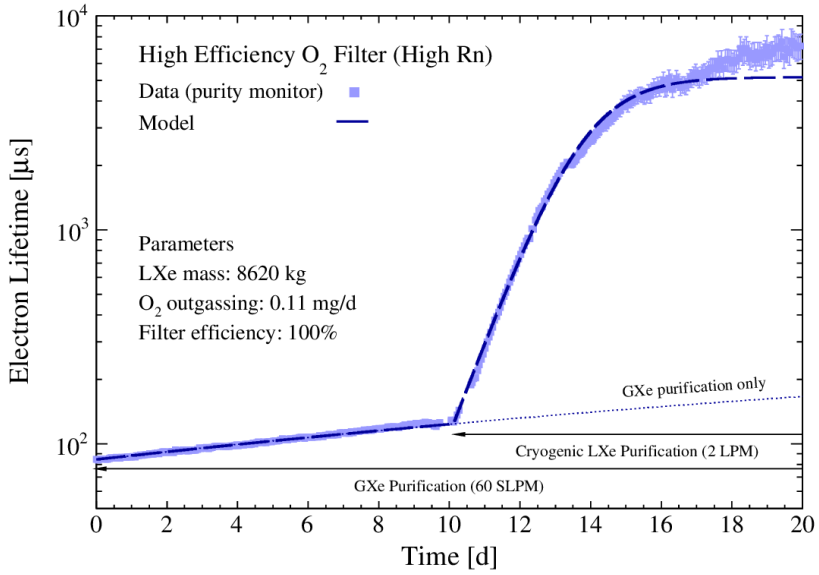

Figure 2.7.: Electron life-time as monitored by the purity monitor when starting the first cleaning of the xenon inventory from oxygen. During XENON1T, only the LXe was purified. Figure from the XENON collaboration.

XENONnT is expected to reach a sensitivity up to $1.4 \times 10^{-48}\text{cm}^2$ for a WIMP with mass 50 GeV/c^2 (see figure 2.8). In addition, the improved sensitivity will allow to distinguish if the excess observed in [32] is due to a SM background or new physics [46].

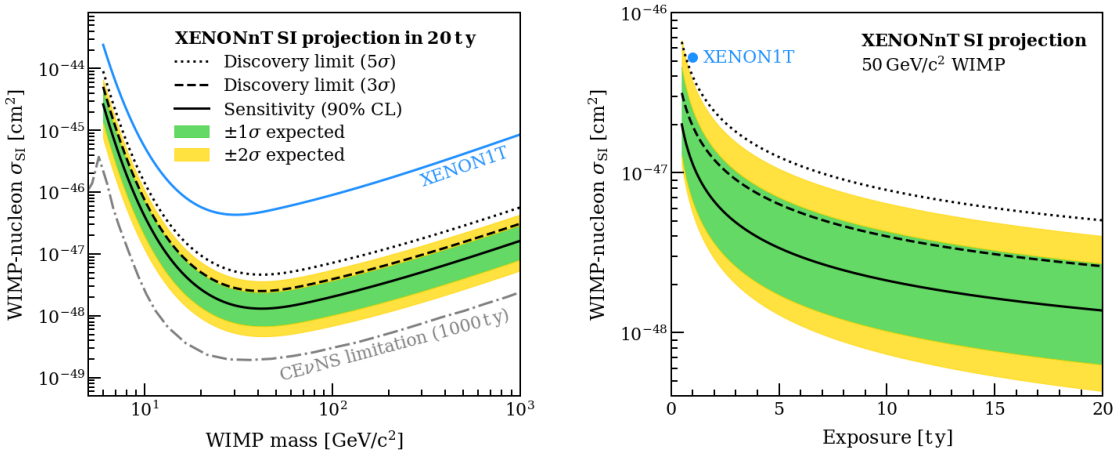

Figure 2.8.: Left: Projection of XENONnT sensitivity for spin-independent WIMP-SM nucleus cross section. Right: Sensitivity vs exposure for a WIMP with mass 50 GeV/c^2. Figure taken from [48].

2.3 Backgrounds

As written in this chapte's introduction, a huge part of the effort for rare-event searches is devoted to background reduction. In this section, all major sources of background in XENON1T and XENONnTare listed, based on where they originate.

2.3.1 External sources

In this category belong all the sources that are generated outside the active target. The most prominent one is the cosmic radiation, which can generate:

- γ rays. For WIMPs searches, they can be discriminated against, as they recoil electronically.
- neutrons. They can be generated in muon induced showers and they generate a nuclear recoil, which makes them very dangerous for WIMPs searches.

In order to shield from cosmic radiation, the XENON experiments are built at Laboratori Nazionali del Gran Sasso (LNGS) in Italy, exploiting the natural stopping power of rocks. The underground LNGS facility has ~ 1400 rock overburden, equivalent to ~ 3700 m of water, which reduce the atmospheric muon flux by around 6 orders of magnitude (see figure 2.9)

Even with the detector shielded from cosmic radiation, there are several other sources of natural radioactivity present in the rocks and concrete of LNGS. There are 3 primordial elements that are still decaying nowadays: ^{235}Ur, ^{238}Ur and ^{228}Th. Their decay chain produces several α, β and γ particles. As a byproduct, they can also generate neutrons in (α, n) reactions or spontaneous fission. In order to shield from the environmental radioactivity, both active and passive neutron shields are employed. XENON100 used a small water shield. XENON1T used a water tank with a volume of 740 m^3. The tank is instrumented with 84 PMTs and it works also as an active Cherenkov detector, providing

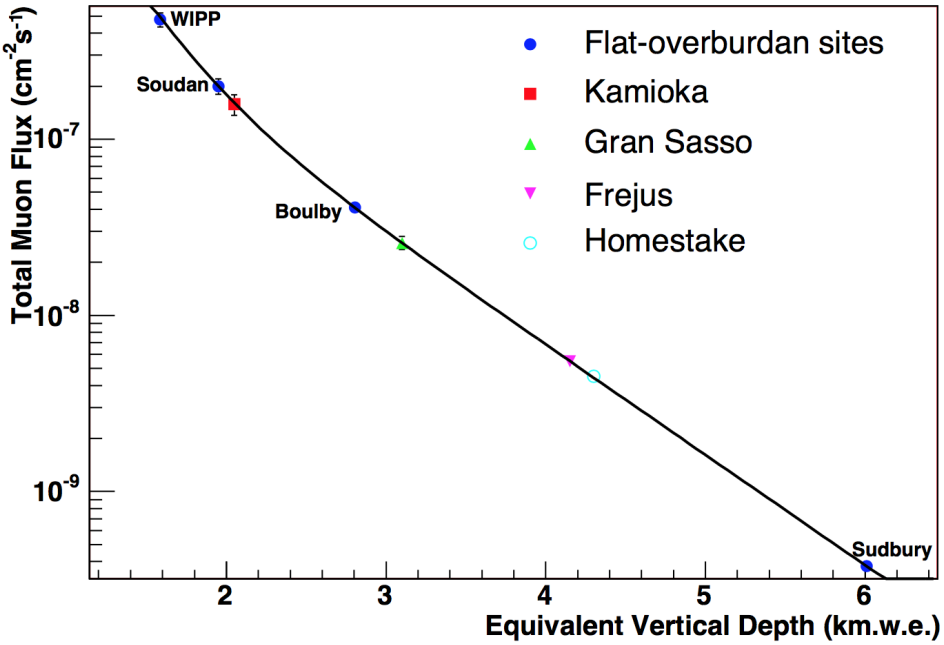

Figure 2.9.: Total muon flux measured for the various underground sites. Due to the different nature of soil in different locations, the depth is given in water equivalent kilometers. Figure taken from [49].

a way to tag muons [50]. XENONnT uses the same water tank infrastructure, with an additional active neutron veto built around the cryostat.

Even when all the external radioactivity is shielded or tagged, radioactive contaminants can be found inside the materials used for the construction of the detector. A huge effort is devoted in selecting and screening beforehand the materials that will be used for the construction of the detector [51, 52]. Finally, it has been observed that materials exposed to air during construction are contaminated with radon progeny, which means that great care has to be taken for cleaning [53] and storing the material. As the storage is part of the focus of this work, it will expanded in chapter 6.

A final remark: external sources can be excluded through fiducialization [34] and are sub-dominant compared to internal sources [21], which will be illustrated in the next section.

2.3.2 Internal sources

In this category are the sources that are within the LXe target itself. Xenon has only one unstable isotope ^{126}Xe, which decays in $\beta\beta$, but since it has a half life of $t_{1/2} = 2.165 \times 10^{21}$ years it is negligible compared to other backgrounds. The most important internal sources are other elements that might mix with the xenon target. A list is presented below but tritium is omitted, since it will be explained in detail in chapter 5.

Krypton Xenon is produced by separation of air components. Krypton, also a noble gas which is ~ 10 times more abundant in air than xenon, proves to be hard to separate from xenon and it is expected to be present at ppm level in commercially bought xenon. One of the isotopes of krypton, ^{85}Kr, is a beta emitter with maximum energy 687 keV and was one of the most prominent background in XENON100[54]. In XENON1T (and consequently in XENONnT) a distillation column was developed dedicated to this task, and it was used to reduce krypton to ppq[1] level [55], well below the initial goal of 2 ppt[2][56]. The column exploits the fact that krypton has a higher vapour pressure than xenon (see table 2.1): the distillation creates a krypton-enriched GXe phase at the top which is removed. The distillation is performed until the target krypton concentration is reached.

Argon Argon has several decaying isotopes. Among them, the most problematic is ^{37}Ar. It decays with an electron capture generating a 2.82 keV peak, which is increases the background rate for electronic recoil searches at low energies. Argon can contaminate the xenon in two ways: either it is there from the xenon production or it is introduced via an air leak. The argon concentration at the start of XENON1T was measured to be < 5 ppm [57]. The argon is further purified by the krypton distillation; in fact, the distillation is even more efficient since argon has a higher vapour pressure than krypton (see table 2.1). The initial argon contamination is calculated to be sub-dominant compared to tritium. In case a leak is present, a constant amount of argon can be injected in the system. Since the krypton distillation is not performed during a science run and argon, as a noble gas, it is not removed by the hot gas purifiers, the argon would stay in the system. During XENON1T several krypton measurements were taken, and it is possible to constrain an hypothetical air leak rate with them. It was calculated that, for XENON1T, also an air leak rate would cause a subdominant contamination of ^{37}Ar [32].

Radon Radon is also a noble gas which has no stable isotope. The most abundant one, and the one that contributes the most to the background, is ^{222}Rn [47]. ^{222}Rn is part of the ^{238}Ur chain and it is the decay product of ^{226}Ra. As mentioned in the external background section, ^{226}Ra contaminates the material used for constructing the detector. Radium itself is metallic and decays inside the materials, however ^{222}Rn is a noble gas that can then emanate from the material and mix with the LXe. With its half-life of ~ 3 days, it can reach the fiducial volume where it then decays with an α particle, which has an energy much higher than our region of interest. However, its decay products, ^{212}Pb and ^{212}Bi, are beta emitters with low energy, and make up the majority of the electronic recoil events in an energy region which overlaps the one for the WIMPs searches. The radon background challenge is tackled in two ways in XENON1T: first, the materials are selected for a minimal radon emanation [58], and second, a dedicated distillation column can be included for a constant depletion of ^{222}Rn from xenon [59]. This column works in a specular way compared to the krypton column: since the vapour pressure of radon is larger than the one of xenon, the GXe phase will be radon depleted. The radon accumulates at the LXe phase at the bottom, where it decays. It is not necessary to remove any xenon in order to remove radon, since the half-life of radon is ~ 3 days.

[1] part per quadrillion
[2] part per trillion

Element	**Boiling temperature (°C)**	**Vapour pressure at -97°C (bar)**
Hydrogen	−253	-
Nitrogen	−196	-
Oxygen	−182	-
Argon	−185	~ 100
Krypton	−153	20.9
Xenon	−108	2.0
Radon	−61	0.2

Table 2.1.: Table with the boiling temperatures and vapour pressure at the operating temperature of XENON1T and XENONnT of the most relevant elements for this work. For the lighter elements the vapour pressure is too high to be measured. Data from [60].

Chapter 3

Measurement of trace impurities at sub-ppb level

As written in chapter 1, the purity of the xenon is crucial for the success of dual-phase TPCs for rare event searches. For XENON1T, great care has been taken in analyzing the xenon prior to the detector filling [57, 61]. For XENONnT, the purity requirements are even more stringent: the target electron life-time of XENONnT, requires an oxygen equivalent amount of impurities of the order of 10 to 100 ppt, and the excess at low energy can be explained with an hydrogen contamination of the order to 1 to 10 ppb.

As the setup used in [57, 61] has a decision threshold of ~ 20 ppb, in this work a novel method to analyze impurities in xenon has been developed using Atmospheric pressure ionization mass spectrometry (APIMS).

Section 3.1 describes the working principle of APIMS. Sections 3.2 and 3.3 introduces the commercial device used in this work, the APIX dQ. Section 3.4 describes the first combination of the APIX dQ with the old setup from [57, 61]. Section 3.6 describes an improved chromatography setup with a new gas system and section 3.7 describes the data analysis of this system.

3.1 Principle of operation of APIMS

The system is composed, as said by the name, by two components: the Atmospheric Pressure Ionization, and the Mass Spectrometer. In this section, both of them will be described.

3.1.1 Mass spectrometry

Mass spectrometry is a well established experimental technique that measures the ratio m/q of ions in a mixture, where m is the mass and q is the charge of the ion. The first step (ion creation) will be explained in the next section.

Once the ions are created, they fly through a mass filter. In the instrument used in this work, the APIX dQ, a quadrupole mass filter is used. It is composed by 4 metal rods, each

opposing pair connected together electrically. A radio frequency Radio frequency (RF) generator with a Direct current (DC) offset is applied to the rods, creating an electric field in the center. The motion of the ions through the rods can be derived combining Newton's equation of motion and using Coulomb's force, and it is (from [62]):

$$\frac{\mathrm{d}^2x}{\mathrm{d}t^2} = -\left(\frac{e}{m}\right)\frac{[U + V\cos(\omega t)]}{r_0^2}x \tag{3.1}$$

$$\frac{\mathrm{d}^2y}{\mathrm{d}t^2} = \left(\frac{e}{m}\right)\frac{[U + V\cos(\omega t)]}{r_0^2}y \tag{3.2}$$

$$\frac{\mathrm{d}^2z}{\mathrm{d}t^2} = 0 \tag{3.3}$$

where e is the electron charge, m the mass of the ion, U the DC potential and V the amplitude of the RF. $2r_0$ is the closest distance between the four electrodes.

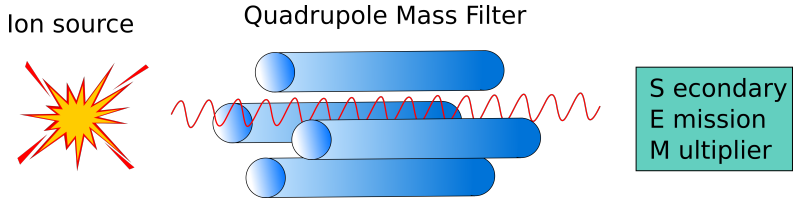

Figure 3.1.: Scheme of the quadrupole mass filter.

Equations 3.1 and 3.2 are Mathieu equations [63] and can be solved numerically. It is possible to find a range of values of U and V for which the motion of the ion is stable in both x and y. By setting U and V it is then possible to filter only the ions with the correct (m/q) ratio. All the other ions have an unstable trajectory and will collapse to one of the rods.

Once an ion has passed the filter, it needs to be detected. The APIX dQ is equipped with a Secondary electron multiplier (SEM) detector which is operated in pulse-counting mode ([64]). The ions that pass through the filter hit a semiconducting surface layer which causes the emission of electrons. The electrons are then accelerated in the detector channel by a high voltage bias and release more electrons on the way. At the output, each primary electron generates a pulse of 10^7 to 10^8 electrons, which induces an electric current that can be amplified and measured.

3.1.2 Atmospheric pressure ionization

All the steps for mass spectrometry (ionization, mass filtering and detection) are usually operated in a hard vacuum environment (around 10^{-5} to 10^{-6} mbar). However, the ionization was historically tried close to or at atmospheric pressure to find trace water in otherwise "pure" gases [66, Ch.1]. The technique was then used to detect organic compounds ([67]) and today it has a wide range of applications, among which, in the field of low background experiments, to detect krypton traces in xenon ([68]).

Nowadays, it is not the sample itself but a bulk gas that is at atmospheric pressure

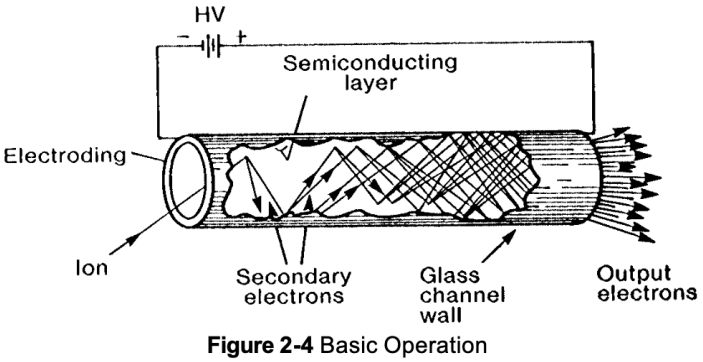

(a) Schematic of a channeltron detector (from [65]).

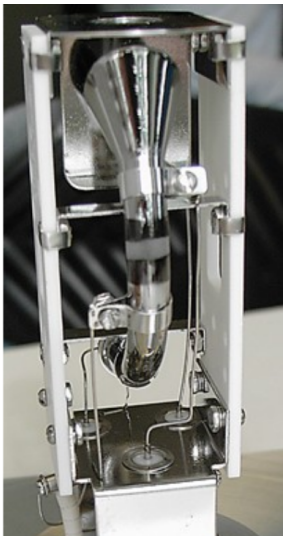

(b) Picture of the channeltron in the APIX dQ.

[66, Ch.2]. The usage of a bulk gas allows to have more control on the ionization process efficiency and, in particular, to make sure that the species of interest are ionized.

In the ion source used in this work, the bulk gas is ionized in a chamber at atmospheric pressure using a corona discharge. A high voltage is applied to a stainless steel needle, which causes a corona discharge that leads to the creation of ion-electron pairs of the bulk gas [69]. A corona discharge happens when the strength of an electric field in a localized spot exceeds the dielectric strength of the medium, causing an electrical breakdown of the medium itself. As each gas has a different breakdown field, the voltage of the needle has to be adjusted based on the bulk gas in use.

The ions and the electrons are accelerated by the electric field in opposite directions: the electrons are attracted to the positive biased needle and are neutralized there. The positive ions move in opposite direction towards a ground plate. While they travel, they collide with other molecules. If the other molecule is the same as the carrier gas, they can form positive bounded molecules (X_2, X_4, ..., where X is the element of the bulk gas).

More interesting for our needs, if there is molecule from another species (a trace impurity) in the bulk gas, the positively charged ions can "steal" an electron if this impurity has a lower ionization potential. The ionization potential is the energy needed to separate one electron from a neutral atom: if it is lower for the trace impurity, when a bulk gas molecule (X) collides with a trace impurity (T), the most favourable energetic state is when the electron is transferred.

$$X^+ + T \rightarrow X + T^+ + \text{energy}$$

The most important criteria to choose a bulk gas is the fact that it has a higher ionization potential compared to the one of the trace impurities that needs to be measured. Table 3.1 lists some of the ionization potentials for the elements we are interested in. From this table, helium is an obvious choice as bulk gas, as it allows to ionize air components, as

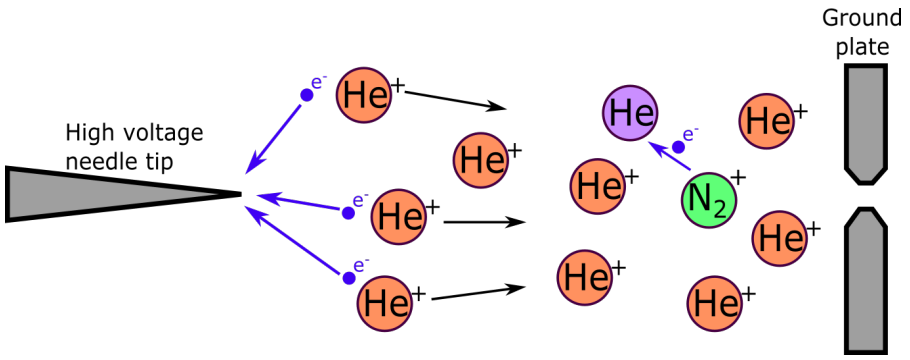

Figure 3.3.: Schematic of the atmospheric pressure ionization process. The high voltage at the needle creates ion (red)-electron(blue) pairs of the bulk gas (in this case helium). The electrons are attracted by the positive potential and neutralized at the needle tip. The positive ions can collide with other molecules present in the mix (in this case nitrogen), who donate an electron.

well as krypton and water. Helium is used as bulk gas for all this work.

Component	**Ionization potential (eV)**
Helium	24.59
Argon	15.76
Nitrogen	15.58
Hydrogen	15.43
Krypton	14.00
Methane	12.60
Water	12.60
Xenon	12.13
Oxygen	12.06

Table 3.1.: List of ionization potentials [60]

The downside with this method of ionization is that when the trace components are too high, their presence makes ionization of the bulk gas less efficient. For this reason the APIMS technique saturates at contamination on the level of 100 ppb[1]. This has two big consequences:

- The calibration of an APIMS system can not be performed with commercially available calibration gases: the lowest impurity level that can be reached is $\mathcal{O}$(5ppm). This will be discussed in section 3.2.1.
- When measuring any gaseous sample which has not the bulk gas of choice as base component, the ionization efficiency drops dramatically. This works focusses on measuring impurities in gaseous xenon, which, looking at its ionization potential,

[1]part per billion

would only ionize oxygen. We need a way to separate the xenon from its impurities. The solution to this problem is presented in section 3.4

Even with this saturation effect, the APIMS can be used to measure trace impurities $\mathcal{O}(1\text{ppt} - 100\text{ppb})$, depending on the species. Figure 3.4 shows an example of a APIMS calibration, presented in log-log scale due to the big range. The curve is linear in the central part and exhibits two plateaus at the two extremes. At high concentration, the plateau is due to the saturation of the atmospheric pressure ionization; at the bottom, it is due to a non-zero background of the machine.

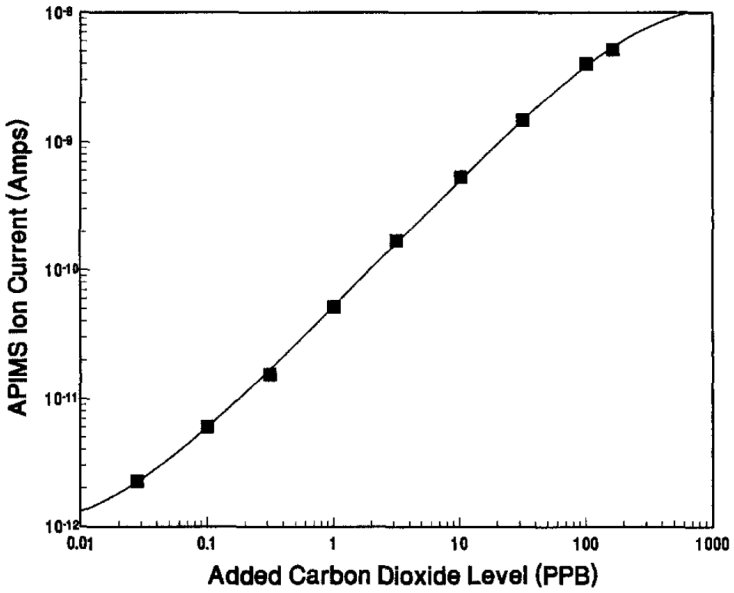

Figure 3.4.: Calibration of carbon dioxide in nitrogen. The two plateaus at the top and at the bottom are caused by saturation and a non-zero background respectively. Figure from [70]

3.2 APIX dQ

In this work, a commercially available APIMS device, the APIX dQ from Thermo Fisher Scientific has been used [71]. This machine was designed primarily for the semiconductor manufacture industry [72]. It is optimised for the detection of oxygen and moisture in nitrogen, argon, helium and hydrogen, as those are the main problematic molecules for the semiconductor assembly. The APIX dQ is designed to work in an industrial environment with a continuous stream of gas that needs to be monitored constantly and alarms raised in case it becomes too contaminated.

The requirements of detecting of trace impurities below 0.1 ppb level makes the APIX dQ a very good candidate for our needs (see table 3.2).

	Bulk gas		
Impurity	Nitrogen	Argon	Helium
Argon	X	X	X
Nitrogen	X	500	< 50
Krypton	1	1	< 10
Water	< 10	< 10	< 10
Oxygen	1	< 10	< 1

Table 3.2.: Detection limits of impurities depending on the carrier gas in ppt[2] according to ThermoFisher [60].

In this section, the APIX dQ subsystems will be described.

3.2.1 Gas blender

The APIX dQ is equipped with a gas system, referred to as "Gas Blender" from AirLiquide. It has two main functions:

- Keep the gas flow stable.
- Dilute the calibration gas in order not to saturate the APIMS during a calibration, as written in section 3.1.2.

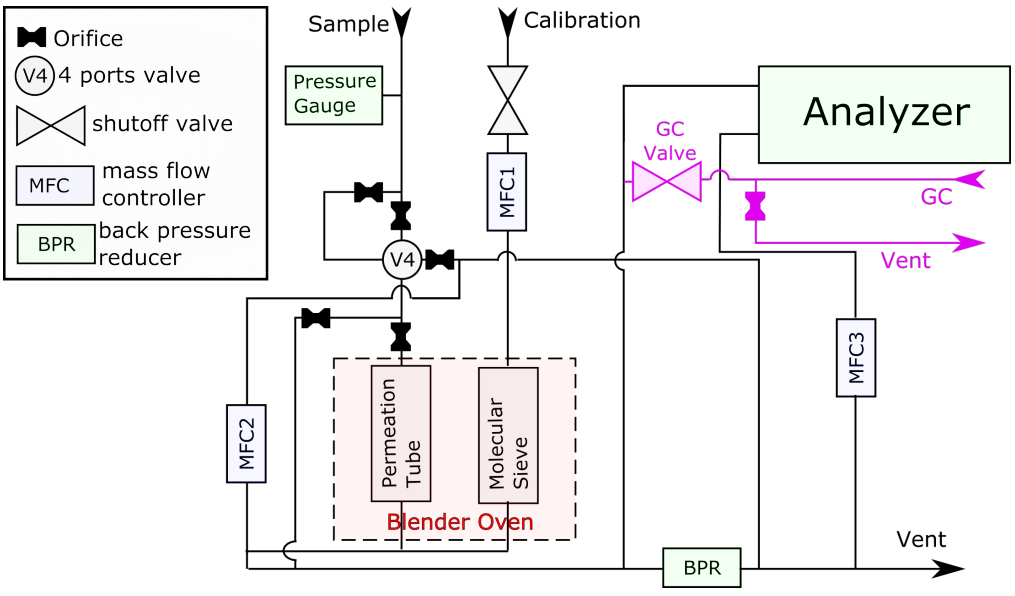

Figure 3.5.: Scheme of the APIX dQ gas blender. In purple are the modifications from the commercial device.

For its industrial use, the gas that has to be measured is used as bulk gas itself, hence there is only one port called "Sample" in figure 3.5. To avoid spoiling the sample stream, the system needs to be both leak-tight and dead-volumes free. In order to minimize

dead volumes, the design of the gas blender uses a minimal amount of valves, preferring instead Mass flow controllers (MFCs) to control the gas flow. In addition, it uses flat seal RHP fittings from *Flowmeca*, which have no dead volume. In order to ensure no air contamination, the whole system is at 5 bar overpressure and it operates at a flow of 5 std[3] l/min.

When entering the system, the sample passes through a series of orifices which reduce the flow. The orifice choice depends on the bulk gas, and V4 is remotely toggled from the software depending on which gas is selected from the measurement routine. The sample gas is then split by two more orifices: most of it goes directly down to the Back pressure reducer (BPR) and the analyzer.

Another smaller part is used to mix with the "high impurity" calibration gas for calibrating the APIX dQ. First it goes inside the blender oven, where a permeation tube adds a controlled amount of moisture to be used as calibration standard. After the oven, this gas is mixed together with the calibration gas. The calibration gas itself goes through a Molecular Sieve that, on the opposite, traps water, ensuring that no extra water is added in addition to the one from the permeation tube. The small flow of the calibration gas is then mixed with the small flow of the sample plus moisture gas and forms the final calibration mixture used in the APIX dQ.

Just before the ionization chamber, there is a BPR that ensures that the pressure that reaches the chamber is always constant at 1.1 bar. It does so by regulating a valve opening to the vent. Of the 5 std l/min used by the blender, 4 are going directly to the vent via this BPR. In addition, the MFC3 keeps the flow constant between 0.9 and 1.3 std l /min, depending on the bulk gas.

The gas blender has two settings:

Measurement mode: MFC2 is open, leaving the calibration gas plus controlled moisture free to go directly to the vent, after the BPR. In this mode, no calibration gas reaches the analyzer.

Calibration mode: MFC2 is partially or totally closed. This way, the calibration gas is mixed with the bulk gas. By setting the opening point of MFC2 it is possible to dilute the calibration gas with different dilution factors. The system can achieve dilutions factors from 10^{-3} to 10^{-5}.

The extra valve and line in purple added before the analyzer will be described in 3.5.

3.2.2 Vacuum system

The main body of the APIX dQ is contained in its vacuum system. This system is leak-tight and contains all the main component of the APIMS:

1. The ionization source at atmospheric pressure;
2. An orifice system to reach the operating pressure of the Quadrupole mass spectrometer (QMS)(10^{-6} mbar);
3. A lens stack to focus the ion in the QMS;

[3]standard

4. The analyzer chamber that contains the QMS itself.

It also has a port to a pirani gauge to monitor the pressure in the analyzer chamber, and two turbo pumps Pfeiffer vacuum HiPace80[73].

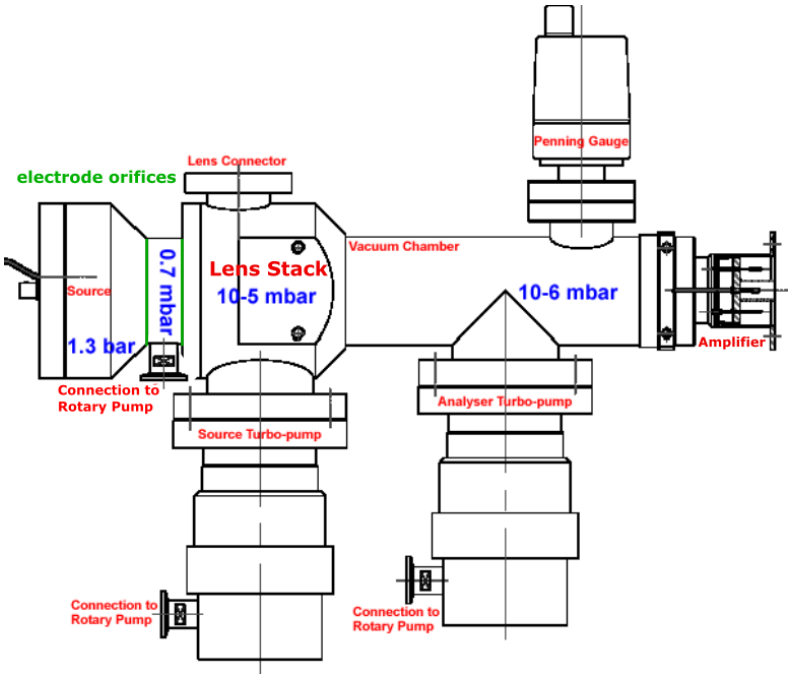

Figure 3.6.: Scheme of the APIX ionization and detection system.

Ionization source The APIX dQ has uses a high voltage needle to cause a corona discharge to ionize gas at atmospheric pressure as described in 3.1.2. The sample gas is injected close to the needle.

Orifice system These are two metal plates with two holes, set at a pre-defined voltage. There are two steps: one for the rotary pump, one for the turbo pump. The voltages need to be adapted to maximaze ion collection, and their optimal voltage is different for different molecules. The APIX software provides a way to modify the voltage depending on the mass monitored, but it takes time to equalize the charges on the metal surfaces, especially when the surface is not perfectly clean. For this reason, in this work a compromise is found that allows to best monitor all the ions of interest.

Lens stack The lens stack is a series of charged plates whose role is guides the ions to the QMS. As with the orifices, the optimal voltage for collection differs from molecule to molecule and needs to be set in advance.

3.2.3 Software

Thermo Fisher provides an official software for the APIX dQ: GasWorks. It provides a way to control most of the parameters described above, including the settings for the

quadrupole filter, the discriminator threshold for the amplifier and the mass alignment settings. It also warns when some parameter is not at a safe level and if necessary it shuts down the ionization source or the SEM.

The software has several data taking modes. The ones used in this work are:

Analog scan: It measure the signal vs mass. It is possible to change the mass range (m/q from 0 to 200 AMU), the mass step and the integration time. Higher integration times result in a slower scan time but at the same time allow to have lower statistical fluctuations. This mode is used mostly to monitor the background traces of the APIX dQ since it requires a stable impurity stream.

Multiple Ion Monitor (MIM): It records the signal of the selected m/q value (called "trace") over time. This is the mode used to measure the xenon samples. There are 3 options for the integration speed and the same caveats are valid as for the analog scan: the higher the speed, the smaller the sampling time and the bigger the statistical fluctuation of the trace. Moreover, each trace require time to be recorded, so the more the traces, the larger the sampling time. In addition to the traces, this mode can also record (at higher sampling time) other parameters of operation of the APIX dQ (see subsection 3.3.1).

3.3 APIX dQ signal characterization

The first step to characterize the response of the APIX dQ is to study the background and calibration analog scans and identify the masses of the impurities we are interested in. The list of the most important impurities and the masses used to measure them is in table 3.3. When an element has more than one isotope, like xenon and krypton, the most abundant one is chosen. A special case is hydrogen: while the hydrogen mass is 2 AMU, this mass is impossible to monitor, both because the very low value means it is sensitive to electrical noise from the QMS, and because it lies below helium (mass = 4 AMU). The solution to this problem is to monitor instead a molecule, $(He_2{+}H)^+$, at mass 9 AMU. This is possible since there are a lot of $(He_2)^+$ ions generated by the APIMS, which then can form a bounded state with one hydrogen atom. This process is less efficient than the simple electron transfer, so the hydrogen response is weaker compared to other impurities.

Figure 3.7 shows the overlay of an analog and background scan, and marks the impurities from table 3.3 with vertical stripes. All the data is using helium 6.0[5] as a bulk/carrier gas which was purified with a hot gas purifier [6].

[5] Helium containing less than 10^{-6} of other atoms and molecules.
[6] https://puregasproducts.com/pdf/ps3spec_512.pdf

Table 3.3.: List of the most important impurities and the atomic masses used to measure them.

Impurity	Mass (AMU[4])
H	9
N	14
CH_4	16
H_2O	18
N_2, CO	28
O_2	32
Ar	40
Kr	84
Xe	132

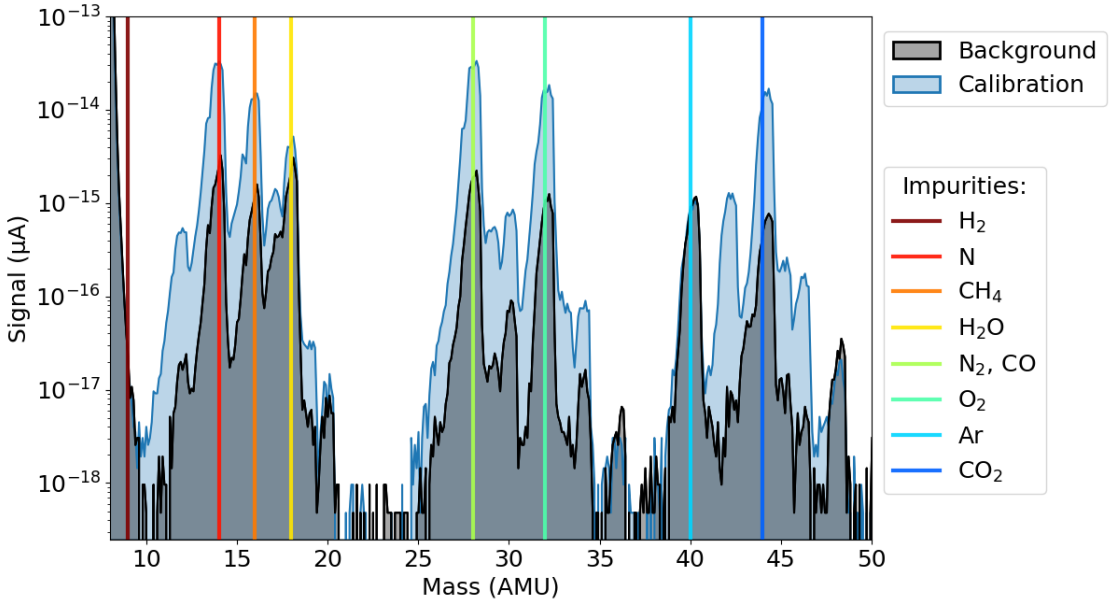

(a)

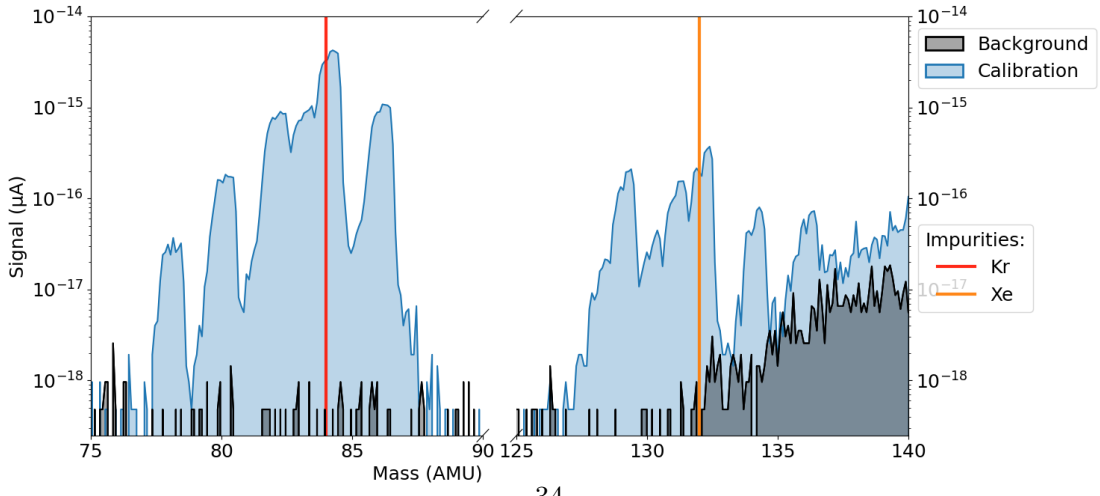

(b)

Figure 3.7.: Analog scan of background with helium only (black) and calibration gas diluted with helium at 0.05% (blue) at different mass ranges. The vertical lines indicate the elements and molecules taken into consideration. Hydrogen is measured as H+He_2 at mass 9.

Looking at the background spectrum at first, at $m/q = 8$ there is the tallest peak due to He_2. This mass is usually avoided not to induce a high ion count and accelerate the ageing of the SEM. Next there is a 3 peaks structure from masses 16 to 18 which is due to water (H_2O, HO and O at 18, 17 and 16 respectively). There are a lot of peaks that are an indication of a small air leak (N, N_2, O_2, Ar, CO_2). However, when comparing the height of the argon peak compared to other air impurities, it is larger respect to the amount of argon in air ($\sim 1\%$). This is due to the fact that argon, as it is a noble gas, is hard to separate from commercially available helium, hence the trace amount of argon in the bulk gas is higher compared to other impurities. Water, air and argon are then the main internal backgrounds. An additional electronic noise is present at very high masses (above 130 amu). This is a known APIX dQ noise that is always constant. In principle it can be reduced by raising the discriminator threshold, but we are not interested in measuring this high masses since no impurity of interest is present there.

The calibration gas spectrum is richer in peaks. During this work, many calibration gases were used, listed in appendix A with their impurity content. Of all the impurities listed in the calibration gases, two are less prominent: one is hydrogen, and the reason is that in the configuration of the APIX dQ the hydrogen signal is suppressed. The other one is argon, and the reason is that the amount of argon in the background is too high.

Since we do not expect water in our samples (see section 3.4) and it is the highest peak in the background (apart from helium at mass 8), we can use water as a tracer for the internal background and as a clue for saturation. For our measurements, we monitor contaminations of H_2, N_2, O_2, Ar and Kr of our sample using the MIM method.

3.3.1 MIM signal stability

The traces of a MIM measurement have in general a normal distribution around a mean value (a mathematical description will be given in section 3.7). The mean of the distribution is in the ideal case stable over time, but there are two parameters of the APIX dQ that have a big influence on it. In this section, those parameters are listed, in order of importance.

1: The corona current. It controls the amount of ions created in the first place. It can be manually set by the user, but it also depends on the amount of impurities in the bulk gas: higher impurity content causes a drop of the corona current. It can be used as a tracer for when the ion source is saturate (see section 3.3.2).

2: The pressure in the analyzer chamber. The signal from the QMS is proportional to the number of ions that can reach it: if not enough ions will reach it, the signal will drop. The pressure in the analyzer chamber is a tracer on the amount of gas that reaches the QMS. It is constantly monitored and a cut is placed when it drops too low. A common cause of pressure drop is if the orifices get obstructed by debris.

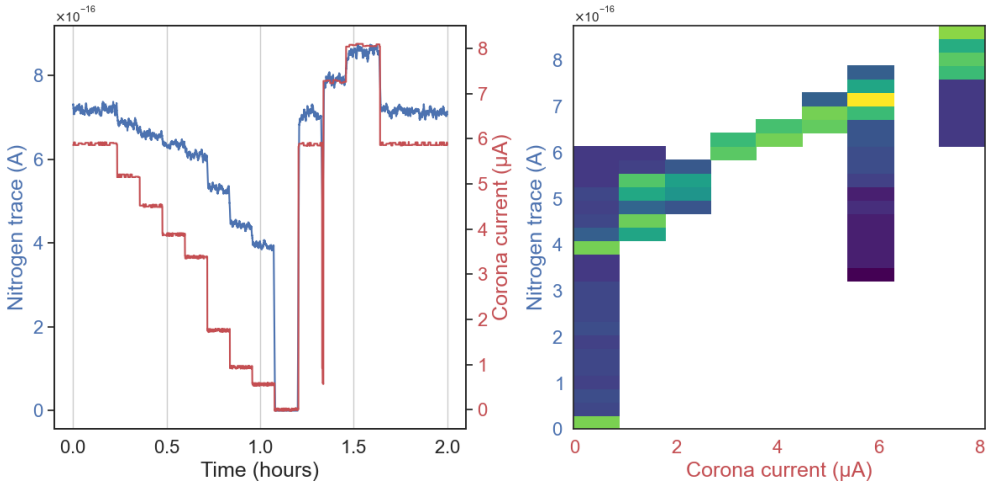

Figure 3.8.: Left: nitrogen trace and corona current vs time. The Corona Current is changed manually and the nitrogen trace follows. Right: 2d histogram of the nitrogen trace and the corona current. The vertical lines at 6 and 8 µA are due to artifact from the MIM data taking mode (the time binning is different for the corona current and the nitrogen trace).

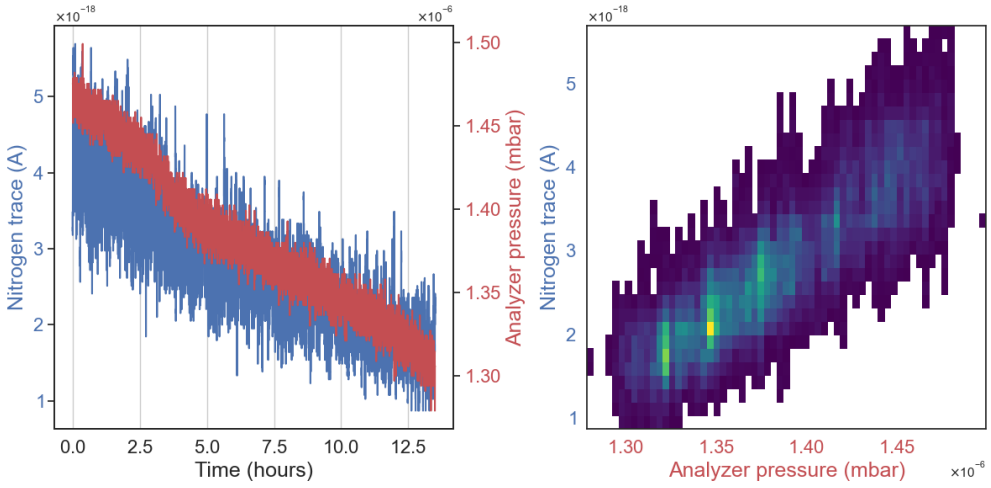

Figure 3.9.: Left: nitrogen trace and analyzer pressure vs time. Right: 2d histogram of the nitrogen trace and the analyzer pressure.

For both the corona current and the analyzer pressure a safe zone is defined. If any of the two drops out of this zone, the data is rejected.

3.3.2 API saturation

The saturation of the atmosperic pressure ionization is expected to happen when at least one impurity has a concentration higher than 100ppb. This phenomenon is easily visible

in figure 3.10, where argon was injected in the helium bulk gas of the APIX dQ.

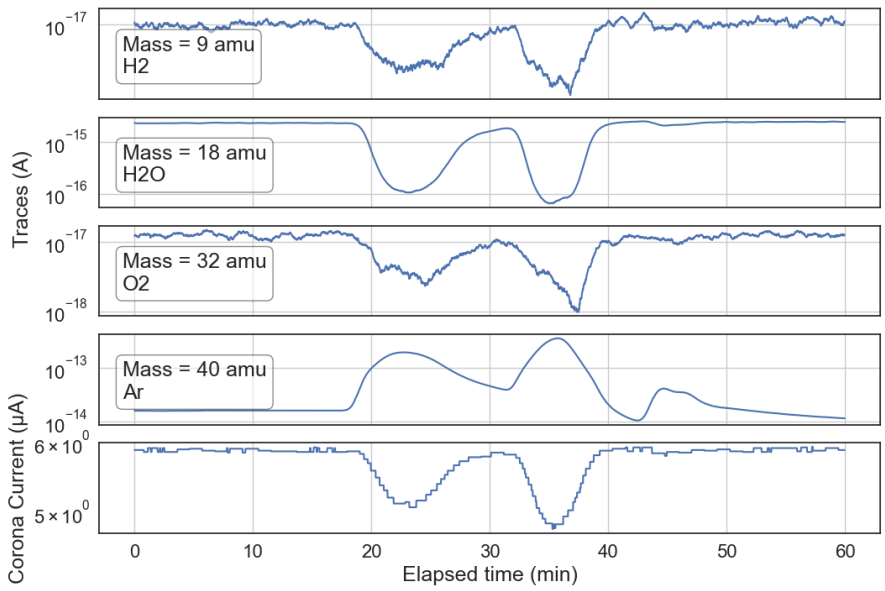

Figure 3.10.: Saturation of the atmospheric pressure ionization. The traces of hydrogen, water, oxygen and argon, and the corona current voltage are recorded at the same time. At $t \sim 18$ minutes a big amount of argon was introduced in the bulk gas stream

The argon trace has a 3 peaks shape, and at the same time all the other traces show an anti-correlated shape. The process is not linear: water (the most intense trace after argon) shows the anti-correlation for the three peaks, while oxygen and hydrogen have dips only corresponding to the first two more intense peaks. This two peak behaviour is also reflected in the corona current: this means that the corona current itself can not be used to correct for the saturation effect. In addition to the non-linearity, it has the problem that the GasWorks software records it with bigger time step compared to the traces, and the reading is not precise enough. For these reasons, there is no way to correct for the saturation of the APIX dQ and the only way to have reliable measurements is to make sure that the impurities reaching the ionization chamber are below 100ppb.

3.4 Gas chromatography

As mentioned in the introduction of this chapter, the sample that we need to measure is a mixture of xenon with other impurities present only at trace level, $\mathcal{O}$(10ppb) or less. Injecting such a mixture in the APIX dQ would saturate the ionization process and no impurity would be visible on top of the xenon signal. In order to separate the xenon from its impurities, we employ gas chromatography.

Chromatography is an experimental technique used to separate components in a moving

phase based on their affinity with a stationary phase [74]. The moving phase can be liquid or gaseous. In this work, we use only gas chromatography. The moving phase is a carrier gas that pushes the sample, and the stationary phase is a solid *ad*sorbent: a material where the sorption happens on the surface and not in the bulk. To isolate the system from air, the process is performed in a leak-tight pipe filled with the adsorbent called "column". The carrier gas pushes the sample through the column. Each component of the gas mixture inserted will move inside the column at different speeds, based on their affinity with the adsorbent. The carrier gas is chosen to have a very low affinity with the adsorbent, thus moving freely in the pipe. At the exit of the column, a detector is placed which records the signal over time. This way, it is possible to construct a "time spectrum" of the components eluting from the column.

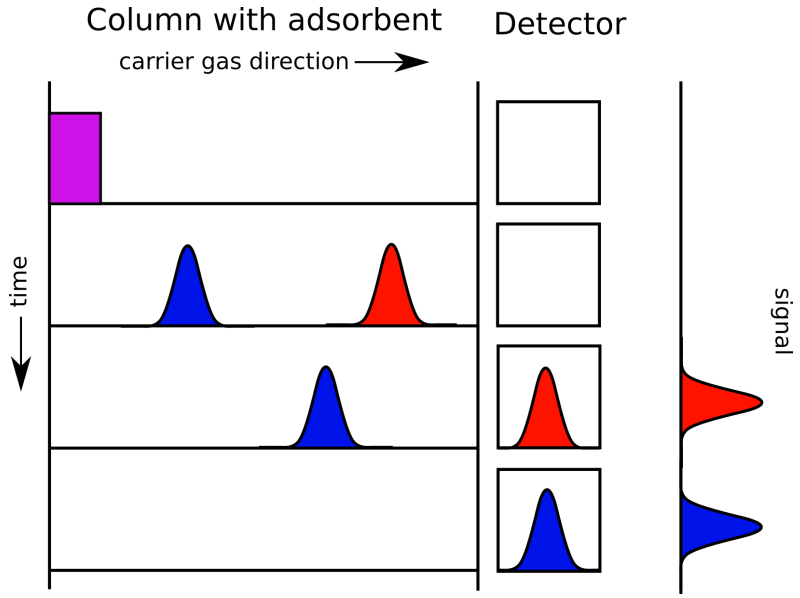

Figure 3.11.: Schematics representation of chromatography.

In our setup, we use the APIX dQ as a detector and helium as a carrier gas. Helium also is the best choice as bulk gas for the APIMS, which allows to easily combine the two processes. The detector used to measure the signal over time is then the APIX dQ with data taking mode MIM.

3.4.1 Commercial gas chromatography

The first chromatography setup used in this work is a commercial Trace GC Ultra (GC) [75] as used in [61] and [57].

The GC employees a pre-separation column with *HayeSep*® polymers and a separation column with Molecular Sieve 5Å (for more details, see section 4.1), each with its own oven to regulate the temperature. It is equipped with a Pulse discharge detector (PDD), which generates a current when it is flushed with a gas that is not helium[76]. The current can be recorded over time to construct a gas chromatograph. The GC uses 6-ways diaphragm valves from the MDCG line from AFP® [77]. They are pneumatically actuated and purged

with clean helium to ensure no environment contamination.

In [61] a procedure was optimized to separate xenon from its impurities, krypton in particular, and the same procedure is also used in this work. Its sensitivity is ~ 20 ppb for krypton and ~ 100 ppb for nitrogen.

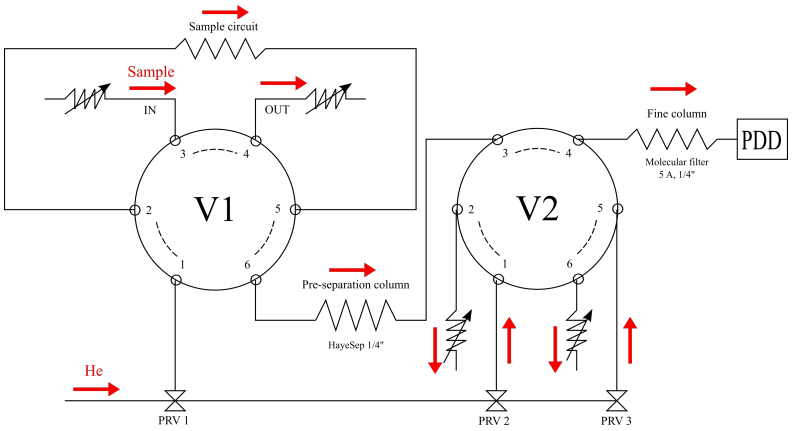

Figure 3.12.: Valve setup of the gas chromatograph. PRV1, PRV2, and PRV3 are pressure reducers. The jagged lines are the columns and the jagged lines with arrows indicate the adjustable flow resistances. All the columns have 1/4 inch section and the lines between the columns and the valves have 1/8 inch section. The red arrows indicate the gas flow. Figure from [57]

Each measurement executes the following steps:

1. At the beginning, the sample flow is started in the sample volume at ~ 30 std ml/min.

2. After a a few minutes to ensure the sample is flowing stably, V2 is switched on to allow the gas from the pre-separation column to reach the fine column.

3. When the flow is stable, V1 is toggled so that the sample is laying in the sample volume is injected into the pre-separation column.

4. After 15 minutes from the injection, both V2 and V1 are switched off in order to prevent xenon from reaching the PDD.

The measurement procedure is fully automatized once the sample is flowing stably in the sample volume (from step 2 onwards).

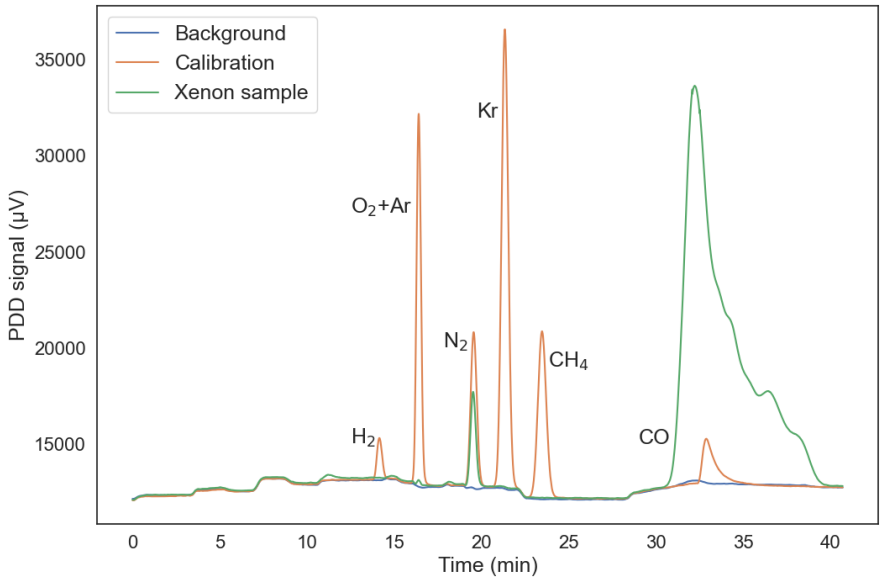

Figure 3.13.: Spectrum of a background (blue), calibration (yellow) and a xenon sample (green) measurements.The peaks of the calibration gas are generated by the marked impurities

3.5 APIX dQ + Trace GC Ultra

In order to detect impurity at sub-ppb level, we need to combine the separation of the GC with the low detection threshold of the APIX dQ. The idea is then to first separate a xenon sample with the GC columns, and then inject it in the APIX dQ. Even though both the APIX dQ and the GC are measuring a continuous gas stream, the GC operates at much lower pressure and flows compared to the APIX dQ gas blender: 1.03 bar vs 5 bars and 30 std ml/min vs 5 std l/min respectively.

A low operation pressure is also necessary to insert a xenon sample from XENON1T or XENONnT: the pressure of those samples are equal to the pressure of the GXe in the gas system, which is $\sim$ 1.3 bar. This is higher than the operation pressure of the GC, but it is not the case for the first part of the APIX dQ gas blender.

For this reason, it is necessary to insert the sample in the APIX dQ *after* the BPR so that the pressure of the gas blender is at atmospheric level and the sample can flow to the ionization chamber. The purple lines of figure figure 3.5 show the modification of the gas blender to allow the sample injection from the GC: when the purple valve ("GC valve") is closed, the gas from the GC flows through the orifice to the vent; when it is open, it mixes with the gas flowing from the gas blender and it reaches the ionization chamber.

Figure 3.14 shows the changes done to the GC gas system compared to [61]. Compared to the setup in figure 3.12, an extra valve was added to the GC to decide whether to send the sample to the PDD or to the APIX dQ. Before the start of each measurement, V3 is set to the desired mode.

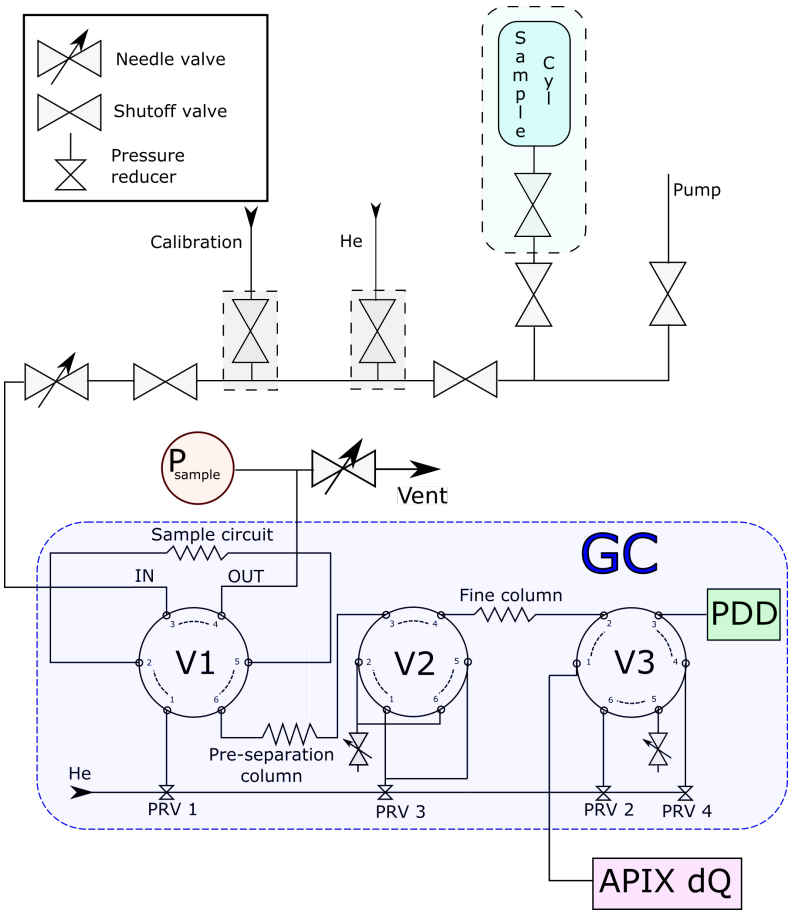

Figure 3.14.: Schematics representation of the combination of the new GC gas system.

3.5.1 Combined measurements

As the APIX dQ differentiates the masses of the impurities, the spectrum will be subdivided in several traces which will be monitored separately using the MIM method. In particular, the carbon trace can be used to monitor all molecules containing carbon, such as CH_4 and CO. The expectation is to see a similar spectrum as the one generated with the PDD in 3.13, but with higher peaks given the improved sensitivity of APIMS compared to the PDD. The results of the first calibrations are presented in figure 3.15, superimposed with a PDD spectrum.

Since the peak width can be less than a minute for small signal, it is important to sample data on a sub-minute time scale in order to record several points for each peak. The MIM is then set to record data in the fastest possible way, but this will result in a bigger statistical error later in the analysis. For the cases where we are interested only in one particular impurity, it is possible to slow down the speed and record *only* the corresponding trace. This possibility is not always open, depending on the amount of sample gas available.

Figure 3.15 shows one APIX dQ measurement overlayed with a similar spectrum from the PDD. At first glance, the data from the APIX dQ traces looks equal or worst. There

are in general larger statistical fluctuation of the baseline, and the peak height is higher for some traces like krypton, but similar for others like oxygen and nitrogen. For hydrogen no peak is visible at all. The traces with the higher signal, N_2 and O_2, have several dips corresponding to the other peaks due to saturation effects.

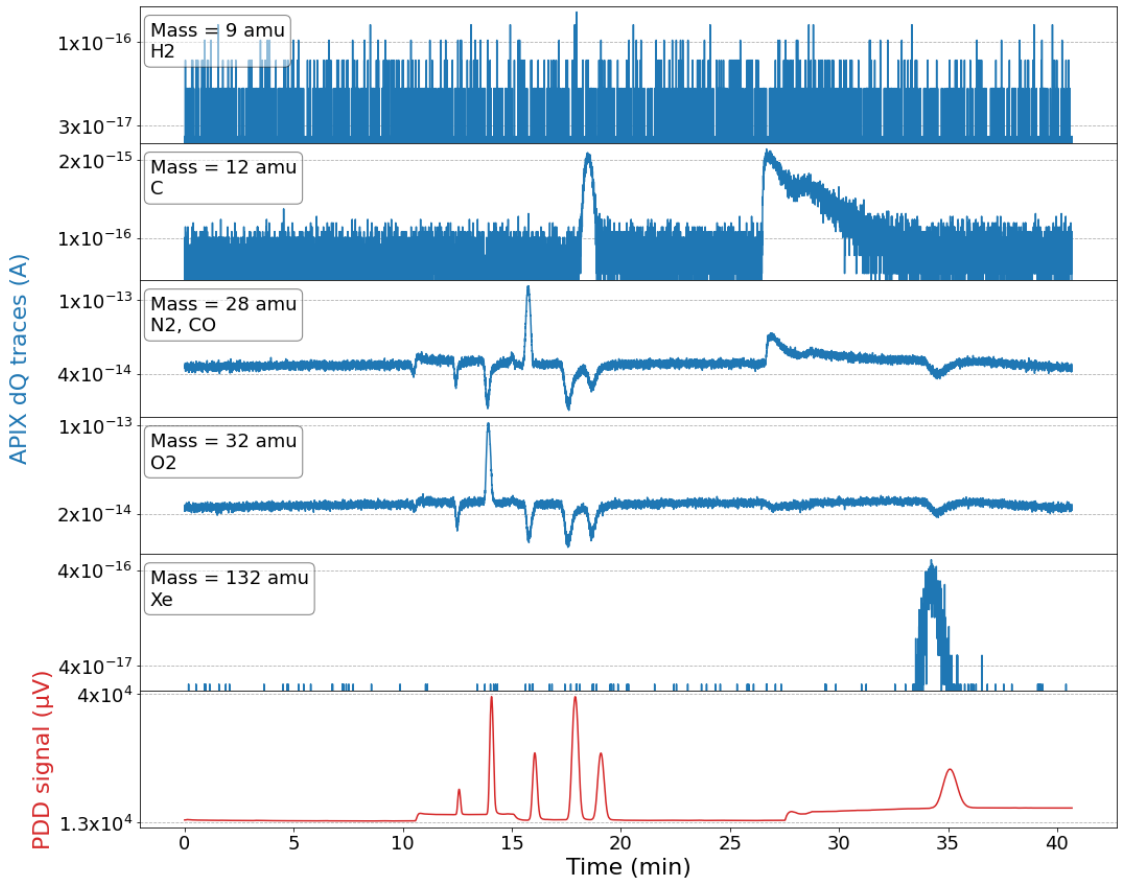

Figure 3.15.: Top panels: calibration spectrum of several APIX dQ traces. Bottom panel: a similar spectrum from the PDD.

To investigate the reason of this, one should take a look at the background of the GC. Figure 3.16 shows some traces and PDD signal for a background measurement. In the PDD there is some structure when switching the valves of the GC, and it is possible to see from the APIX dQ traces that it is due to N_2 and O_2, most likely some air injection in the system due to valve switching.

Comparing the distribution of the trace baseline of the APIX dQ alone, and the APIX dQ combined with the GC shows that the latter introduces a lot of air. Figure 3.17 plots the baseline distribution of the O_2 trace for the APIX dQ alone (blue), the combination with the GC when the purple valve is open and V3 closed, and the baseline when a background GC measurement is running. In particular, the opening of V3 causes an increase of the background of ~ 20 times.

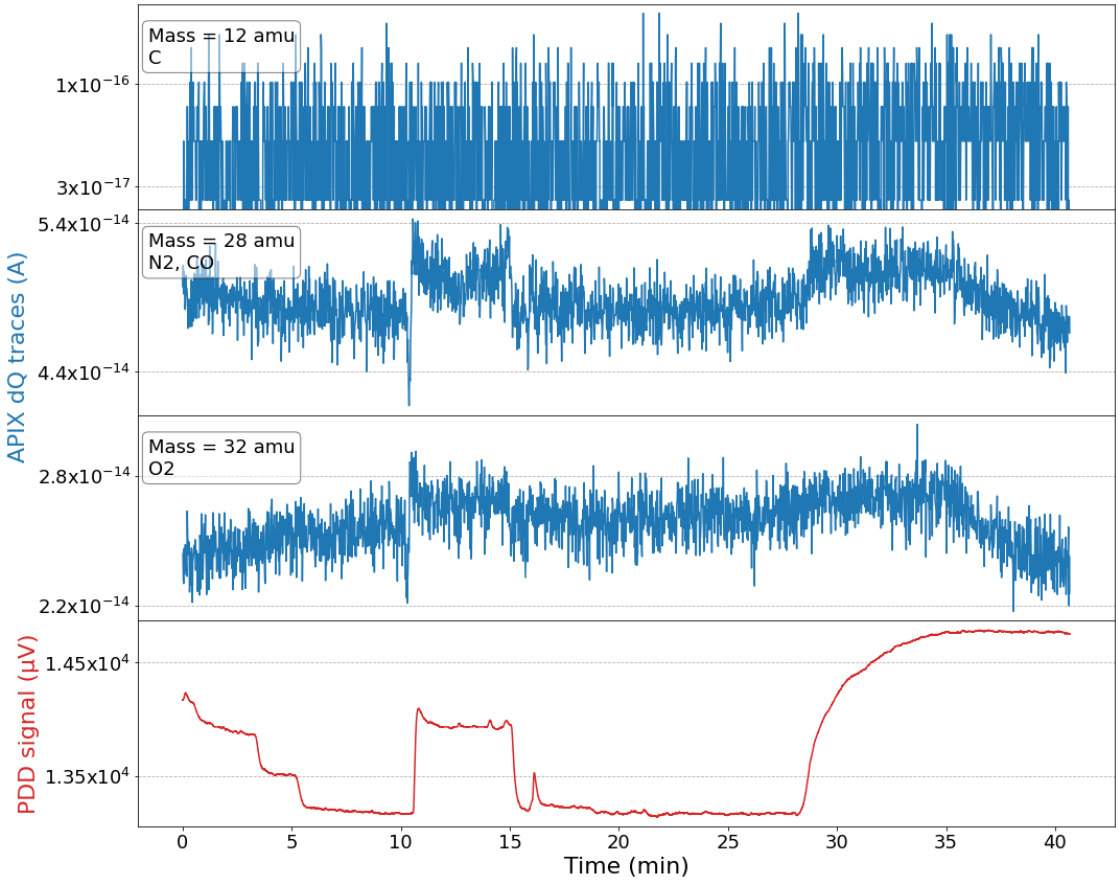

Figure 3.16.: Top panels: background spectrum of N_2 and O_2 traces. Bottom panel: background spectrum from the PDD.

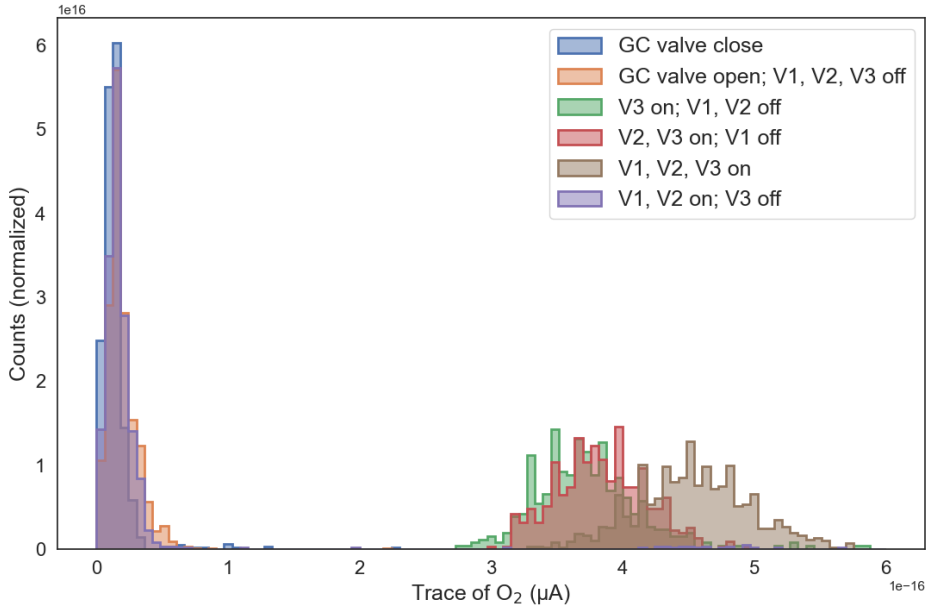

Figure 3.17.: Histograms of the APIX dQ background when opening the GC valve of the gas blender and operating the valves in the GC. The data is normalized.

The reason for this behaviour is that the tightness standards for the GC ($\mathcal{O}$(ppm) level) are different from the ones of the APIX dQ ($\mathcal{O}$(10ppt) level). Nontheless, these results prove that it is possible to use the APIX dQ in combination with a chromatography column to measure a chromatography spectrum. This GC system is used as a starting point to build a a new optimized custom-made chromatography setup that is presented in section 3.6.

3.6 Custom chromatography gas system

In parallel to the construction of a new chromatography gas system, other changes are done in the APIX dQ gas system. In particular, the APIX dQ gas blender has two problems that are not compatible with our needs:

1. There is no way to have a "background only" measurement: the bulk gas is the sample gas.

2. A flow of 5 std l /min of bulk gas is needed. We rely on commercial helium supply to sustain this flow that needs to be avoided in the future for economical reason. Since 4 std l/min are vented directly from the BPR, a lot of the helium supplied to the system is not actively used.

The new gas system will then replace both the GC gas system and the APIX dQ gas blender. It must meet the features from both the gas blender and the GC:

- Stable flow of $\sim$ 1 std l/min and pressure of $\sim$ 1000 mbar in the ionization chamber.
- Leak tight to $< 10^{-9}$ mbar l/s.
- Small dead volumes to reduce tailing effects.
- Constant temperature of the chromatography column.

The new system will also need to allow the same operation as the old system:

- Dilution of the calibration gas.
- Dilution of the xenon sample (if needed).
- Time cut of xenon to protect the APIX dQ.
- Switching between helium (for measuring) and nitrogen (for APIX dQ protection).

The result is presented in figure 3.18.

The improved system is built in stainless steel with Swagelok VCR® connectors, whose leak rate is rated $< 4 \cdot 10^{-9}$ std l/s[78]. It is comprised of an upper part for the upkeep only of the APIX dQ, and a lower part for chromatography. The upper part has a three way valve (V2) that allows to choose to flush the APIX dQ either with helium or with nitrogen, and a regulating valve (RV1) that allows to set the desired flow. MFC3 from figure 3.5 is still in use but, as the maximum gas flow is now close to the set point, it can not regulate the flow and it is instead used only as a readout. To monitor the pressure in

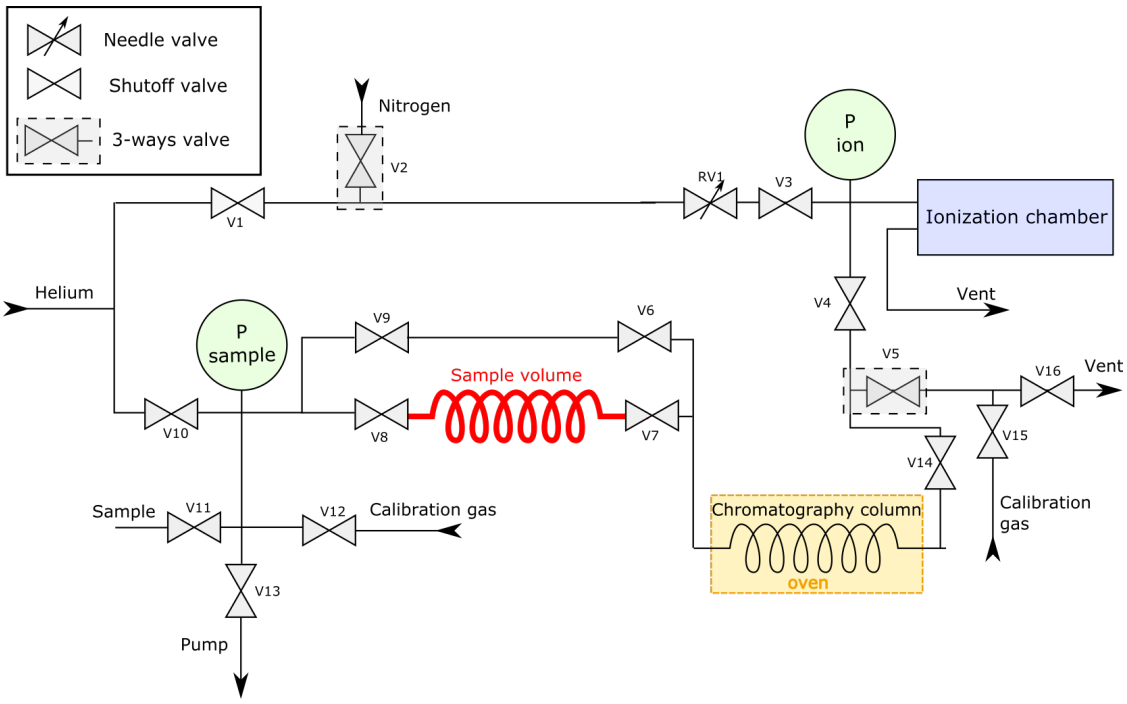

Figure 3.18.: Scheme of the new APIX dQ chromatography gas system.

the ionization chamber, a new pressure gauge MSD 2.5 BAE from Greisinger[7] is installed. Just before the ionization chamber, a particle filter (removal rate: 99.9999999% removal of all particles down to 0.003 µm[8])is installed to avoid debrees to occlude the AIPX dQ orifices.

The bottom side contains the chromatography column and all the ports for connecting the calibration gas and the sample vessel. The chromatography column can be exchanged and several materials were tested to find the most suited ones. The column is situated in an oven that can reach uniform temperatures up to 150°C: changing the temperature leads to a change od the adsorption reaction and therefore a change of the travel time of the impurities in the column itself. In addition the column can be baked up to 350°C with an extra heating tape. The tests on the chromatography columns are reported in section 4.1.

There are 2 ways to calibrate the APIX dQ with this new setup:

1. Through valve V15 (right side), bypassing the column and going directly in the ionization chamber. This mode is similar to the old gas blender, although with the current setup it is not possible to quantify the exact amount of calibration gas reaching the ionization chamber. Nevertheless, this calibration is useful when a constant stream of calibration gas is needed eg. for mass alignement.

2. Through valve V12 and the chromatography column. This mode allows to have very similar condition for measuring a sample and a known amount of calibration gas

[7]https://www.greisinger.de/p/handmessgeraete-und-sensoren/druck/sensoren-edelstahl/absolutdruck/msd-2-5-bae/600585/
[8]https://files.valinonline.com/userfiles/documents/mott-pou-gas-filters.pdf

and it is extensively used for the rest of this work. The calibration gas dilution is achieved by inserting a controlled pressure of calibration gas in the sample volume and using the bulk gas to dilute it.

Two pressure gauges are used for covering a pressure good pressure range: a MSD 6 BAE from Greisinger[9] to measure in range $1 - 6000$ mbar and a CMR 363 from Pfeiffer Vacuum[10] for the rate $10 - 10^{-4}$ mbar. The usual inlet pressure is around 2.5 bars, meaning that dilution factors up to $1/10^6$ can be achieved.

In a similar manner as with the GC, the gas that needs to be measured (calibration or xenon sample) is inserted in the sample volume at the desired pressure, while the APIX dQ is only flushed through the upkeep side (V10 and V4 closed). When the sample preparation is complete, the sample volume is closed and the lower part is opened to the APIX dQ again using the bypass between valves V9 and V6. Then it is necessary to wait 5 minutes for the system to equilibrate, and the bypass is closed while the sample volume is open, injecting the sample in the chromatography column. The of the flow instability from this operation is very small and it lasts only for a few seconds, thus giving a stable baseline for the whole measurement. The valves V4 and V5 allow to decide whether to send the sample to the APIX dQ for measuring, or to the vent when removing xenon. In addition, in this configuration there is no need to loose part of the sample to the vent as in the setup in section 3.5, thus saving more of the sample.

As the insertion procedure is performed in vacuum, the xenon samples can in principle have any pressure, with the caveat that the smaller the sample pressure, the bigger the sample dilution. The xenon samples are contained in stainless steel vessels that have a volume of ~ 250 ml, which is enough to perform a measurement 4 times with consistent pressure.

3.6.1 Background of the custom chromatography system

The analog scan of the background of the new setup is compared with the background using the gas blender in figure 3.19. It is hard to compare the peaks absolute height due to several change of conditions of the APIX dQ, but we can use the water peaks as a benchmark since we do not expect the internal background of the APIX dQ to have changed. In addition, the settings of the QMS were improved: the masses have been re-aligned and the RF generator settings have been changed in order to have wider peaks, which allow a more stable data taking in the MIM mode.

With this setup, the height of the peaks corresponding to air (oxygen and nitrogen) is lower compared to the peaks corresponding to water, which means that less air is present in the background. This is an indication that, even with the high overpressure of the gas blender (5 bar), there was still a small amount of air leaking in the system: this problem was solved with the current setup.

With this air leak gone, now the biggest background is due to argon at mass 40. As already stated in 3.3, this background is due to argon contamination of the commercial

[9] https://www.greisinger.de/p/handmessgeraete-und-sensoren/druck/sensoren-edelstahl/absolutdruck/msd-6-bae/600592/

[10] https://www.pfeiffer-vacuum.com/en/products/measurement-analysis/measurement/activeline/activeline-gauges/4379/cmr-363-10-hpa-f-s-8-vcr

helium used as bulk gas. The hot gas purifier is not able to remove noble gases, so the only way to remove argon is with cryo-trapping. As the freezing temperature of argon is −189°C, this is not possible in the current setup

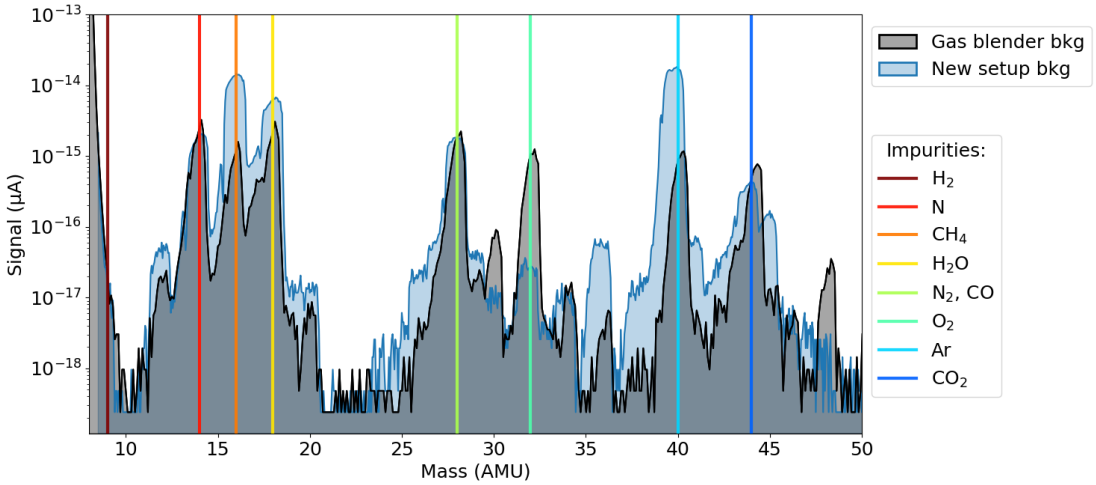

Figure 3.19.: Comparison of the background with the gas blender and the new background (without chromatography column). The masses in the new background have been realigned and the parameters of the RF generator have been adjusted to have wider peaks.

3.7 Data analysis

As with the GC setup explained in section 3.4.1, a measurement starts when the sample is injected in the column. The APIX dQ is running continuously in MIM data taking mode, as for the setup in section 3.5.1. However, with the new gas system, the injection valves are not automatic and the injection of the sample is performed manually. There is still a small amount of air injected in the system due to valve operation, but it does not behave like a constant leak and the baseline doesn't have a step structure like in figure 3.16.

There are two steps for analyzing the chromatography data of the APIX dQ:

1. Quantify the APIX dQ response for each trace impurity.

2. Build a calibration curve to relate the peak area with the impurity concentration.

3.7.1 APIX dQ response

The MIM returns a current per time bin. The current value can be easily converted into ion counts if we know the µA induced by a single ion. This minimal unit depends on the settings of the amplifier of the QMS, so it doesn't change for the different traces. It can be changed by the operator adjusting the discriminator threshold (used to clean the electrical noise of the APIX dQ, see 3.3), or by changing the integration speed, but once these values are set, it stays constant.

It is then possible to exploit the fact that some masses, like krypton, have a very small internal background, which means they can have zero or one count in a time bin of the MIM. By finding the time bins with one count, one can extract the minimal current unit and we can divide the MIM current value to have the ion counts. For our setup, the minimal current unit given by the APIX dQ is $\mathcal{O}(10^{-18}\text{A})$.

Once we have the ion count, we can then use the total number of counts in a peak (N_{peak}) as APIX dQ response. It can can be calculated as the difference between the counts in the time interval where we expect a chromatography peak (N_{on}) and the number of counts expected from the baseline (N_b).

$$N_{peak} = N_{on} - N_b \tag{3.4}$$

It is necessary to determine the peak time interval and a background region that will be used to evaluate the baseline (see figure 3.20). Both of them are determined using calibration data and have some extra room to accomodate for the fact that, since the sample injection is manual, there can be some small variation between datasets ($\mathcal{O}(10\text{s})$). In general, these regions do not change unless the chromatography column conditions change and are set at the start of a measurement cycle. There can be small differences due to the helium flow, but this is cross-checked every day and adjusted if needed.

It was not possible to find a fit function that is able to fit the peak shape in a precise manner, especially when the peaks are small. For this reason, instead of modelling the peak shape, a simple counting approach is used for estimating N_{on}. The baseline of the traces extracted from the regions adjacent to the peaks is also not constant, but shows a linear trend. This can be explained by several factors:

- All contaminants which have no reservoir decrease over time with the helium purging. However, this causes a decreasing trend only for the dominant impurities: all the others would increase given the improved ionization efficiency.

- Some impurities are loaded in the system for loading the column with oxygen (see 4.2). They then decrease with an exponential trend, but the data taking happens far away from the loading, so that we can approximate it with a line.

We can then model the baseline with a linear function:

$$f_{baseline} = \alpha + \beta \cdot x \tag{3.5}$$

Figure 3.20 shows an example of a calibration including the fit of the baseline function and figure 3.21 shows the residuals[11]. The baseline fit is performed in the background region (red shaded in figure 3.20). Part of the region after the peak is not fitted due to possible instabilities in that region. The signal region is shaded in blue and we can define its extreme time bins $[s1, s2]$.

If the fit is acceptable, the residuals are distributed according to a normal distribution, with mean equals 0 and standard deviation equals one. The outstanding exception is krypton, which will be explained in detail in 3.7.3.

[11] Each residual is $(y - y_{fit})/\sigma_y$

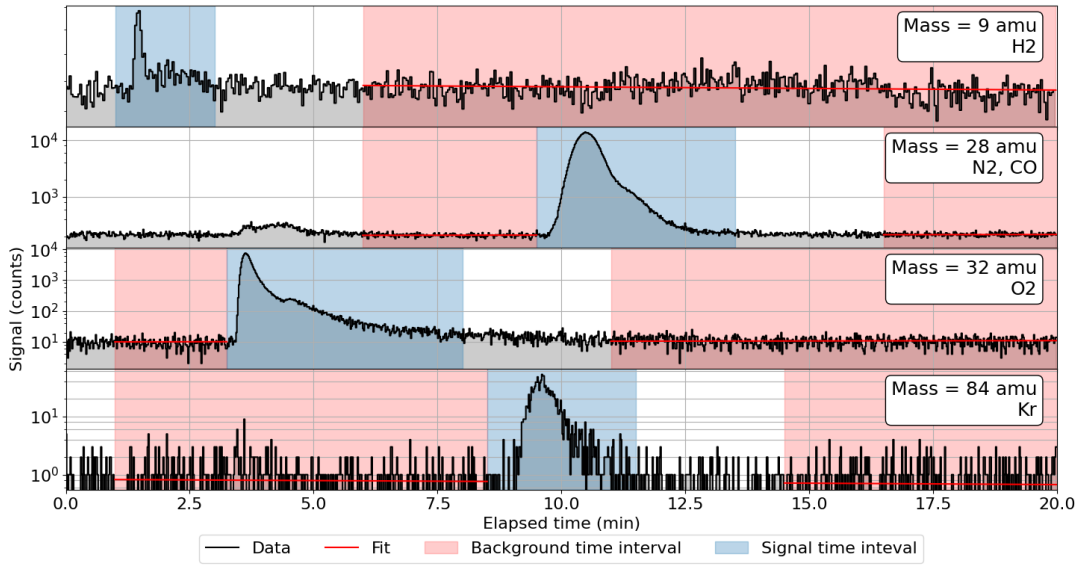

Figure 3.20.: Typical measurement of a calibration sample. All the traces have been converted to counts. The red shaded region is the one used for fitting the background while the blue shaded region is the one . The solid red line is the fit.

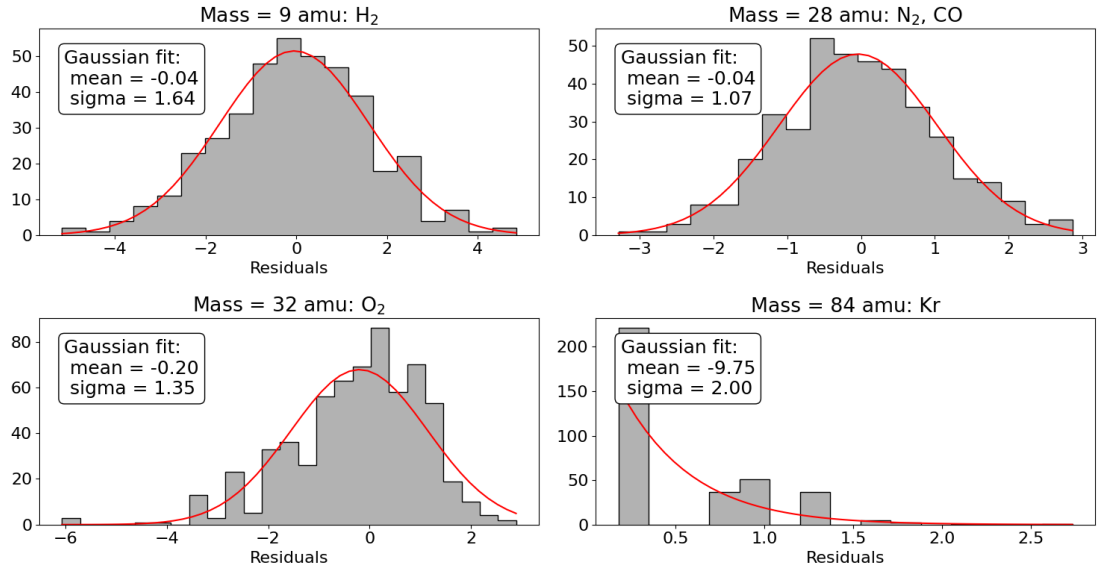

Figure 3.21.: Residuals of the baseline fits for each trace. All the residuals except krypton distribute around a unitary normal distribution.

For everything except krypton, we can then calculate N_b as the sum of $f_{baseline}$ in each bin in the peak region (with n_{peak} being the total number of bins in this region) :

$$N_b = \sum_{s_1}^{s_2} f_{baseline}(i) = n_{peak} \cdot \langle h \rangle \tag{3.6}$$

We can calculate the average height of a bin in this region with an integral:

$$\langle h \rangle = \frac{1}{s_2 - s_1} \int_{s_1}^{s_2} f_{baseline}(x)\mathrm{d}x = \int_{s_1}^{s_2} (\alpha + \beta \cdot i)\mathrm{d}i = \alpha + \frac{\beta}{2}\frac{(s_2^2 - s_1^2)}{(s_2 - s_1)} \tag{3.7}$$

The variance of N_b is

$$\sigma_{N_b}^2 = n_{peak}^2 \left(\sigma_\alpha^2 + \sigma_\beta^2 \left(\frac{1}{2}\frac{(s_2^2 - s_1^2)}{(s_2 - s_1)} \right)^2 + \frac{(s_2^2 - s_1^2)}{(s_2 - s_1)} \sigma_{\alpha\beta} \right) \tag{3.8}$$

where σ_x^2 and σ_{xy} are the variances and covariances from the fit. Combining equations 3.4 and 3.6 we can calculate N_{peak}:

$$N_{peak} = N_{on} - n_{peak} \left(\alpha + \frac{\beta}{2}\frac{(s_2^2 - s_1^2)}{(s_2 - s_1)} \right) \tag{3.9}$$

Since we are simply counting the events, $\sigma_{N_{on}}^2 = N_{on}$, and the variance of N_{peak} is:

$$\sigma_{N_{peak}}^2 = N_{peak} + \sigma_{N_b}^2 \tag{3.10}$$

3.7.2 Decision threshold

The decision threshold is defined as the smallest number of N_{peak} that we can measure over the baseline N_b with 95% confidence level. From looking at the residuals distribution in figure 3.16, we make the assumption that N_b is normally distributed (reasonable since it is $\mathcal{O}(100)$ per time bin). For a normal distribution, the 95% quantile corresponds to 1.649σ, which is then used as decision threshold. A signal is found if

$$N_{peak} > N_{thres} = 1.649\,\sigma_b \tag{3.11}$$

This evaluation is done separately for each measurement since the APIX dQ response can vary in different periods due to the different detector conditions and the baseline level.

3.7.3 Krypton

Figure 3.21 shows how the residuals of the linear fit of the krypton baseline do not have a normal distribution. This is due to the fact that krypton has very few events per time bin, < 10 compared to $\mathcal{O}(100)$ of the other traces: figure 3.22 shows a histogram of the entries in each time bin in the background region for the krypton trace, and it is possible to see how most of the time bins are empty. This discrete distribution can not be fit with a gaussian, but it also does not have a poissonian distribution.

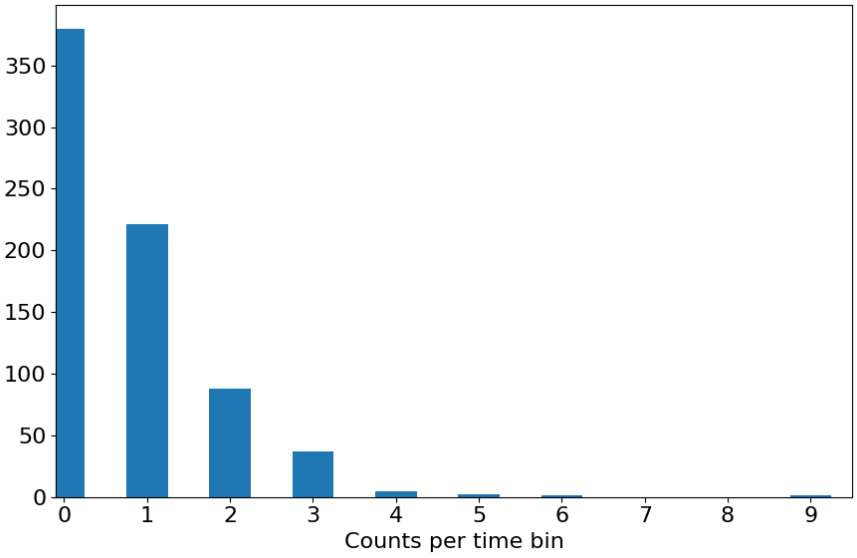

Figure 3.22.: Example of the distribution of counts per time bin for the krypton trace.

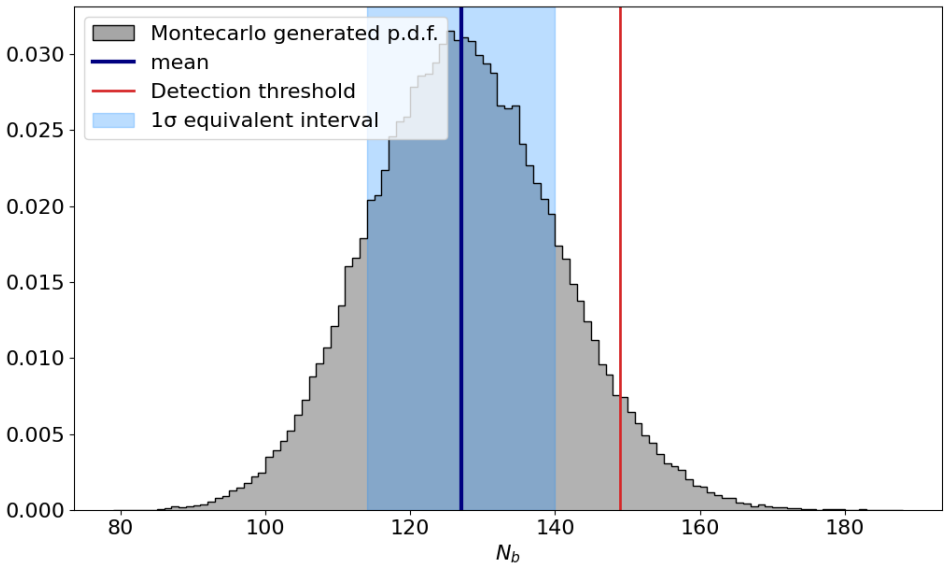

Figure 3.23.: probability density function (p.d.f.) of $\tilde{N}_b$ using Monte Carlo data.

In order to estimate N_b, we make use a small Monte Carlo simulation: we can construct a discrete p.d.f. of the expectation value for each time bin from the histogram of figure 3.22. As for the previous analysis, each histogram, and consequently each N_b, is calculated separately for each data set. From the p.d.f. of the expectation value per time bin, we can construct a new p.d.f. for N_b: n_{peak} random values are generated according to the

bin height p.d.f. and N_b is the sum of these values. 10^5 $\tilde{N}_b$ are generated and used to calculate p.d.f. (figure 3.23). As $\mathcal{O}(n_{peak}) \simeq 100$, the resulting $\tilde{N}_b$ p.d.f. tends towards a gaussian distribution, even though it is asymmetrical and it has a tail at high $\tilde{N}_b$ values. From this p.d.f., we can extract the mean $\langle N_b \rangle$, which is used in equation 3.4, and we can use the quantiles at 32 and 68% to calculate its equivalent 1σ error, which in this case is asymmetric. Finally, we can calculate the decision threshold N_{thres} at 95% confidence level using the 95% quantile.

3.7.4 Calibration curve

Once N_{peak} is calculated, it is possible to construct a calibration curve as in figure 3.4 for our setup. As calibration standard, we use a calibration gas from AirLiquide [12] with Helium 6.0 and a known amount of other impurities. Since the shelf time of these mixes is 1 year, several of them were used in this work (see appendix A).

The pressure gauges are used to insert a known amount of calibration gas at a known dilution. In general, defining p_{sv} as the pressure of calibration gas inserted in the sample volume, p_{bulk} the final pressure after diluting with helium, the measured concentration of calibration gas is:

$$C^{cal}_{meas} = C^{cal}_{original} \frac{p_{sv}}{p_{bulk}} \tag{3.12}$$

Since all the variables are not correlated, the variance is

$$\left(\frac{\sigma_{C_{meas}}}{C_{meas}}\right)^2 = \left(\frac{\sigma_{C original}}{C_{original}}\right)^2 + \left(\frac{\sigma_{p_{sv}}}{p_{sv}}\right)^2 + \left(\frac{\sigma_{p_{bulk}}}{p_{bulk}}\right)^2 \tag{3.13}$$

The calibration gas has an uncertainty of $\sim 10\%$ and the pressure gauges an error of $\sim 1\%$, thus the calibration gas uncertainty dominates the error. The only exception is when measuring $10 < p_{sv} < 100$ mbar, since this range is too high for the more precise CMR Pfeiffer Vacuum gauge and the MSD Greisinger gauge's precision is 1 mbar.

Then changing the p_{sv} of calibration gas, we can change the dilution factor of the calibration gas itself and measure different concentration of the calibration gas. We can then plot in figure 3.24 N_{peak} versus the concentration of the calibration gas: The points are lying one a line in the log-log space. Since the data points have error both on the x axis (from the calibration gas and dilution uncertainties) and on the y axis (from the error on N_{peak}), the total least square method is used for fitting (see [79]).

A N_{peak} measurement of a xenon sample is then represented as an horizontal line in figure 3.24. By calculating the intercept of the line with the calibration fit, it is possible to extract the concentration. If γ and δ are respectively the slope and intercept from the fit:

$$\log_{10} N_{peak} = \gamma \log_{10}(C^{sample}_{meas}) + \delta \tag{3.14}$$

[12] https://mygas.airliquide.de/

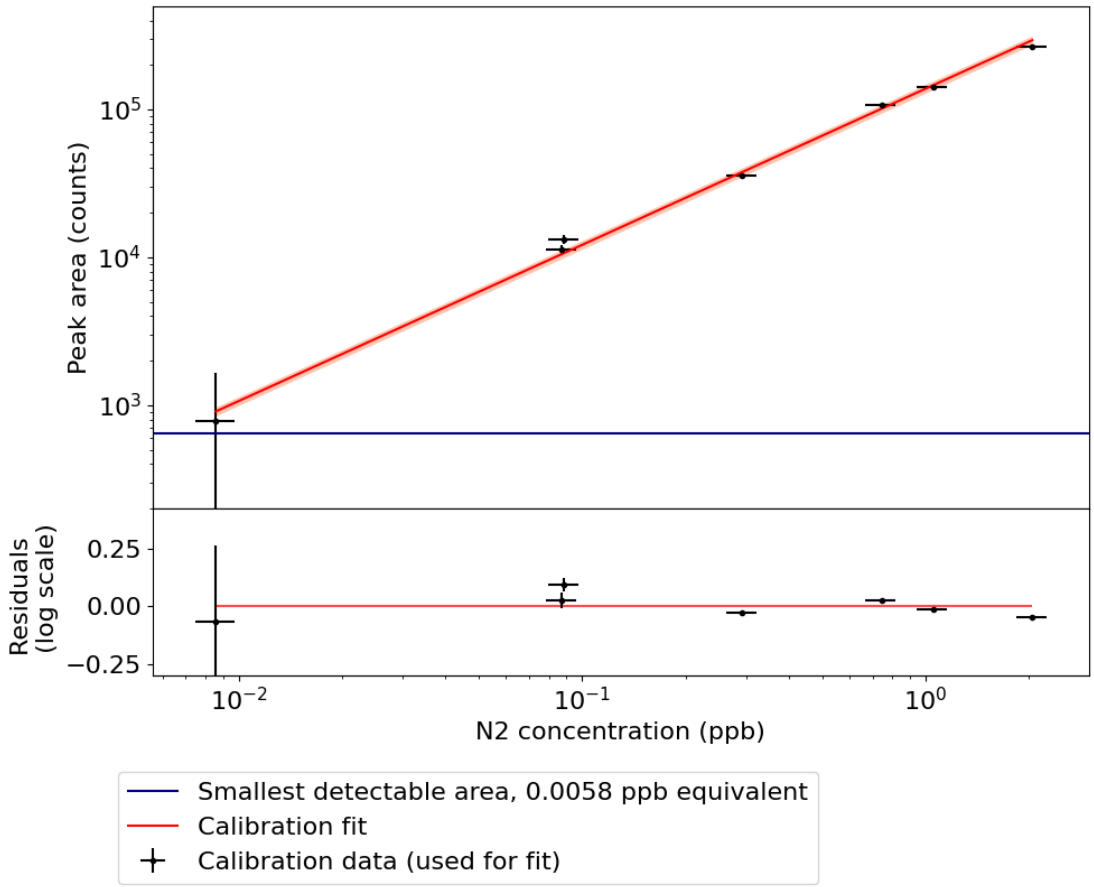

Figure 3.24.: Calibration of the APIX dQ nitrogen trace. The calibration fit (red line) is linear and the decision threshold is the solid blue line.

which, solving for C_{meas}^{sample}, leads to:

$$C_{meas}^{sample} = \left(\frac{N_{peak}}{10^{\delta}}\right)^{1/\gamma} \tag{3.15}$$

Using the error propagation formula, the error is:

$$\sigma_C = C_{meas}^{sample} \sqrt{\left(\frac{\sigma_{N_{peak}}^2}{\gamma^2 N_{peak}^2} + \frac{\ln^2(10)\sigma_\delta^2}{\gamma^2} + \frac{\sigma_\gamma^2}{\gamma^4}\ln^2\left(\frac{N_{peak}}{10^{\delta}}\right) + 2\frac{\ln(10)}{\gamma^3}\ln\left(\frac{N_{peak}}{10^{\delta}}\right)\sigma_{\gamma\delta}\right)} \tag{3.16}$$

where $\sigma_\gamma^2, \sigma_\delta^2 \text{and} \sigma_{\gamma\delta}$ are given by the fit and $\sigma_{N_{peak}}^2$ is calculated in subsection 3.7.1. If the sample was diluted, to get the real concentration it is sufficient to invert equation 3.12

$$C_{original}^{sample} = C_{meas}^{sample} \frac{p_{bulk}}{p_{sv}} \tag{3.17}$$

And the variance can also be calculated in a similar way as in equation 3.13.

Finally, the smallest detectable concentration C^{thres} is also calculated in the same manner, sing N_{thres} from section 3.7.1.

$$C^{thres} = \left(\frac{N_{thres}}{10^{\delta}} \right)^{1/\gamma} \tag{3.18}$$

When placing an upper limit on the sample, it also needs to be scaled using the sample pressure ratio.

3.8 Summary

In this chapter we presented an experimental technique to measure trace impurities in gaseous samples at the ppt level. The exact thresholds are slightly different from day to day. Table 3.4 reports the lowest thresholds reached for the most important impurities measured in this work.

The APIX dQ is most sensitive for nitrogen. Chapter 4 reports the measurements of the oxygen and nitrogen concentration in XENONnT, and explains why the oxygen threshold is a factor ~ 10 worse. Chapter 5 focusses on the hydrogen measurements, and also similarly explains why hydrogen is in the ppb range.

One special mention goes to argon: most of the calibration gas used in this work do not contain argon (see appendix A), so it is not possible to do a precise calibration. We can however estimate the argon content assuming that argon and nitrogen have a similar response. The reasons for this assumption are:

- They have very similar ionization potentials (see table 3.1), which leads to a similar atmospheric pressure ionization efficiency;
- They have a similar mass, which leads to a similar quadrupole mass filter efficiency;
- They have a non-negligible background (although the background from argon is higher).

With this assumption, we can make a rough estimate of the argon using the nitrogen calibration curve.

Trace impurity	**Decision threshold**
Hydrogen	30 ppb
Nitrogen	15 ppt
Oxygen	150 ppt
Argon	$\mathcal{O}$(10ppt)
Krypton	80 ppt

Table 3.4.: Decision thresholds of the APIX dQ and chromatography combined system

Chapter 4

Measurements of electronegative impurities

In chapter 2 it was introduced how the electronegative impurities in LXe can attach to electrons and reduce the electron life-time. Oxygen and water are the most abundant and electronegative impurities that are expected to contaminate the LXe. While it is possible to evaluate the water content also by its photon absorption [35], the same does not hold for oxygen. This leads to a chicken-and-egg problem, where we need to measure the oxygen to calculate the electron life-time, and we need the electron life-time to measure oxygen.

One way to measure oxygen is using an external setup to monitor the electron life-time, and not the TPC itself, as it is done in XENONnT. In this chapter, we show an alternative way to measure oxygen using the setup from chapter 3.

Section 4.1 introduces some early tests that were performed with different chromatography columns to find the best option for measuring oxygen. Section 4.2 details the calibration differences between oxygen and nitrogen. Finally, section 4.3 reports the results of first sample measured from the gas phase of XENONnT and section 4.4 gives the conclusions.

4.1 Test of chromatography columns

While for the most common chromatography applications the separation power is the most important factor to take into consideration, when the combination of chromatography with mass spectrometry makes a fine separation not necessary: the impurities are divided by atomic mass, thus having more than one impurity eluting at a time from the column does not affect the resolution from the two. This is true if the sample does not have any impurity that exceeds 10 ppm, which would saturate the ionization process. In general, all our samples are expected to be below this level and, if necessary, sample dilution can be used to mitigate this issue.

For this reason, the new setup described in section 3.6 uses only one chromatography column, whose main purpose is to slow down and separate the xenon. To look for the best candidate for our needs, we tested again the two adsorbents from the old GC (molecular

sieve 5Å and Hayesep). Since both of them have known issues which will be exposed later, also a new adsorbent (Shincarbon) was tested.

4.1.1 Molecular Sieve 5Å

Molecular sieves are aluminosilicate minerals, with a large surface and uniform micropores size, 5Å for this work. This adsorbent is used mostly for oxygen, nitrogen and water separation. It was used as the fine separation column in the GC. It is very clean and stable, as it is possible to see from the background analog scan in figure 4.1.

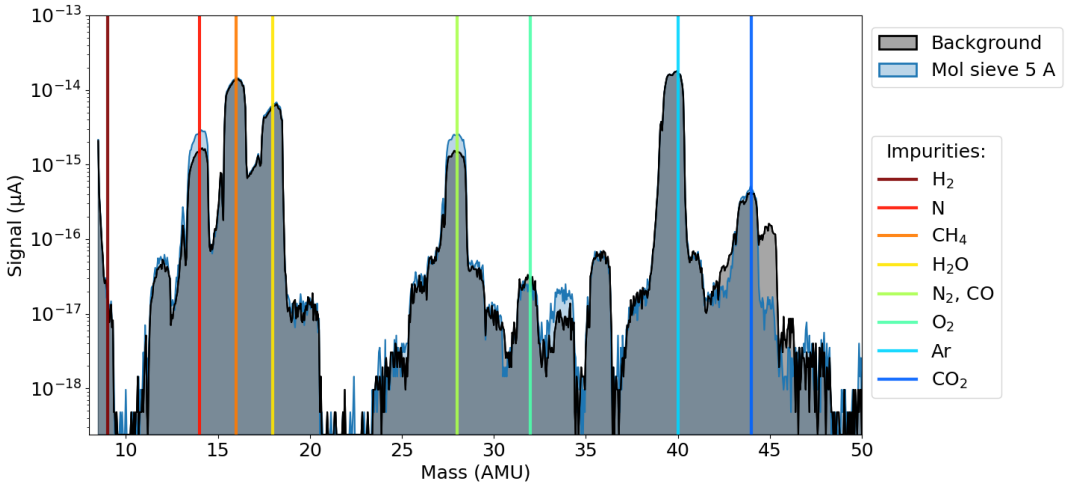

Figure 4.1.: Comparison of the background with and without the Molecular Sieve 5Å column.

The separation of xenon and its impurities is very good (20 minutes in figure 3.15), except for water, which elutes from the column only after xenon. This means that no water is visible with this column. The reason why the Molecular Sieve is not an ideal sample is because it is known to very efficiently trap oxygen, causing a oxygen molecules loss. This problem will be explained in details in section 4.2.

4.1.2 Hayesep

The Hayesep adsorbent belong to the class of porous organic polymers, and have a vast range of applications (gases, light organic compounds and water). They are clean, inert, and stable, and their maximum baking temperature is 150°C[74, Ch. 3]. This adsorbent was used in the pre-separation column of the GC. Figure 4.2 shows a background with and without the Hayesep column, which shows a lot of peaks at high masses. This spectrum is due to a feature of the Hayesep polymers: the "bleeding" effect, which is the constant leaking of content of the column constantly[74, Ch. 3]. A minimal amount of bleeding is expected, and in the case of the GC setup, this bleeding caused an increase in the overall background but it did not hinder a measurement. But for the APIX dQ the bleeding introduces an amount of impurities that saturates the signal. The signal loss can be

quantified taking advantage of a small constant nitrogen leak that was present during both measurements. We can use N (mass=14) and N_2 (mass=28) as a tracer for saturation. If no saturation is present, the two peaks have the same height in both measurements, which is not true looking at the two analog scans: when including the Hayesep column in the system, the N peak is 0.01% lower and the N_2 is 0.30% lower. In conclusion, the Hayesep adsorbent is not a good adsorbent in combination with APIMS. The fact that both this material and the Molecular Sieve are not ideal for our applications prompt some tests of one other adsorbent for the chromatography column.

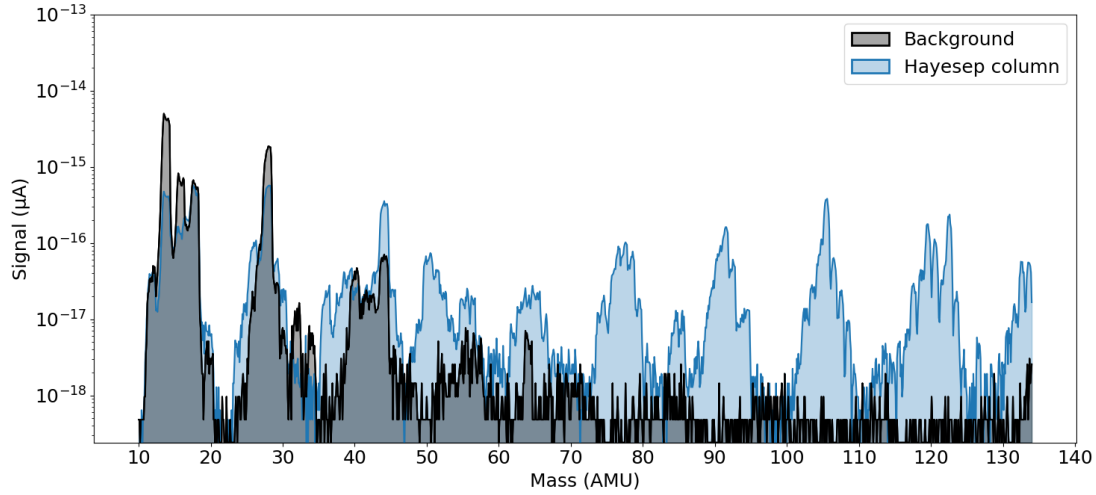

Figure 4.2.: Comparison of the background with and without the Hayesep column. The repeated polymer structure is visible at very high masses. A small nitrogen leak is present in both data set, but the peak is lower when the Hayesep column is included due to the ionization saturation.

4.1.3 Shincarbon

This column is a carbon molecular sieve. It is a proprietary from Sinwa Chemical Industries Ltd and was bought from Restek [1]. According to the seller, it is very stable and it has minimal bleeding. Restek provides a chromatography spectrum as well, which looks promising for our application. The first analog scan of the background from this column showed still some bleeding effect, but after baking the column the background analog scan became clean enough not to cause any saturation. There is a higher background for some masses, even for some monitored peaks like oxygen and nitrogen, but a higher background does not automatically mean a loss of sensitivity, if it is below the saturation threshold of the APIMS process.

[1] https://www.restek.com/row/products/columns/gc-columns/packed–micropacked-columns/4674/

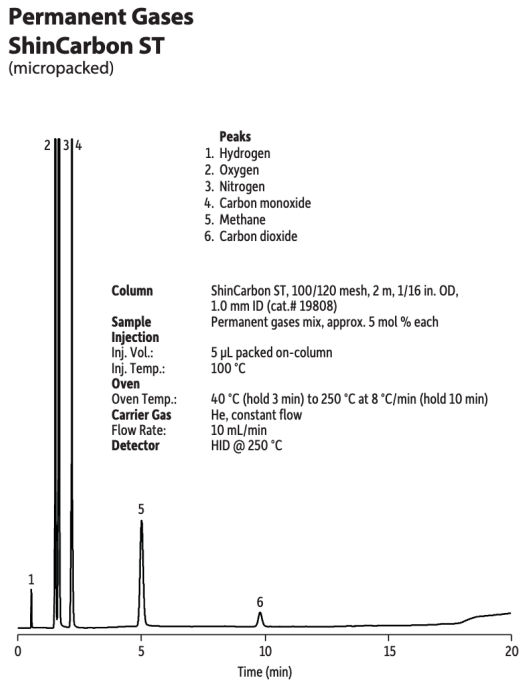

Figure 4.3.: Chromatography spectrum from Restek [80].

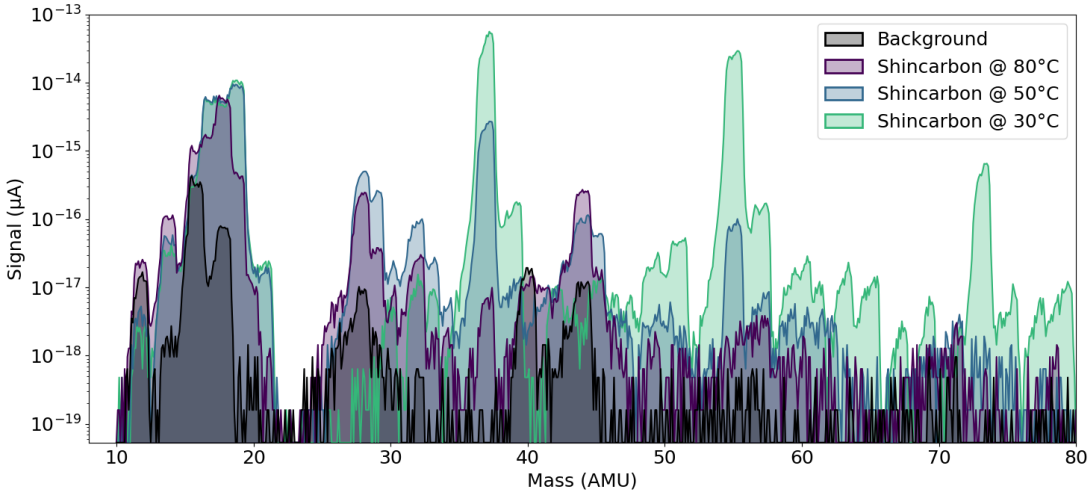

[htb]

Figure 4.4.: Comparison of the background with and without the Shincarbon column, at different baking temperatures. There is an unidentified impurity at mass 37 which dominates the background of the column.

Once the background is clean, a test was done with calibration gas. The results are shown in figure 4.5. The chromatography spectrum looks very different compared to the one in figure 4.3; in particular, there extra features appearing at masses 28 (N_2 and CO) and 44 (CO). What happens is that when the oxygen amount is at $> \mathcal{O}(100\text{ppb})$

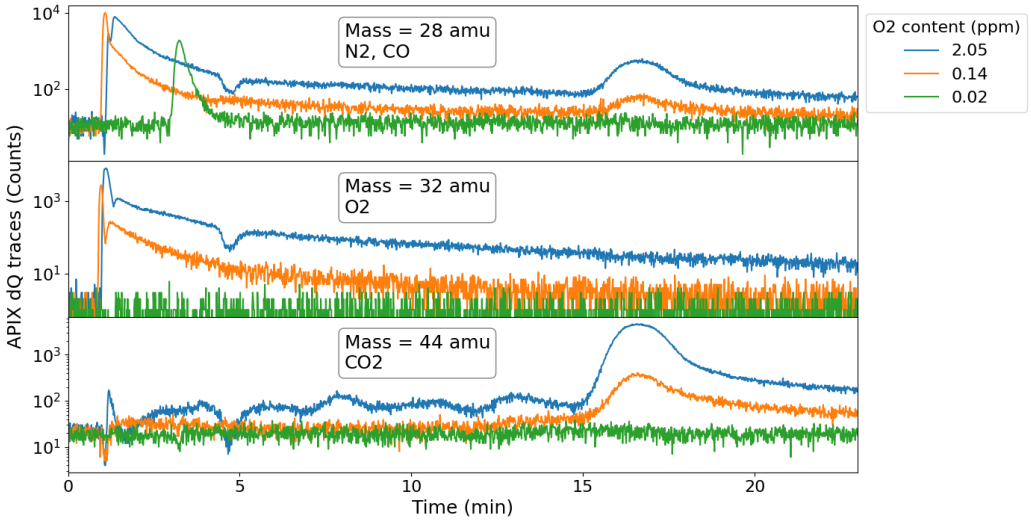

Figure 4.5.: Chromatography spectrum with Shincarbon. The green trace is taken at different flow conditions, which changes the elution time for nitrogen.

level (blue and yellow curve), it gets carbonized by the Shincarbon, forming CO and CO_2 molecules. Both those molecules then move slowly in the column, which creates a shape that is not a clear peak. In addition, CO has an atomic mass of 28, the same as N_2, hence disrupting the N_2 measurements. On the other side, no oxygen is visible when injecting a small amount of oxygen (less than 20 ppb), neither at its mass of 32, nor in the CO or CO_2 traces (the peak at trace 28 is due to nitrogen).

One possible explanation of the difference between figure 4.3 and 4.5 is that Restek works with a calibration gas that has a mix of components at 5% level and a not so sensitive detector, while our calibration has a much lower content (2 to 0.2 ppm) and the APIX dQ is much more sensitive. Carbonization is present also in 4.3 but not visible due to the high oxygen concentration.

In conclusion, Shincarbon can not be used to separate oxygen from xenon due to its efficiency in carbonize oxygen. It was proved however that it has an excellent separation power for noble gases, such as krypton[81].

4.2 Oxygen trapping by Molecular Sieve

From the tests in the previous section, the best candidate for separating xenon from electronegative impurities is the Molecular Sieve 5Å. As written in section 4.1.1, this material is known to trap oxygen, which makes it ideal for noble gas purification([82]). Before using it just to separate oxygen from a mixture, as we do with gas chromatography, it is necessary to load all its trapping sites in order not to loose part of the oxygen signal while the sample travels through the column. This operation is performed by injecting enough oxygen to fill all the trapping sites (the amount of oxygen depends on the weight of the Molecular Sieve in use) and, according to the instructions, should be performed every

time after baking the column. The oxygen is released from the column at temperatures higher than 150°C, so keeping the temperature of the column below this value should lead to no oxygen loss.

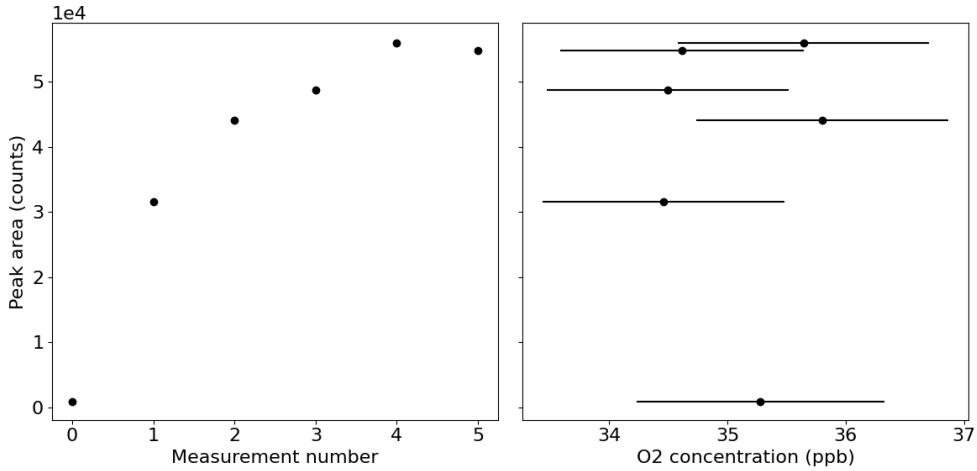

Figure 4.6.: Left: oxygen response during measurements performed in one day. At first the response is very small and it increases with each measurement. Right: same data respect to oxygen amount in the sample volume.

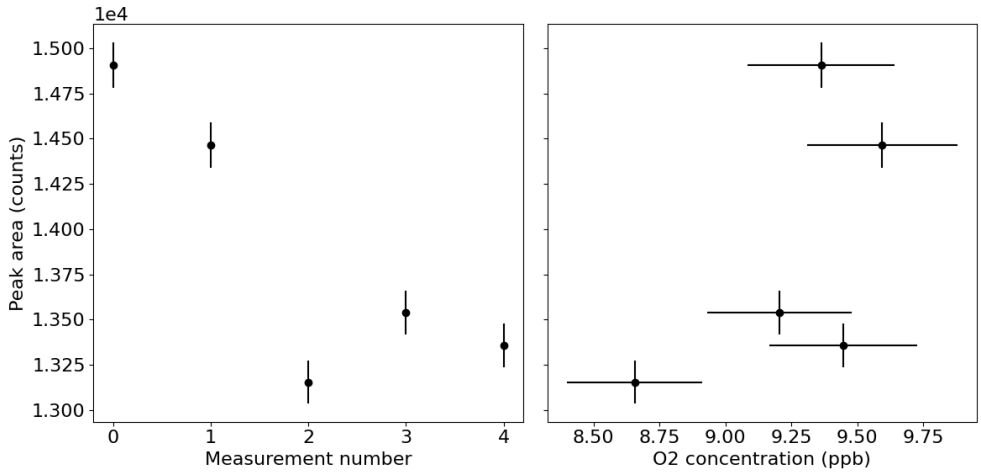

Figure 4.7.: Left: oxygen response during measurements performed in one day after spiking the column with $\sim$ 1ppm of oxygen. The response does not correlate with the measurement number. Right: same data respect to oxygen amount in the sample volume, where now a trend can be seen.

In our case however, it was observed that this precaoutions are not enough. Figure 4.6 shows a series of repeated measurements with ~ 35 ppb of oxygen during one day. It is easy to see that the APIX dQ response correlates very well with the number of the

measurement: it is almost zero at first, and it increases with each measurement until it reaches a saturation point after 4 measurements.

The conclusion from this measurement is that, even at temperatures $< 150°C$, a small portion of the trapping sites of the Molecular Sieve are constantly liberating the oxygen molecules. This portion is negligible when measuring oxygen at $\mathcal{O}$(ppm), but plays a big role at $\mathcal{O}$(ppb). A set of repeated measurements with ~ 35 ppb of oxygen progressively load the sites so that the signal becomes larger, saturating when all the sites are filled around the fourth measurement (figure 4.6 left). In practice, the speed at which the sites are getting freed of oxygen is slower than the oxygen loading from the measurements.

In order to mitigate this problem, the Molecular Sieve temperature was lowered from 60°C (as it was in [61]) to 30°C. This slows down the chemical binding of the gas phase with the Molecular Sieve, which both causes the separation of the column to get worse (but, as already written, it is not a problem for your setup) and at the same time it slows down the liberation of the oxygen from the trapping sites. More important, a big amount of calibration gas, equivalent to ~ 2 ppm of oxygen, is introduced in the column to load all the oxygen sites. As the saturation lasts a few hours, this procedure is repeated 2 to 3 times per day, depending on how many measurements are performed each day, and it greatly improves the stability of the oxygen response. Figure 4.7 shows another set of repeated measurements with ~ 10 ppb of oxygen after the column was saturated with oxygen: this time the APIX dQ response does not relate with the number of measurement, as it was in figure 4.6, but instead it is related to the amount of oxygen introduced in the calibration gas.

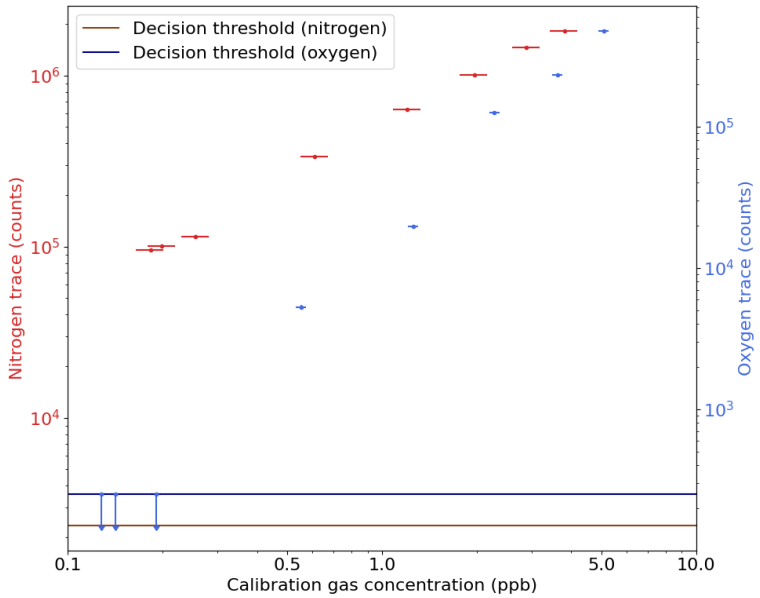

Figure 4.8.: Comparison of the APIX dQ response for oxygen and nitrogen. The lower three points are above the decision threshold for nitrogen but not for oxygen, hence only an upper limit can be placed.

When comparing the APIX dQ response for oxygen and nitrogen, it is still visible that

for oxygen is one order of magnitude lower, which we would not expect from the theory of the ionization (the oxygen has a lower ionization potential than nitrogen, see table 3.1). Figure 4.8 shows a comparison of oxygen and nitrogen calibrations, and it is already visible from the scale how oxygen is falling faster than nitrogen and in general how its response is smaller. This is an indication that part of the oxygen signal is still lost in the chromatography column.

One solution for this problem would be to dope the helium flow with a controlled amount of oxygen in order to load continuously the Molecular Sieve sites. This oxygen should be ultra-pure, as is helium, and must be added after the gas purifier. The oxygen concentration to be injected has to be also small enough so that it does not saturate the atmospheric pressure ionization. A dedicated study needs to be done to evaluate the exact concentration needed, but from the measurements in figure 4.6 we know that a concentration $\mathcal{O}(10\,ppb)$ every 20 minutes (the run time of a single measurement) is sufficient, which means that less than 1 ppb of oxygen in the helium flow is needed.

4.3 Electronegative impurities in XenonnT

A xenon sample was extracted in July 2021, at the beginning of the science run of XenonnT. It is extracted from the gaseous phase, which we know does not reflect the amount of impurities in the liquid phase due to the enrichment of lighter elements in the gas phase. The sample was measured four times on four days. The results are shown in table 4.1.

	Concentration (ppb)		
Date	**Oxygen**	**Nitrogen**	**Argon**
05.08.2021	2.6−	2.1 ± 0.2	−
06.08.2021	$2.5 - 5.2$	2.5 ± 0.3	−
09.08.2021	$0.9 - 3.7$	0.91 ± 0.09	< 0.06
17.08.2021	0.73−	0.48 ± 0.05	< 0.02

Table 4.1.: Measurements of air impurities in the gaseous phase of XenonnT from July 2021. On 05.08.2021 and 17.08.2021 it was not possible to calculate the oxygen upper limit. Argon was only measured in the last two measurements.

There is a systematic effect which causes the calculated concentration to change a factor ~ 3 in the last measurements. This effect is not consistent with the hydrogen measurements (see section 5.3) and it is still under investigation. In addition, during some of the days, the calibration of oxygen showed some instabilities at low concentration (see figure 4.9). Those instabilities are induced by the oxygen trapping described in section 4.2 and indicate that the oxygen concentration in the sample might be underestimated when it is close to the detection threshold.

The calibration data at low concentration falls faster below the detection threshold compared to the linear fit. This means that the real oxygen amount is higher than what measured and the sample oxygen concentration from the global fit can be interpreted as a

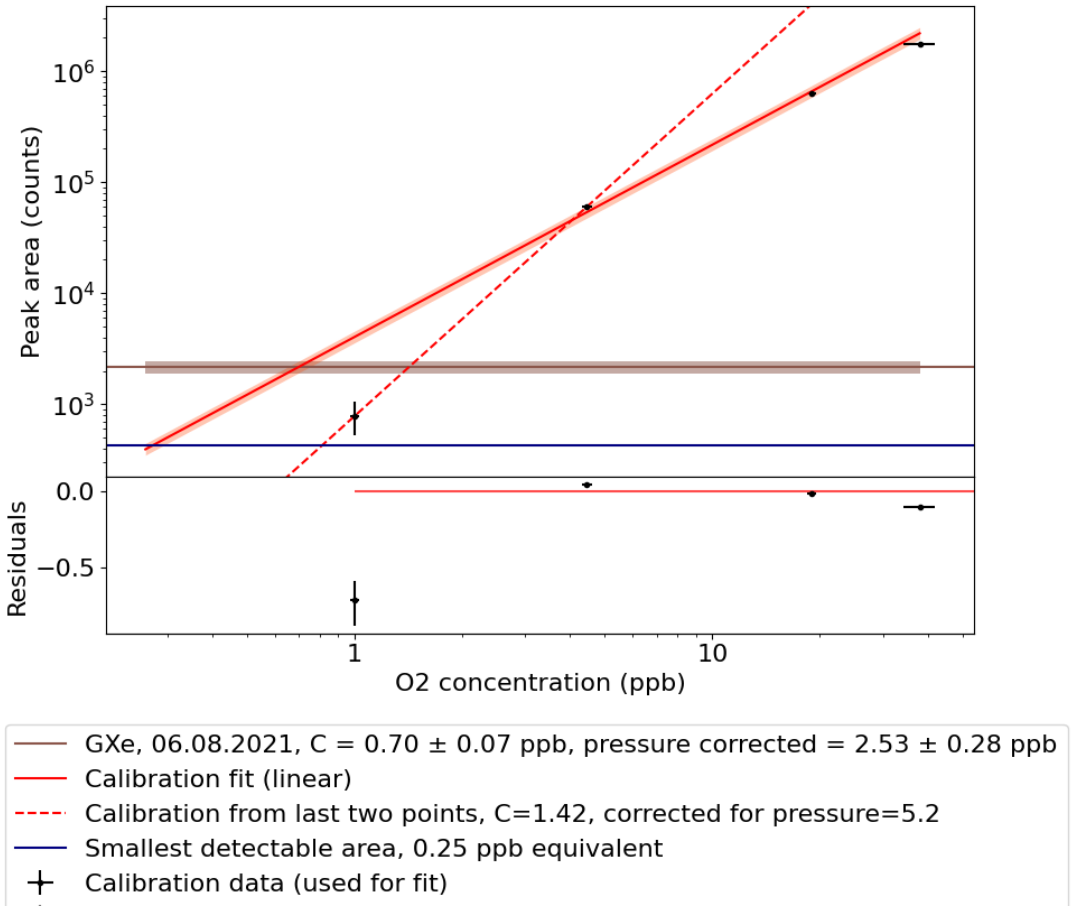

Figure 4.9.: Oxygen calibration curve on 06.08.2021 and GXe measurement of the same day. The last points of the calibration are falling below the detection threshold faster than naively expected from a linear fit. A second calibration curve is constructed with the two lower-most calibration point to have an upper limit.

lower limit. For the measurements on 06.08.2021 and 09.08.2021 it was possible also to construct a new calibration curve using only the two data points at lowest concentration (see figure 4.9). A second value for the oxygen concentration calculated with this low-concentration calibration curve is an upper limit.

4.4 Discussion and outlook

In this chapter, the first measurement of oxygen and nitrogen from the gas phase of XENONnT was presented. The liquid purification system of XENONnT is also equipped with an external purity monitor, which constantly measures the electron life-time independently from the TPC. If we make the assumption that the electron life-time is driven only by the oxygen concentration, that would lead to an oxygen concentration of 20 ppt in LXe (calculated with equation 2.1).

As already written in section 4.3, we expect oxygen, which has a lower boiling point

than xenon (see table 2.1), to be enriched in the gaseous phase. In fact, it is not possible to estimate the vapour pressure of oxygen at the conditions of XENONnT, one would simply expect that all the oxygen is in the gaseous phase. In addition, since the xenon gas phase of XENONnT is recirculated several times per day, we do not expect a static equilibrium, but rather a dynamic one. We can then empirically calculate the enrichment factor, or the solubility of oxygen in LXe ($\alpha^{\mathrm{Xe}}_{\mathrm{O_2}}$) for the case of XENONnT, which is:

$$\alpha^{\mathrm{Xe}}_{\mathrm{O_2}} = \frac{C^{\mathrm{GXe}}_{\mathrm{O_2}}}{C^{\mathrm{LXe}}_{\mathrm{O_2}}} = 35 - 260 \tag{4.1}$$

depending if we take the upper or lower value for the oxygen measurement.

One surprising observation is also that the oxygen amount is higher than nitrogen. Nitrogen and oxygen are removed by two getters in XENONnT. Getters are filled with a zirconium alloy that chemically bound reactive atoms and molecules. It is naively expected that oxygen is bound more efficiently than nitrogen, since it is the most electronegative of two, resulting in an overall lower oxygen concentration in the xenon. This is not what is observed for the sample, which leads to three explanations:

- There is a big oxygen source in the system. It is unlikely because air is the main source of oxygen, and it would contribute more to nitrogen.
- The getter material is saturated in oxygen. The saturation can be monitored through the electron life-time and so far it was not observed.
- The combined efficiency of the getters plus liquid purification system is lower for oxygen than for nitrogen.

The first hypothesis is unlikely, since air is the main source of oxygen, and it would contribute more for nitrogen than for oxygen. The second hypothesis is the most favoured one, even if unexpected. A dedicated study should be done on the performance of the getter material, and in particular on their removal power of different species.

The detection threshold of the system is currently too high to be sensitive to the oxygen concentration in LXe. As written in section 4.2, the limiting factor is the trapping of oxygen by the molecular sieve. The upgrade proposed in section 4.2 would allow to lower the detection threshold for oxygen to a similar level as the one of nitrogen, which would make a direct measurement of oxygen possible also in the liquid phase. This would confirm both the value of $\alpha^{\mathrm{Xe}}_{\mathrm{O_2}}$ and if oxygen is the most relevant impurity for the electron life-time.

The argon concentration was constrained to sub-ppb level and it is confirmed that its contribution is sub-dominant for the XENONnT background, as already mentioned in section 2.3.2.

In the framework of XENONnT, samples will be taken regularly. The LXe is constantly purified, so the APIX dQ can be used as an alternative method to monitor the purification efficiency and verify if the system is at equilibrium. This would also help in identify any possible leak of the XENONnT gas system.

Finally, more broadly, so far we concentrated on oxygen, but the APIX dQ can measure the solubility of several impurities in liquid xenon. This is useful information for identifying the most efficient way to purify liquid and gaseous xenon for future experiments like DARWIN.

Chapter 5

Measurements of hydrogen

Tritium is a possible novel background that was first introduced in [32] as a possible explanation for the excess in the electronic-recoil band at low energies. It can be present in the LXe as either tritiated water or tritiated hydrogen. In this chapter, we focus in particular on hydrogen and we use the APIX dQ to measure its concentration in XenonnT, as an indirect way to constrain HT.

Section 5.1 introduces tritium as a background. Section 5.2 explores one of the manners in which tritium can be introduced in XenonnT. Section 5.3 gives the results for hydrogen measurements in XenonnT and section 5.4 gives the conclusion and an outlook.

5.1 Tritium as background in XenonnT

Tritium (^{3}H) is a trace isotope of hydrogen. It can be spontaneously produced by cosmic radiation, but the major source of it is the accidental release by nuclear power plants or atomic detonation [83]. Its concentration is $5 - 10$ atoms of ^{3}H for 10^{18} atoms of H[84] in water. We assume a similar concentration for HT, but it is worth noting that this value changes depending on the location where it is measured. Tritium is a beta emitter with total released energy 18.6 keV and a half-life of 12 years. As the life-time of a Xenon detector is < 5 years, it can be considered a constant background source.

The excess events observed in [32] is consistent with a concentration of ^{3}H/Xe of $(6.2 \pm 2.0) \times 10^{-25}$ mol/mol (see figure 2.6). Tritium can be present in the system as two species: tritiated water (HTO) and tritiated hydrogen (HT). If we assume the natural abundance of tritium in hydrogen, we would need a combined amount of at least 30 ppb of H_2O+H_2 to explain the excess.

The introduction of tritium can happen in two ways: either from an initial cosmogenic activation [85], or as a constant leak of HTO and HT. As the cosmogenic activation is negligible underground due to the small muon flux, it can only play a role in an initial contamination of the xenon when it is still above ground. However, due to the krypton distillation, we expect the final tritium concentration to be at least as low as the krypton one, in the ppq range, too low to explain the signal.

A second option is the constant outgas of water and hydrogen from the detectors material.

The water contaminating the system can be constrained independently by measuring the light transparency of the xenon [35], and it is, in XENON1T, $\mathcal{O}$(1ppb), around a factor 10 lower than what needed to fully explain the excess. However no independent way to measure HT is possible in XENON1T: if we assume hydrogen behaves in a similar way as oxygen, we would expect also to have a hydrogen concentration $\mathcal{O}$(1ppb), but this was not possible to verify independently. Hydrogen outgassing is a possible contamination source and will be detailed in next section.

5.2 Hydrogen outgassing

As written in chapters 2 and 3, all the gas systems are build in stainless steel, the material of choice for its purity and robustness. During the stainless steel production, hydrogen from the atmosphere is dissolved inside the stainless steel, causing a higher partial pressure of hydrogen in the steel which then slowly outgases[86, Ch. 6]. Hydrogen outgassing is the limiting factor for ultra high vacuum and extra high vacuum system[87].

In an ideal case, the outgassing rate of hydrogen from a 1 mm sheet (a typical thickness of the APIX dQ gas system) of stainless steel when vacuum is at both sides is[86, Ch. 6]

$$R = 1.26 \cdot 10^{-12} \frac{\text{mbar l}}{\text{s cm}^2} \tag{5.1}$$

In practice, the rate can vary greatly due to the surface roughness, the exact production procedure and which temperature the stainless steel was exposed to, so the exact coefficient of the outgassing rate must be verified for each stainless steel volume separately.

The standard procedure to reduce hydrogen outgassing is baking the stainless steel at 950°C temperatures for at least one hour ("vacuum firing")[88]. This method is used in several physics fields where ultra high vacuum is needed, such as gravitational waves interferometers[89] and super colliders[90].

5.2.1 APIX dQ gas system blank

The hydrogen outgassing is visible also in the background of the APIX dQ. When doing a blank measurement, for all the traces the measured N_{peak} is compatible with the statistical fluctuations of the baseline, but hydrogen is an exception: there is a non zero area that is measured in every blank run.

This non-zero blank raises the detection threshold of hydrogen compared to other traces. Figure 5.1 shows a calibration curve for hydrogen and the detection threshold. The calibration data (black) are used to construct the calibration fit (red) as is done section 3.7.4. The detection threshold as defined in 3.7.4 is the dashed blue line and the blank measurements are in light blue (the x position is arbitrary, just to show them on the plot). To calculate the mean value of the blank $\hat{N}^{blank}$ we do a weighted average of all the blanks $N_i^{blank} \pm \sigma_i$, where the weights are defined based on the variance of each measurement:

$$w_i = \frac{1/\sigma_i^2}{\sum_i 1/\sigma_i^2} \tag{5.2}$$

The mean of the blanks is then:

$$\hat{N}^{blank} = \sum_i w_i N_i^{blank} \tag{5.3}$$

And the variance (see appendix B):

$$\sigma^2_{N_{blank}} = \frac{\sum_i w_i (N_i^{blank} - \hat{N}^{blank})^2}{(1 - \sum_i w_i^2)} \tag{5.4}$$

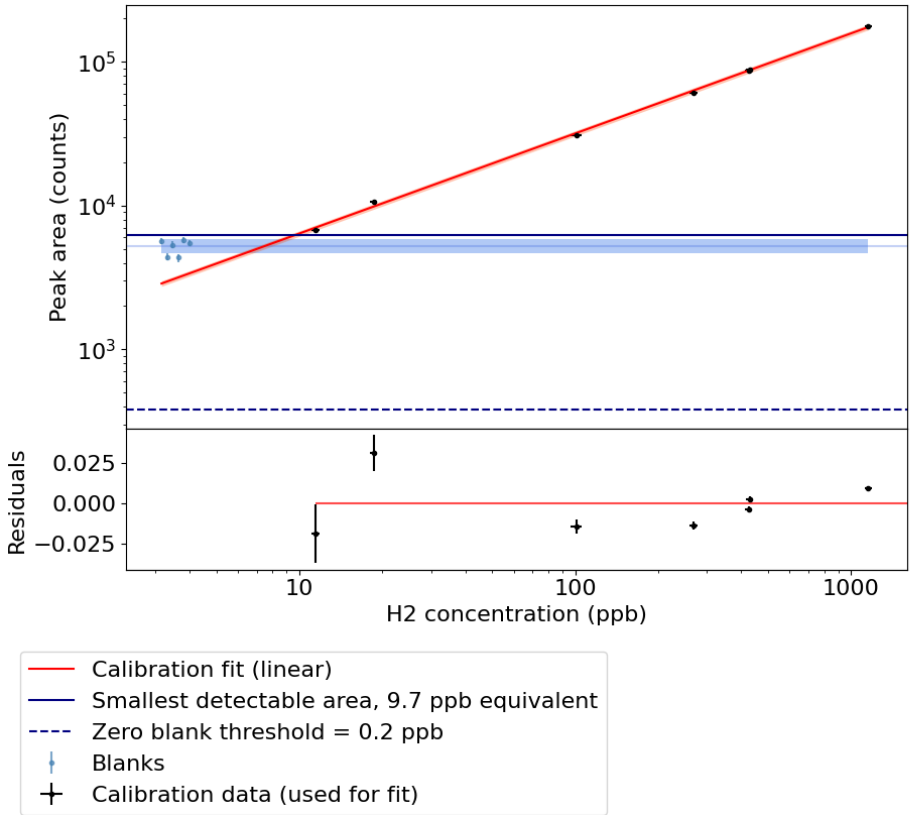

Figure 5.1.: APIX dQ calibration for hydrogen with a non-zero blank. The new detection threshold (solid blue line) is 10 times higher than the threshold calculated from the baseline only (dashed blue line) as for the other traces.

The light blue line is then $\hat{N}^{blank}$ with its 1σ interval and the solid blue line is the new detection threshold placed, as always, at the 95% confidence interval. The detection threshold defined as with only the statistical fluctuation shows that it is possible to achieve sub-ppb sensitivities, provided that this constant hydrogen signal can be eliminated. The gas purifier of the system is already removing all hydrogen that comes from the commercial helium, so the left over component is from the APIX dQ gas system and the APIX dQ itself. To remove hydrogen, vacuum firing the whole system and the APIX dQ ionization chamber is the best solution.

5.2.2 Pipettes vacuum firing

The pipette vessels used to transport the samples from XENONnT to the APIX dQ is also made of stainless steel and thus it also outgas hydrogen. After the sample pipette manufacture, its hydrogen outgas was measured. The pipette was evacuated and filled with ~ 1 bar of purified helium and several days were waited. The helium in the pipette was measured with the APIX dQ several times, extracting ~ 0.1 bar of gas each time which converts in a dilution factor of $\sim 4\%$. The results of these measurements are in figure 5.2, left side, together with the theoretical calculations from equation 5.1 (red dots). After just few days, the concentration of hydrogen in the pipette is at ppm level. If any sample is taken from LNGS, we expect around one week between the sample extraction and the sample measurement (due to the shipping time), which means this outgassing rate is incompatible with our needs of measuring hydrogen in the ppb range. The pipette vessel was vacuum-fired with the exception of the top part of the valves which are not able to withstand such high temperatures, and the measurement is repeated. The new points are shown in figure 5.2(right) and the hydrogen is below the threshold for each measurement, proving the success of vacuum firing as a mean to reduce hydrogen outgassing. For this second measurement, all the measurements have been taken with a dilution factor of $\sim 4\%$ except the last one which had a dilution of 30%, which converts to a lower threshold.

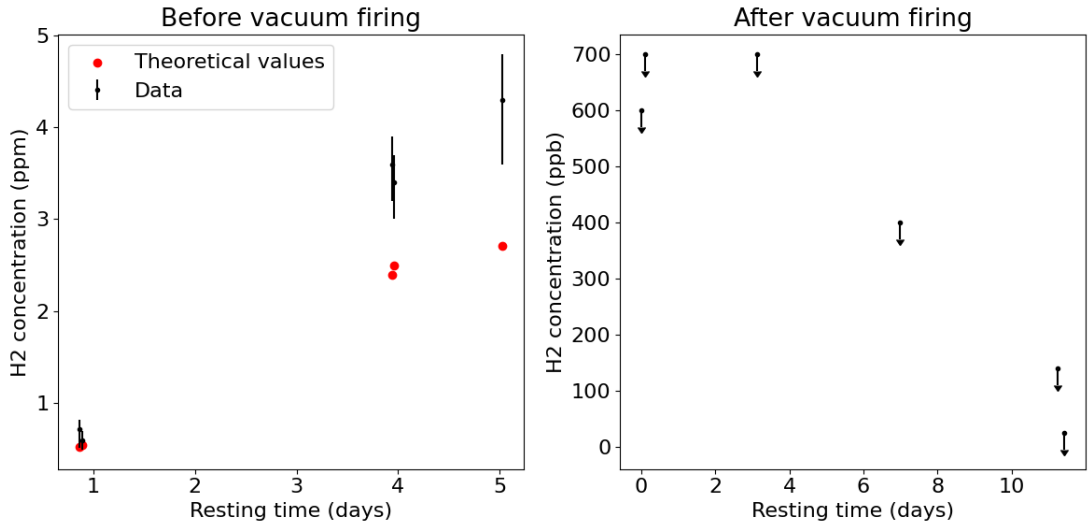

Figure 5.2.: Comparison of hydrogen outgassing of a pipette before (left) and after (right) vacuum firing. The theoretical outgassing values for a pipette without vacuum firing are plotted with red dots. After vacuum firing, no hydrogen is detected in outgassing after more than 10 days. The lower detection threshold of the last point is due to a smaller sample dilutiond.

5.3 Hydrogen in XENONnT

Two samples were measured: one from the liquid phase from March 2021 and one from the gas phase from July 2021 (the same one as in section 4.3). Unfortunately, an air leak was

present during the extraction of the LXe sample, with an air contamination $\mathcal{O}$(ppm). This prevented the measurement of oxygen and nitrogen, but the concentration of hydrogen in air is 0.5 ppm, which means that the total expected hydrogen contamination is well below the APIX dQ detection threshold.

The results of the two samples are given in table 5.1. For the LXe sample we were only able to place upper limits, while the GXe sample has a clear signal.

Liquid Xenon		**Gaseous Xenon**	
Date	**Hydrogen Concentration (ppb)**	**Date**	**Hydrogen Concentration (ppb)**
31.03.2021	< 47	05.08.2021	54 ± 3
16.04.2021	< 408	06.08.2021	71 ± 4
30.04.2021	< 46	09.08.2021	64 ± 4
		17.08.2021	71 ± 4

Table 5.1.: Hydrogen measurements of the XENONnT samples.

The self distillation of light impurities that played a big role for oxygen is expected to be even stronger for hydrogen. The enriched concentration of the gas phase is consistent with the measurements of hydrogen in the liquid phase. Since it was possible to only place an upper limit on the concentration of hydrogen in LXe, we can also only place a limit on the solubility of hydrogen in LXe ($\alpha_{H_2}^{Xe}$)

$$\alpha_{H_2}^{Xe} = \frac{C_{H_2}^{GXe}}{C_{H_2}^{LXe}} > 1.2 \tag{5.5}$$

5.4 Discussion and outlook

The hydrogen measurements indicate the presence of a hydrogen contamination in XENONnT. The actual contamination of the LXe can not be measured because it lies below the blank level of the APIX dQ. The limiting factor of the detection threshold is the presence of a non-zero blank (shown in section 5.2.1). Eliminating this blank would lower the detection threshold by a factor ~ 50, which would improve the measurement of $\alpha_{H_2}^{Xe}$ and possibly allow a direct hydrogen measurement in LXe.

As stainless steel is the most abundant material for constructing the XENONnT gas system, it is also the main source of hydrogen contamination through outgassing. From equation 5.1, we know that the driving factors for hydrogen amount are the surface of the stainless steel to which xenon is exposed and how long xenon is exposed to it. The concentration depends also on the amount of xenon: the more xenon, the more diluted the hydrogen is. One would expect that the source contributing the most are then the pipes of the gas systems and the packaging material of the radon column.

Performing an accurate calculation of the hydrogen sources is beyond the scope of this work, as it requires a precise calculation of the xenon flow in the subsystems, and

the calculation of the hydrogen outgassing rates below room temperatures in the case of the cryostat. The final hydrogen contamination is the result of the dynamic equilibrium between the constant outgassing from the stainless steel and the constant removal of the getters.

It is possible to give a conservative estimate of the hydrogen concentration in LXe using $\alpha^{\mathrm{Xe}}_{\mathrm{O_2}}$. As hydrogen is lighter than oxygen (see table 2.1), we expect $\alpha^{\mathrm{Xe}}_{\mathrm{H_2}} > \alpha^{\mathrm{Xe}}_{\mathrm{O_2}}$. This estimate makes sense if the dynamic equilibrium of oxygen and hydrogen is similar, so if the oxygen and hydrogen contamination and purification are behaving in a similar way. From the purification side, according to the specifications, the getter material should remove in a similar way both oxygen and hydrogen. A similar conclusion can be reached for the liquid purification system, meaning that oxygen and hydrogen are compatible from the removal point of view. From the contamination side, we assume that the sources of oxygen and hydrogen are equally distributed. This is a reasonable assumption as both of them are derived from outgassing, but no dedicated measurement was performed so far.

With the assumptions listed above and using the values in equation 4.1, we can calculate a hydrogen concentration in LXe of:

$$C^{\mathrm{LXe}}_{\mathrm{H_2}} < \frac{C^{\mathrm{GXe}}_{\mathrm{H_2}}}{\alpha^{\mathrm{Xe}}_{\mathrm{O_2}}} = 0.2 - 2.0 \text{ ppb} \tag{5.6}$$

In XENON1T the estimated hydrogen contamination was 30 ppb. A direct comparison of the measurement in this work with XENON1T is not possible due to the enlarged inventory, the new liquid purification and radon column systems, and the several purification procedures done for the commissioning of XENONnT. However, if the measured concentration is confirmed, it means that the tritium background in XENONnT is sub-dominant.

Chapter 6

Radon daughters deposition

In chapter 2 it is described how PTFE is used in dual phase xenon TPCs as a light reflector and insulator. In XENON1T the PTFE is screened [91], its top layer is removed using diamond tools to improve the reflectivity and it is cleaned with nitric acid [41]. A similar procedure was used for the PTFE in XENONnT. Since it is not possible to clean all the TPC components at the same time, the PTFE was stored in a cleanroom environment during the cleaning and assembly operation.

As it is crucial to avoid contamination of ^{222}Rn chain for a clean background (see chapter 2), it is necessary to make sure that the storage of the TPC components is safe. This chapter presents a study to quantify the deposition of ^{210}Po and ^{210}Pb during the storage phase using an alpha detector. ^{210}Pb itself decays emitting a β particle, but we can use the subsequent measurement of the ^{210}Po decay to also monitor ^{210}Pb. For the ^{222}Rn decay chain, see figure 6.1.

The alpha detector and its setup are described in section 6.2. Section 6.3 describes the phenomenom of polonium vacuum evaporation and how it impacts the background of the setup. Section 6.4 discusses a method to identify surface and bulk events. Finally section 6.5 presents the results from the campaign measurement during XENONnT commissioning and section 6.6 gives an outlook on the future of these measurements.

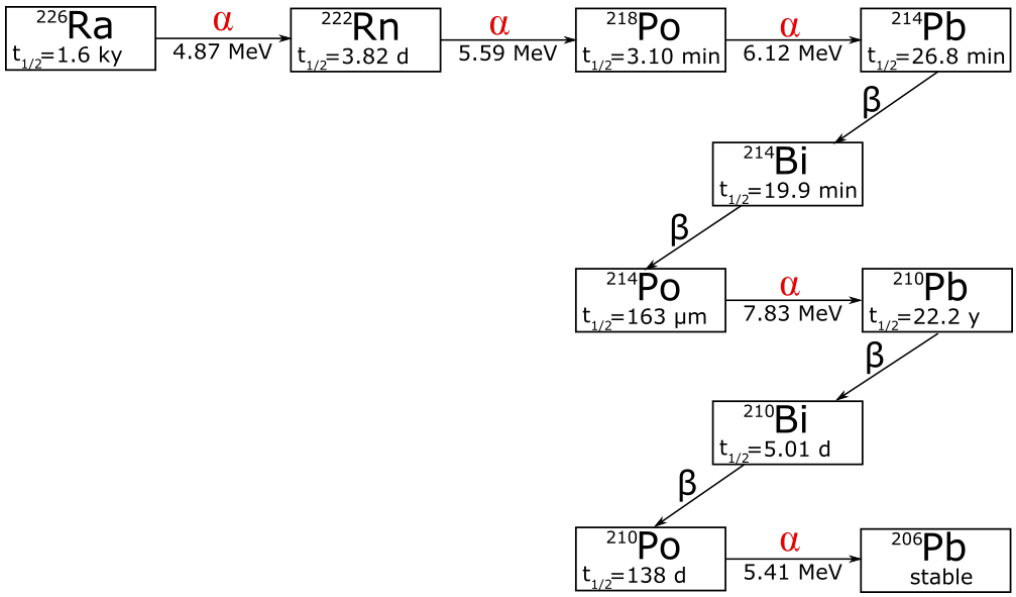

Figure 6.1.: Decay chain of ^{222}Rn starting from the radium mother isotope. This chain is part of the uranium-238 series. Data provided from [92].

6.1 Radon measurement with alpha detection

To detect radon and its decays product, we make use of an alpha detector. The detector used in this work is a PIN diode. A PIN diode is formed by a semiconductor with an extensive intrinsic region in the center (I), and a P-doped and a N-doped region at the opposite sides. The diode is backwards-biased so that the central region is charge depleted. When an alpha particle stops in the intrinsic layer it generates a transient photo current that generates a pulse[93]. The pulse can be amplified and detected with a multi channel analyzer.

The surface of such a detector is between $\mathcal{O}(10 - 1000\text{mm}^2)$. For many application, the sample (solid or gaseous) is placed many centimiters away from the sample. As each alpha particle is generated with a random direction, it is possible that the probability that it reaches the detector (the "geometrical efficiency") is below the percent level. As a way to boost the efficiency, one can exploit the fact that, when a nucleus emits an alpha particle, the daughter nucleus has a probability to be positively ionized up to 60%, depending on the gas where the decay happens[94]. It is then possible to apply a negative high voltage to the front window of the diode in order to attract the positively charged ions and boost the sensitivity. As the ionization is caused by the alpha emission, it is not possible to attract the first decay of the chain (usually ^{222}Rn for the measurements that we perform).

6.2 Experimental setup

As alpha-detector, we use an Ion-Implanted-Silicon PIN diode (model CU-060-1000-100) from Ortec. It uses an implanted Boron-N-type which is extremely thin (500Å) for minimal energy loss of the incoming alpha particle [95]. It has an active surface of 3019 mm^2 and

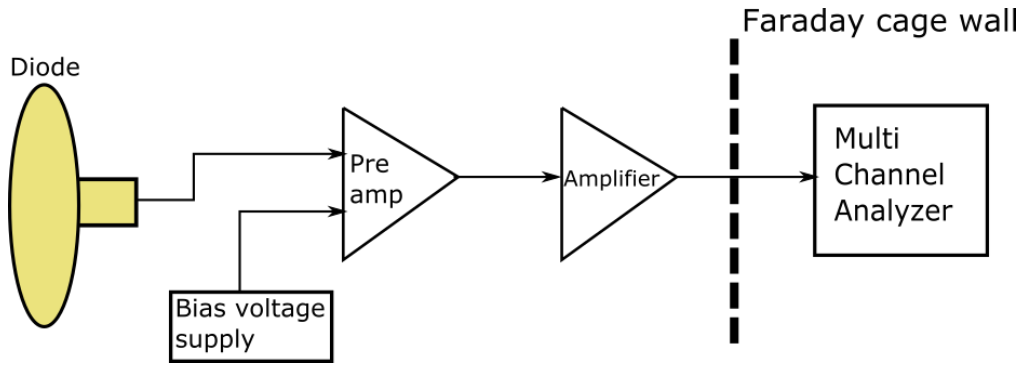

Figure 6.2.: Electronic setup of the Ortec PIN diode.

it is sold with a guaranteed background of < 24 counts per day in the $3 - 8$ MeV energy region [96]. To avoid external contamination and preserve the low-level background, the PIN diode is operated only in a cleanroom environment. The PIN diode has a BNC connector and it requires a positive bias voltage of 50 Volts (applied on the N-doped side) to be operated, which is applied through the pre-amplifier. An amplifier with gain $\times 50$ and a multichannel analyzer is used as a read-out. See figure 6.2 for the electronic setup.

As samples we use PTFE disks with a diameter of 50 mm. 8 samples have been measured in total. Before placing them for the radon exposure, they have all been cleaned at the same time in the same manner: ultrasonic bath with Elma 65 soap[1] at 3%, rinsed twice with de-ionized water and dried with clean N_2. Two of those samples were measured just after the cleaning procedure. The others were placed in couples and located:

1. in the XENONnT water tank (one horizontal, one vertical);
2. in the underground cleanroom;
3. inside a box as a storage blank.

The samples were exposed for 131 days (only on one side), during which great care was taken in not touching the exposed surface and disrupt the deposition. After the exposure, they were stored in radon-tight bags, taking care that the exposed surface was not touching the bag.

The samples are placed with the exposed side facing the PIN diode (see figure 6.3 for a sketch). The alpha particles are generated on the surface or in the bulk by ^{210}Po decays (which are themselves the decay product of ^{210}Pb). If they are generated with the right angle, they reach the PIN diode and will be detected if they have sufficient energy.

The measurements are carried out inside a cylindrical vacuum vessel which was constructed for [97], with the addition of a holder that was manufactured for the Ortec PIN diode. The diode is mounted on the top flange (where also a BNC feedthrough is located) facing down to the sample which is placed on a platform. The distance between the diode and the sample is fixed at $d = 8 \pm 2$ mm for this study, but it could be in principle changed. The whole structure and electronics are placed in a Faraday cage to reduce external noise.

[1] https://www.elma-ultrasonic.com/fileadmin/downloads/CleaningAgents/ProductInformation/EN/PI_elma%20clean%2065%20(EC%2065)_EN.pdf

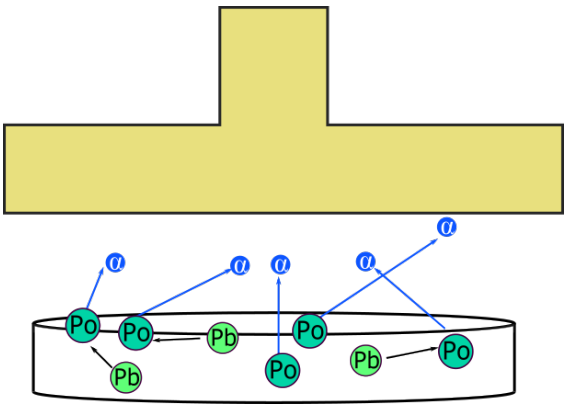

Figure 6.3.: Sketch of the alpha detection process. If the alpha particles (blue) are generated with the right angle they hit the PIN diode (gold)

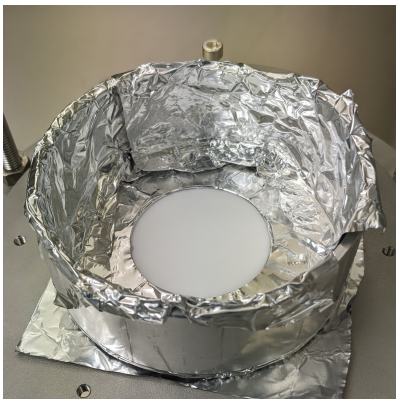

Figure 6.4.: Picture of a PTFE sample (white) surrounded by the aluminum-covered shield.

The measurements are performed in vacuum, with pressure < 1 mbar. At this pressure, the mean free path of alpha particles of 5 MeV energy is > 50 cm(simulated with SRIM, see [98]. Since it is much bigger than the distance between the sample and the PIN diode in our setup, we can assume that the alpha particles arrive at the diode without loosing energy.

At the same time, the metal structure that holds the sample and the vessel itself is also closer to the PIN diode than 50 cm, which means that extra shielding is needed to reduce background events. The shield is composed of two aluminum pieces (visible in figure 6.4):

1. to stop the contamination from the surface where the sample is sitting, we use a disk with a hole, that has the a diameter slightly smaller than the diameter of the sample disks. This also ensures that the measured surface is always the same, even if the PTFE disks themselves have slightly different diameters.

2. to stop the contamination from the rest of the cylinder, a hollow cylinder encase both the sample and the diode

6.2.1 Geometrical efficiency

Although the PIN diode has a 100% efficiency[96], not all the alpha particles generated by the ^{210}Po decays hit the detector: they need to have the right combination of position and momentum direction in order to reach the diode. Figure 6.6 illustrates the geometry of a decay.

We assume that the alpha particles are homogeneously distributed on the surface of the sample and their direction is isotropically distributed. The starting position of a particles is denoted by (x_0, y_0) couple, with the condition that $x_0^2 + y_0^2 \leq R_S$ and R_S being the radius of the sample (in this case, the radius of the hole of the holder ring). The unit vector of the particle momentum is characterized by the two angles (θ, ϕ). Since momenta are uniform in spherical coordinates, we have the conditions $\phi \in [0, 2\pi]$ and $\cos(\theta) \in [0, 1]$.

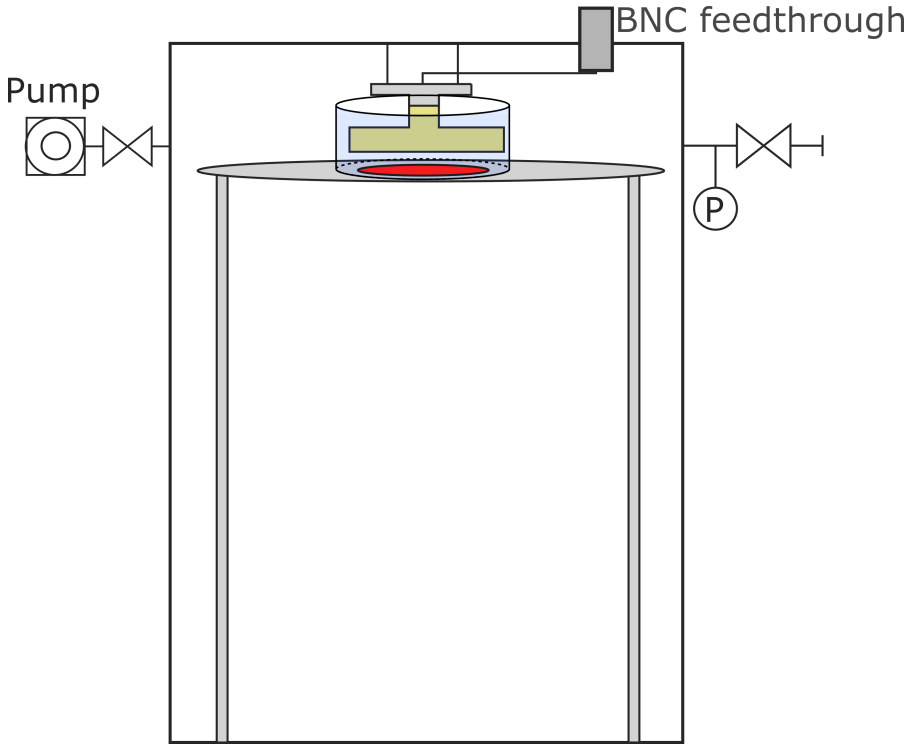

Figure 6.5.: Schematic of the big vacuum vessel. The diode is in gold, the sample is red and the shields are in light blue.

A hit occurs when the final particle coordinates (x_1, y_1) are inside the diode active area, namely $x_1^2 + y_1^2 \leq R_D$ with R_D the radius of the diode. (x_1, y_1) can be calculated via:

$$\begin{aligned} x_1 &= x_0 + d\tan(\theta)\cos(\phi) \\ y_1 &= y_0 + d\tan(\theta)\sin(\phi) \end{aligned} \tag{6.1}$$

To calculate the geometrical efficiency, a Monte Carlo simulation is performed (see figure 6.7). $N = 10^7$ alpha particles are generated with random (x_0, y_0) and (θ, ϕ). The error from the Monte Carlo simulation is negligible. If a particle's final position (x_1, y_1) satisfies the hit condition, a hit is recorded. The geometrical efficiency η is calculated:

$$\eta = \frac{N_{hit}}{N} \tag{6.2}$$

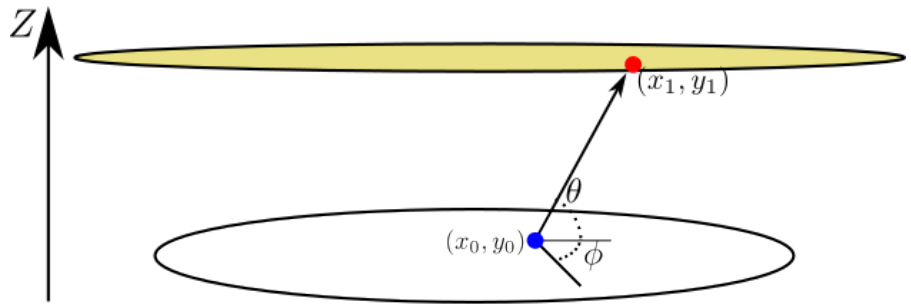

Figure 6.6.: Geometry sketch of a alpha particle trajectory, from where it is generated (blue dot) to where it hits the detector (red dot).

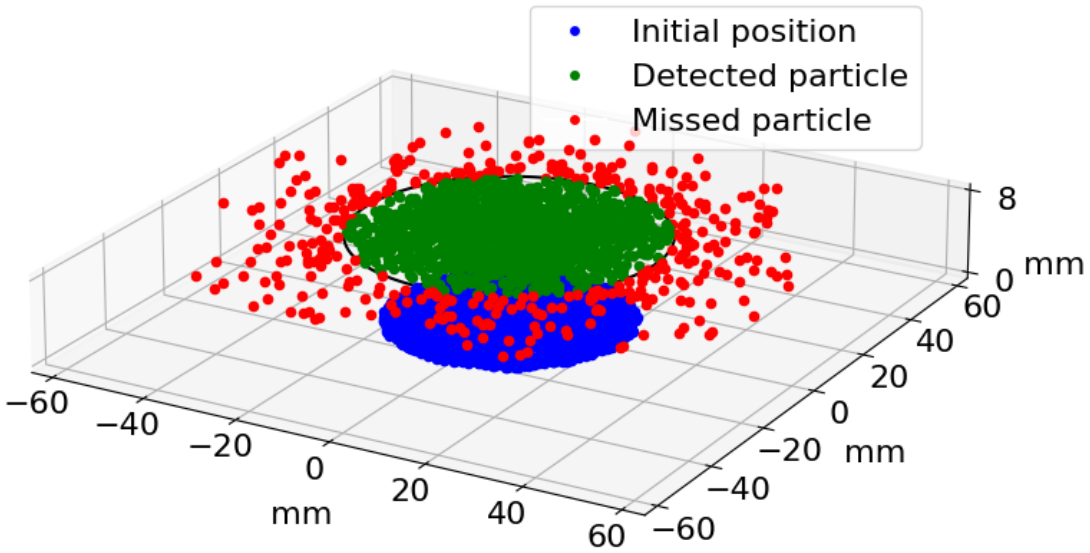

Figure 6.7.: Monte Carlo simulation of the geometrical efficiency. The sample lies at the bottom, and each simulated decay is a blue dot. The PIN diode is at the top. Hits are red and misses are green.

Since both the sample and the PIN diode have a similar size, the driving factor of the uncertainty comes from the distance d between the diode and the sample. Figure 6.8 shows the how changing the distance in the simulation changes the resulting geometrical efficiency.

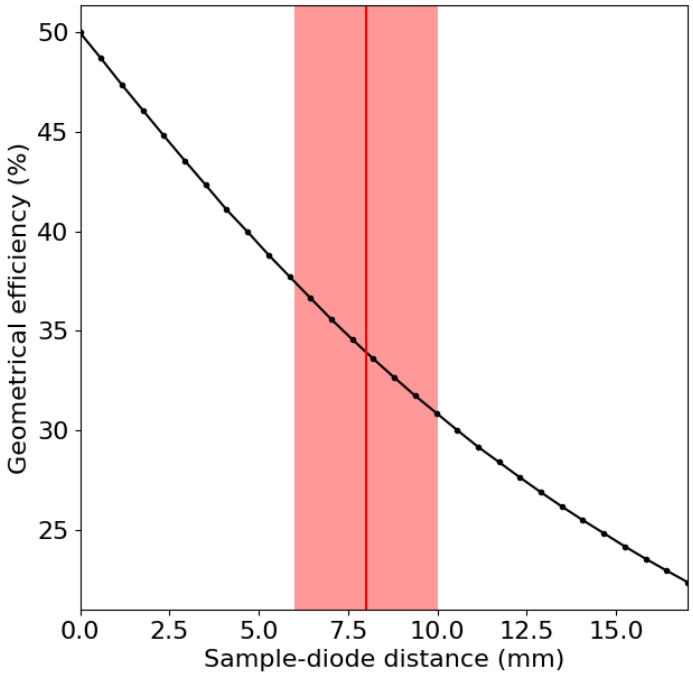

Figure 6.8.: Geometrical efficiency as a function of the distance between the sample and the PIN diode (d). The distance used distance in this work and its uncertainty is marked in red ($d = 8 \pm 2$ mm).

At the limit where $d = 0$, the geometrical efficiency is 50% since half of the alpha particles are emitted downwards and have no chance of being detected. At the opposite limit $d \to \infty$ the solid angle covered by the diode tends to 0, thus also the geometrical efficiency goes to 0. For the best geometrical efficiency, d needs to be small as possible, as allowed by the PIN diode operations. In the current setup with $d = 8 \pm 2$, the resulting a geometrical efficiency is:

$$\eta = 0.34^{+0.04}_{-0.03} \tag{6.3}$$

6.2.2 Energy calibration

From similar smaller PIN diodes [97], we expect the energy calibration to be linear with respect to the read-out energy channel. To confirm this, we calibrated the diode with an ion beam implanted ^{226}Ra source which production is described in [99]. For more information, see [100].

This source produces alpha particles with 4 different decays: from ^{226}Ra, ^{222}Rn, ^{218}Po and ^{214}Po (see figure 6.1). The last alpha decay from the chain from ^{210}Po is not visible since the source was produced 3 years before this calibration. As a consequence, ^{210}Po is yet not in equilibrium with the predecessor nuclei due to the ~ 22 years half-life of ^{210}Pb. The source was measured at the same distance and vacuum pressure as the samples. Its

spectrum is shown in figure 6.9. The data is binned in energy channels and it is fitted with a function that is the sum of 4 normal distrubution, one for each alpha line. The parameters of the fit (height, mean and width of each gaussians) are left free and their fitted values are listed in table 6.1.

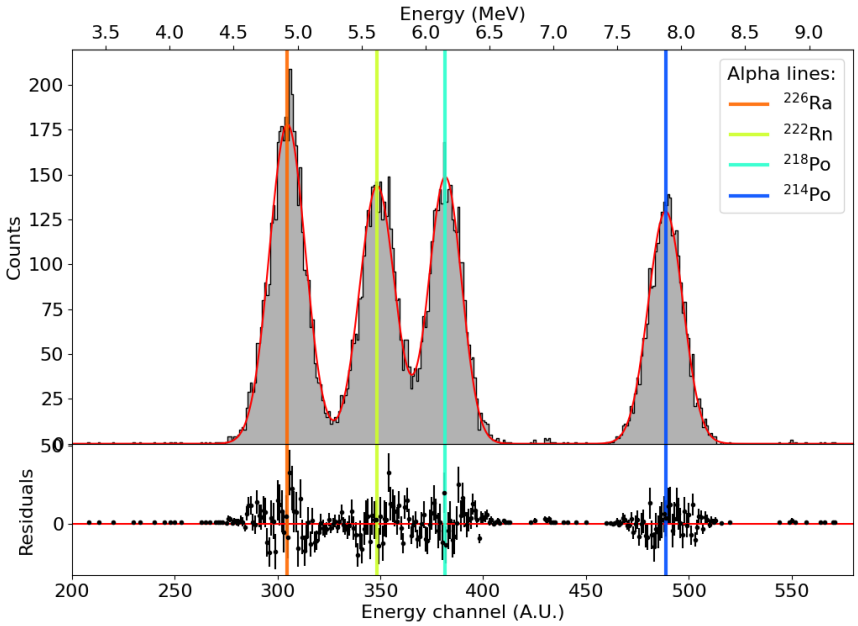

Figure 6.9.: Spectrum of the alpha particles produced by the ^{226}Ra source.

Table 6.1.: Fit parameters for the 4 gaussians fit from figure 6.9

Isotope	Mean	Standard deviation
^{226}Ra	304.8 ± 0.2	8.7 ± 0.1
^{222}Rn	348.4 ± 0.2	8.5 ± 0.2
^{218}Po	381.6 ± 0.2	7.9 ± 0.1
^{214}Po	488.8 ± 0.2	8.4 ± 0.1

From the calibration, it is possible to calculate the energy resolution of the PIN diode. We take conservatively the worst possible width, from the ^{226}Ra peak, and, dividing by the energy of ^{210}Po, we calculate that the energy resolution is $2.56 \pm 0.03\%$. Figure 6.10 shows the linearity of the fitted means compared with the literature values of the energy of the alpha particles in our region of interest. In addition, the energy calibration has no offset: this means that it is sufficient to fit one peak to calibrate the whole range.

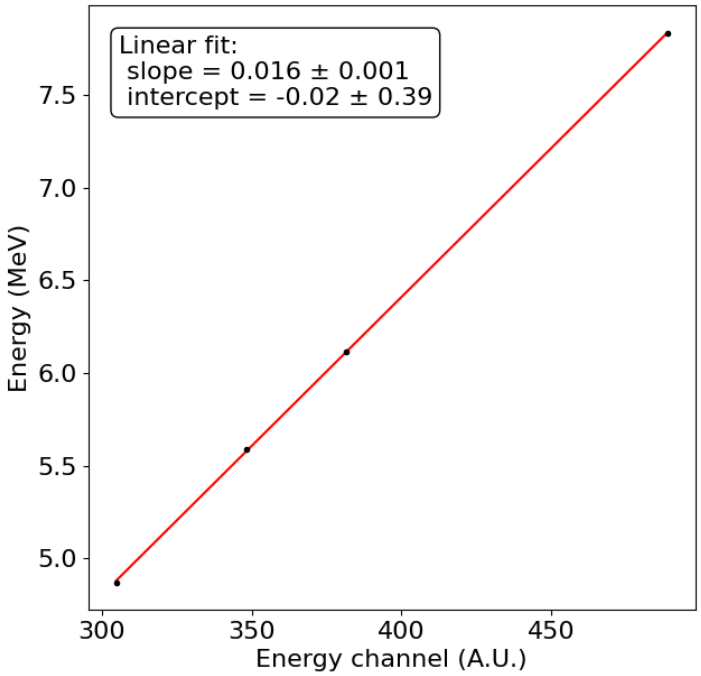

Figure 6.10.: Alpha particle energy vs energy channel from the gaussian fit (from table 6.1). The best fit for the energy is linear and it is compatible with no offset.

6.2.3 Noise reduction

Low-energy noise At low energies (< 3 MeV) a tail of events is constantly present. This noise has a decaying exponential shape with respect to the energy channels and it is not problematic since it is well separated from the energy range taken into consideration in this work (> 4.5 MeV).

Timed-noise The data is recorded in time bins of 1 minute. In some bins there is a high amount of hits that does not reflect the usual hit distribution per time bin. To evaluate the hit distribution, an energy region is defined where the contribution from both the low energy noise and the lower alpha peak are negligible. Figure 6.11 shows the hit time distribution for one measurement in this region. A threshold is defined based on the cumulative hit distribution of all data sets and it is placed at 3 events per time bin. The threshold value was chosen so that it cuts between 1 and 4% of data, depending on the dataset, which will be also a correction of the live-time. This cut is not applied for calibration data: in that case the high activity of the calibration source generates more events per minute and an updated threshold is based hit time distribution specifically for the calibration data sets. Figure 6.12 shows an example of events that are cut, and it is possible to see that most of the events in the ^{210}Po interval are not removed.

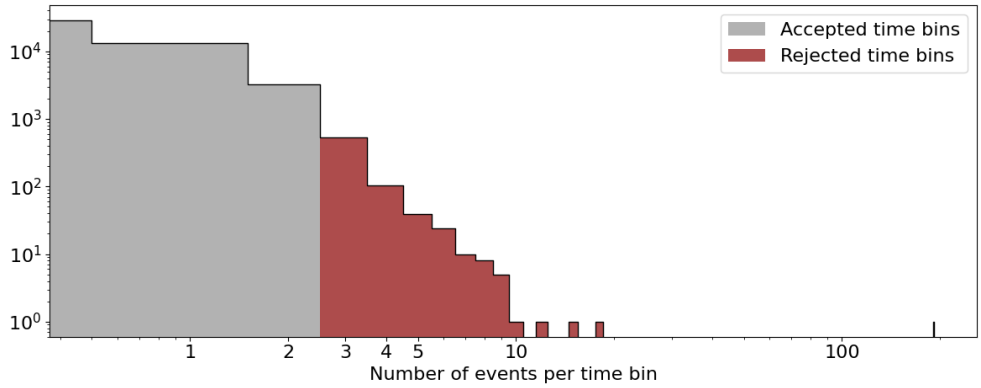

Figure 6.11.: Example of hit distribution per time bin (in double log-scale) in the energy region between the low-energy noise and the lowest of the alpha peak for one measurement. All the time bins in red are equal or above the 3 events threshold and are rejected.

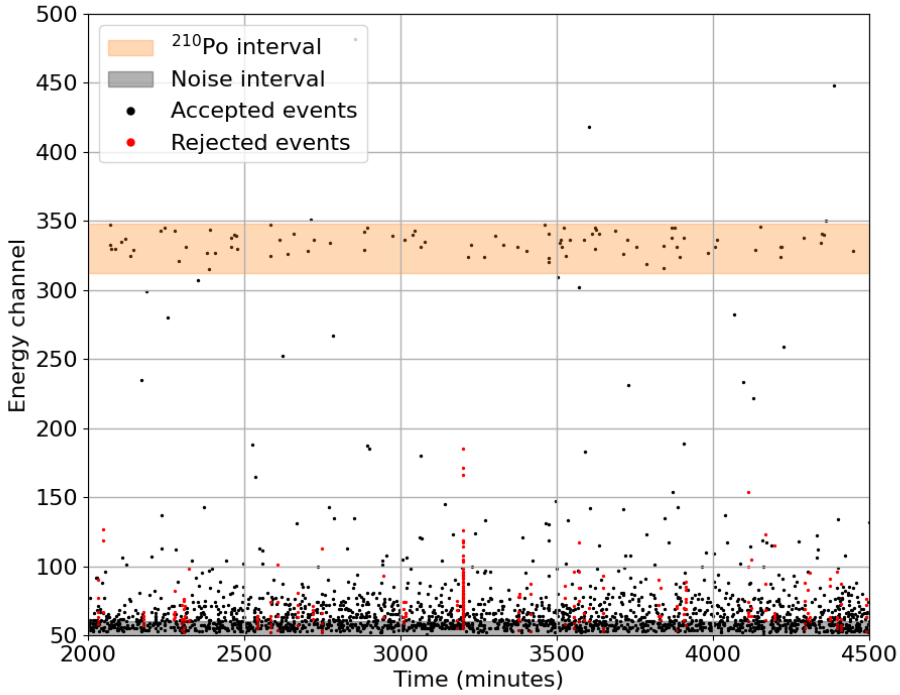

Figure 6.12.: Example of events rejected by the timed noise cut.

6.3 Polonium evaporation

As we are interested in measuring ^{210}Po, the very first calibration of the PIN diode was performed using a strong ^{210}Po source. This source consists of a PTFE disk that was exposed to ^{222}Rn enriched air, which resulted in ^{210}Po to be loaded onto the PTFE disk. For more information see [53]. Since the exposure was done several years prior this work, all the fast components have decayed, which leaves only ^{210}Pb with its 22.3 years of half life and its daughters, which slowly grow-in. ^{210}Pb is considered to be at equilibrium with its daughters, ^{210}Bi and ^{210}Po. Of these decays, the only one that produces an alpha line is ^{210}Po, while ^{210}Pb and ^{210}Bi are beta emitters.

After the ^{210}Po calibration, we observed an increase of the diode background in the ^{210}Po energy region. A spectrum comparison is given in figure 6.13 and table 6.2 has the counts in this region, but a quantitative calculation is not possible, since part of the shielding was missing in the blank before the calibration. Therefore, the numbers of events in the blank after the calibration in table 6.2 underestimate the increase of the activity of the PIN diode after the calibration. Nontheless, it is possible to see qualitatively how the blank after the calibration has increased compared to the blank before.

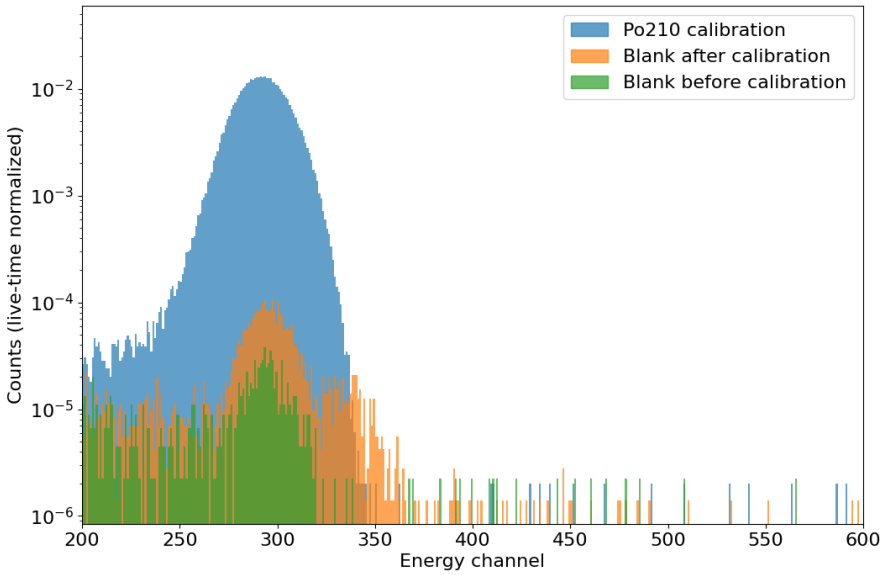

Figure 6.13.: Alpha spectra before, during and after the ^{210}Po calibration.

The cause of the increased activity is due to the evaporation of ^{210}Po from the PTFE source and its deposition on the window of the PIN diode. Polonium is a metal with a melting and boiling point of 527 K and 1235 K respectively, and a vapour pressure that is zero at room temperature [101]. However, there are indications that polonium is more volatile than expected [102] and some early measurements show an enhanced volatility in vacuum even at room temperature [103].

This phenomenon was also observed using another detector in [97]. There, the activity

Table 6.2.: Activity in the ^{210}Po energy region before, after or during the calibration

	Activity (events/day)
Blank before calibration	68 ± 4
^{210}Po calibration	$36,580 \pm 80$
Blank after calibration	268 ± 5

of a ^{210}Po loaded PTFE disk was measured over time. It was observed that the activity of the disk is decreasing faster than what one would expect naively from the simple radioactive decay. Moreover, the accelerated loss of activity is present only when the disk is in vacuum.

Due to this volatility, the shields described in 6.2 are covered with new aluminum foil every time a new measurement is started, to prevent the ^{210}Po from any contaminated sample to attach to the shield. It is not possible to prevent this for the diode itself, but the very high activity of the initial ^{210}Po calibration dominates the added activity from any sample.

6.3.1 ^{210}Po background estimation

The first step in estimating the background is to develop a way to measure the activity that is coming *only* from the diode ("diode background"). Alpha particles have a high energy deposition in a medium, so to shield from external activity a protection gas must be employed.

In this case, the protection gas is the air (of the cleanroom). A SRIM simulation indicates that the range of alpha particles with energy 5.41 MeV (the ^{210}Po decay energy) is 40 mm in air. However, the alpha particles lose energy while travelling in air, so the effective measurable range is lower: for our analysis we define a Region of Interest (ROI) within 2σ of the mean of a peak (see 6.4), so we have to calculate the maximum distance for which the alpha particles would still fall inside the ROI. From 6.2.2, it was calculated that the width of 2σ is $\sim 5\%$, so if an alpha particle loses more than 5% of its energy, it will fall out of the ROI. The energy loss is also simulated with SRIM and shown in figure 6.14, and it is possible to see that only particles within 3 mm from the diode have enough energy to fall in the ROI.

Thus to performe a diode background measurement it is sufficient to remove the inner metal support structure, so that the closest metal surface to the PIN diode is > 150 cm, and not to evacuate the chamber. The spectrum of such a measurement is shown in figure 6.15.

There are three peaks in the spectrum: one is the expected ^{210}Po contamination, there are two other isotopes of polonium: ^{214}Po and ^{218}Po (compare also to the spectrum of figure 6.9). Those isotopes are short lived, and decaying over time, compatible with an injection of ^{222}Rn at the start of the measurement. The ^{222}Rn concentration in air was measured at $A_0^{\mathrm{Rn}} = 10 \pm 1$ Bq/m^3([2]), which confirms the fact that some radon is present

[2]Measured for one week with a handheld radon monitor (https://cdn2.hubspot.net/hubfs/4406702/Website/Product%20Sheets/Home/Home%20Product%20Sheet.pdf)

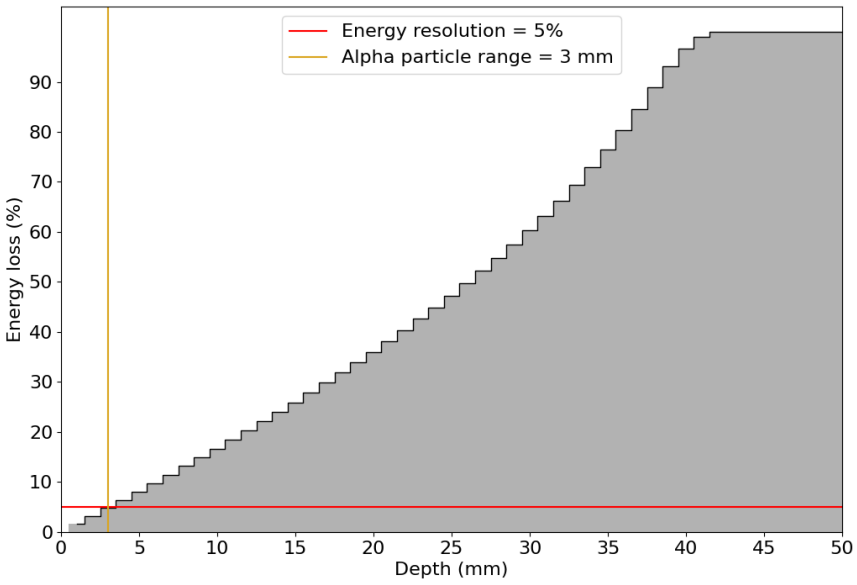

Figure 6.14.: Simulation of energy loss of alpha particle in air. The maximum radius corresponding to a particle reaching the diode in the region of interest is only 3 mm.

in the cleanroom air at the start of a measurement.

We can calculate how many events we expect to measure from a ^{222}Rn injection. ^{222}Rn decays with half-life of 3.8 days and emits alpha that has energy 5.59 MeV, which is not possible to resolve from ^{210}Po. We can then estimate the contribution to the ^{210}Po peak based on the initial activity and the probability that an alpha particle from a ^{222}Rn hits the detector.

The first step is to construct a volume around the diode where the alpha particles are generated close enough so that they are able to reach the detector in the right energy range, provided that they have the right momentum direction. As simulated before, the maximum distance at which an alpha particle will not loose enough energy for falling in the ^{210}Po region is $l = 3$ mm. The volume is composed of a cylinder part with height l and radius the radius of the PIN diode (R_D), and a quarter of torus with distance from the center P and radius of the tube l (see figure 6.16). The total volume is:

$$V = V_{cyl} + \frac{V_{tor}}{4} = \pi l R_D^2 + \frac{\pi^2}{2} R_D l^2 = 10.43 \pm 0.06\,\mathrm{cm}^3 \tag{6.4}$$

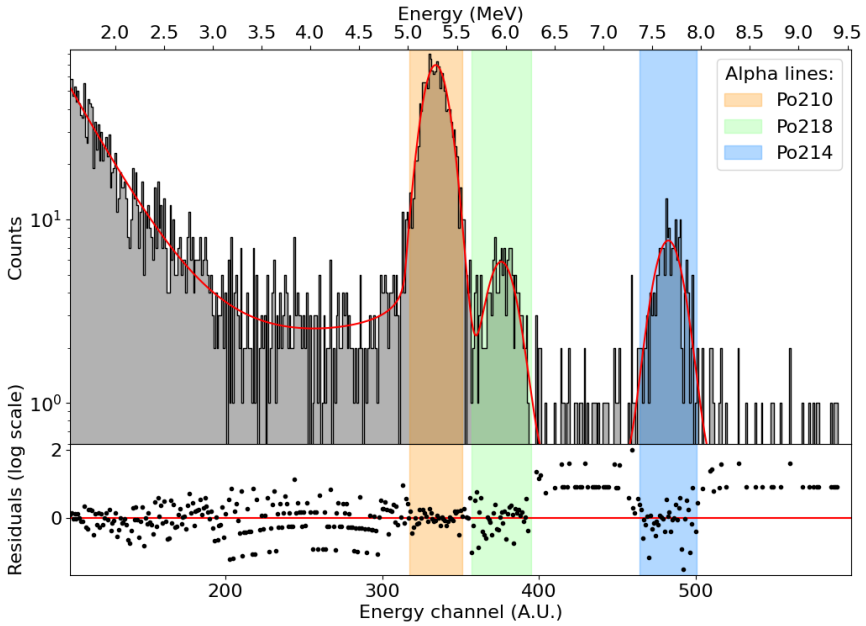

Figure 6.15.: Alpha spectrum of a "diode only" measurement with air from the cleanroom.

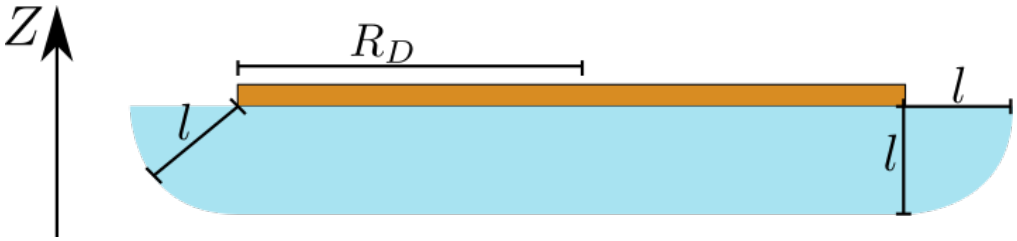

Figure 6.16.: Cross section (not to scale) of the air volume that the alpha particles are able to traverse. The PIN diode is in orange and the volume in light blue.

We can then simulate the probability that an alpha particle generated at a random position in this volume with a random momentum has to hit the detector. The simulation was done in a similar way as the one for the geometrical efficiency simulation, with $N = 10^7$ alpha particles. The resulting efficiency is $\eta_V = 36\%$.

In total, the amount of alpha particles that we expect to contribute in a measurement that lasts a time T is:

$$N_{\mathrm{Rn}} = \eta_V V A_0^{\mathrm{Rn}} \int_0^T \exp(-\lambda^{\mathrm{Rn}} t) dt = \frac{\eta_V V A_0^{\mathrm{Rn}}}{\lambda^{\mathrm{Rn}}} (1 - \exp(-\lambda^{\mathrm{Rn}} T)) \tag{6.5}$$

For a typical measurement of one week, N_{Rn} is less than one event, so we can neglect the radon contamination in the ^{210}Po ROI. We do expect to have some contribution of alpha particles that lose their energy at lower energy compared to the ^{210}Po ROI, which is indeed what we observe in 6.15. To model this tail, instead of a normal distribution,

this peak is fit using a Crystall Ball function. More details on this function are given in section 6.4. In the cases where a diode background measurement runs for longer times and it is possible to cut the first 9 days of data ($\sim$ 3 times the half-life of ^{222}Rn) the tail is negligible and a normal distribution fit can be used.

A similar calculations can be done for the other alpha decays of the chain, ^{214}Po and ^{218}Po, and it yields a similar result, with the number of expected measured events $<$ 1 event/day. This is in contrast with the three peaks saw in 6.15. We can explain the detection of the alpha particles generated by the ^{214}Po and ^{218}Po decays with an additional charged ions collection effect, as introduced in section 6.1. This hypothesis is also supported by the fact that the peaks have a normal shape: this means that the alpha particles do not lose any energy in air, thus the decay itself takes place at the PIN diode window. However, the PIN diode is only biased with positive voltage, so no collection of positive ions can take place. The study of this phenomenon is beyond the scope of this work, but we can make two hypotheses: either the ions detected are negatively charged, or the field line generated by the PIN diode bias voltage have a non-trivial shape, guiding more positively charged ions than naively expected. In either case, this phenomenon it does not impact the measurements itself: ^{222}Rn is neutral thus does not have any collection process, and the ^{214}Po and ^{218}Po are separated with respect to ^{210}Po for more than 2σ, so no contamination is present due to these alpha lines. As for the tail of ^{222}Rn, cutting the first 9 days of a measurement also removes the ^{214}Po and ^{218}Po peaks.

6.3.2 Time evolution of ^{210}Po contamination

It is hard to quantify the initial contamination of the diode due to the fact that it happened during the early design phase of the setup, but it is possible to evaluate its evolution over time and eventually correct for it. Several measurements described in subsection 6.3.1 have been taken while measuring the samples. All the measurements are fitted separately due to a small observed energy shift (see table 6.3).

Table 6.3.: Integration limits energy channels. Some dataset are time-cut so that no ^{214}Po and ^{218}Po are present in the spectrum

^{210}Po		^{218}Po		^{214}Po	
298	343	-	-	-	-
313	350	358	391	460	498
312	348	362	398	468	504
316	352	361	393	465	501
299	336	-	-	-	-

The data from those measurements is binned in days and shown in figure 6.17. It is possible to fit a exponential decay. The fitted half-life is compatible with the one from literature of ^{210}Po (138 days). The exponential fit is used to predict the amount of events coming from the diode contamination (N_{cont}). For a measurement that is done from the time t_1 to the time t_2:

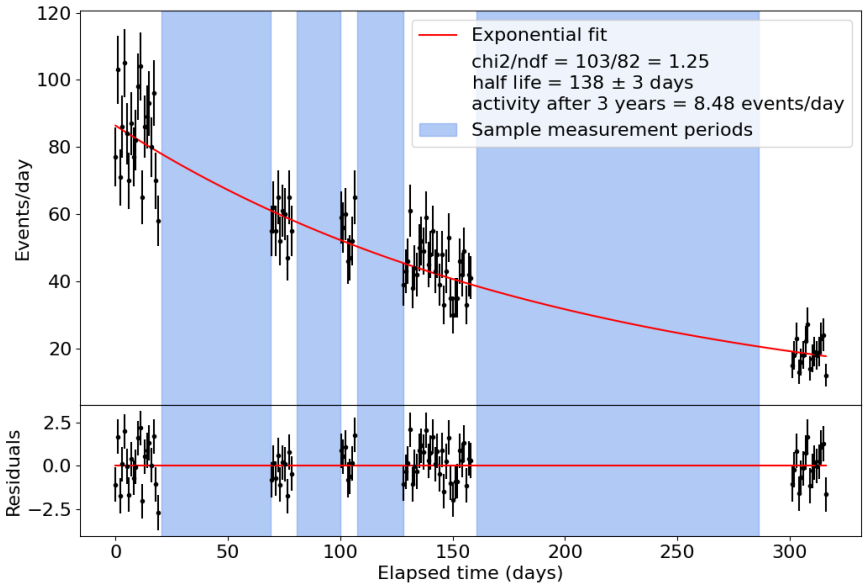

Figure 6.17.: Fit of the time evolution of the ^{210}Po contamination (starting after the ^{226}Ra calibration). The shaded regions are the times where the samples are measured.

$$N_{cont} = \int_{t_1}^{t_2} I \exp(-\lambda t) dt = -\frac{I}{\lambda}(\exp(-\lambda t_1) - \exp(-\lambda t_2)) \tag{6.6}$$

Where I is the initial contamination and $\lambda = \ln(2)/t_{1/2}$ the decay constant. The variances and covariance of I and λ are calculated from the fit, and the variance of N_{cont} is:

$$\begin{aligned}
\sigma^2_{N_{cont}} &= \left|\frac{\partial N_{cont}}{\partial I}\right|^2 \sigma_I^2 + \left|\frac{\partial N_{cont}}{\partial \lambda}\right|^2 \sigma_\lambda^2 + 2\frac{\partial N_{cont}}{\partial I}\frac{\partial N_{cont}}{\partial \lambda}\sigma_{I\lambda} \\
\frac{\partial N_{cont}}{\partial I} &= -\frac{1}{\lambda}(\exp(-\lambda t_1) - \exp(-\lambda t_2)) \\
\frac{\partial N_{cont}}{\partial \lambda} &= \frac{I}{\lambda^2}(\exp(-\lambda t_1) - \exp(-\lambda t_2)) + \frac{I}{\lambda}(t_1 \exp(-\lambda t_1) - t_2 \exp(-\lambda t_2))
\end{aligned} \tag{6.7}$$

6.4 Spectral line peak shape

The calibration described in section 6.2.2 is well fitted by a fit function composed by a gaussian for each alpha line and an exponential to model the noise at low energies. Also the ^{218}Po and the ^{214}Po peaks from the measurements in 6.3.1 are well fitted by a gaussian. However, it was found that a better fit for the alpha lines both in the 210Po calibration and for the samples is a Crystal Ball function [104]. This function is a composition of a gaussian core with a power-law tail and it is commonly used to take into account energy losses in high energy physics:

$$f(x; N, \alpha, n, \mu, \sigma) = N \cdot \begin{cases} \exp\left(-\frac{(x-\mu)^2}{2\sigma^2}\right) & \text{for } \frac{x-\mu}{\sigma} > -\alpha \\ A \cdot \left(B - \frac{(x-\mu)}{\sigma}\right)^{-n} & \text{for } \frac{x-\mu}{\sigma} \leqslant -\alpha \end{cases} \tag{6.8}$$

with.

$$A = \left(\frac{n}{|\alpha|}\right)^n \cdot \exp\left(-\frac{|\alpha|^2}{2}\right)$$
$$B = \frac{n}{|\alpha|} - |\alpha|$$

The parameters μ and σ are the mean and width of the gaussian, α is the threshold to switch to the power-law tail, and n is the power of this power-law. N is the normalization constant which depends on the number of events measured.

While for the ^{210}Po peak in section 6.3.1 it is clear that the tail comes from the energy loss of ^{222}Rn, in this case the system is in vacuum and there is no loss of the alpha while they travel from the surface to the PIN diode. We also know that there is no energy loss at the diode itself from the calibration in 6.2.2. The only remaining place where the alpha particles can loose energy is in the PTFE itself.

So far, we always assumed that the ^{210}Po decay that generates the alpha particle is on the surface of the PTFE. However, it is possible that some radioactive elements from the ^{226}Ra decay chain are trapped in the bulk of PTFE from the production. The range of alphas with energy 5.41 MeV in PTFE is 25.5 µm (simulated with SRIM), so we can expect that some of the decays that are happening inside the bulk reach the surface and are free to travel to the detector. The energy they loose inside the PTFE is then reflected in the Crystall Ball tail.

For this work, we are interested only in the surface contamination. For all the datasets, $\alpha > 2$, which means that, by defining the ROI within 2σ from the mean, we can neglect the tail contribution. By using this ROI, we lose 4.55% of the total events which are in the purely normal tails: we have then to apply a correction factor $c_{tail} = 0.9545$ to the total number of events in order to correct for this loss.

In conclusion, with this setup we can distinguish between bulk and surface events. For this work we focus on the surface contribution, but the bulk events can also be identified, provided that the low-energy noise can be well described and separated from the Crystall Ball tail.

Figure 6.18.: Comparison between gaussian (red) and Crystall Ball (orange) fits.

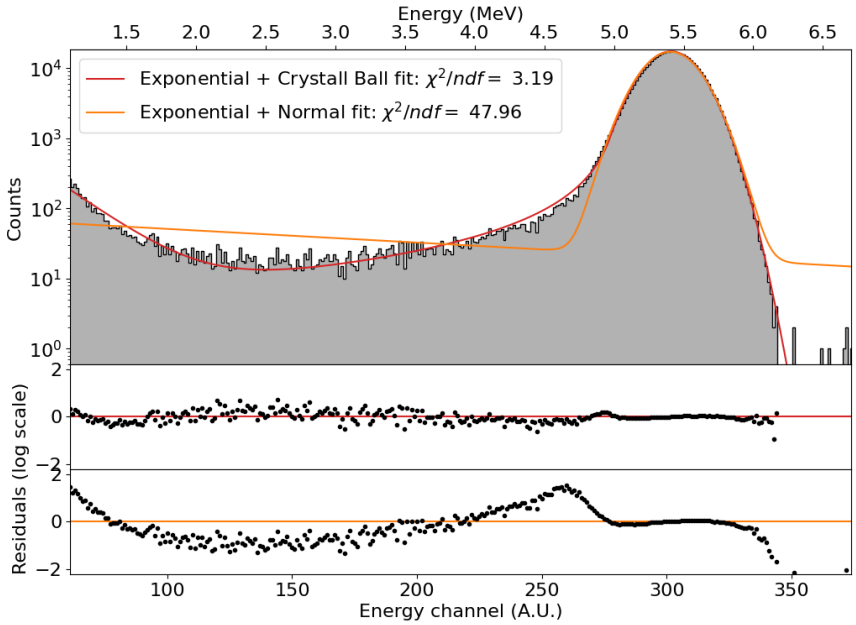

(a) ^{210}Po calibration

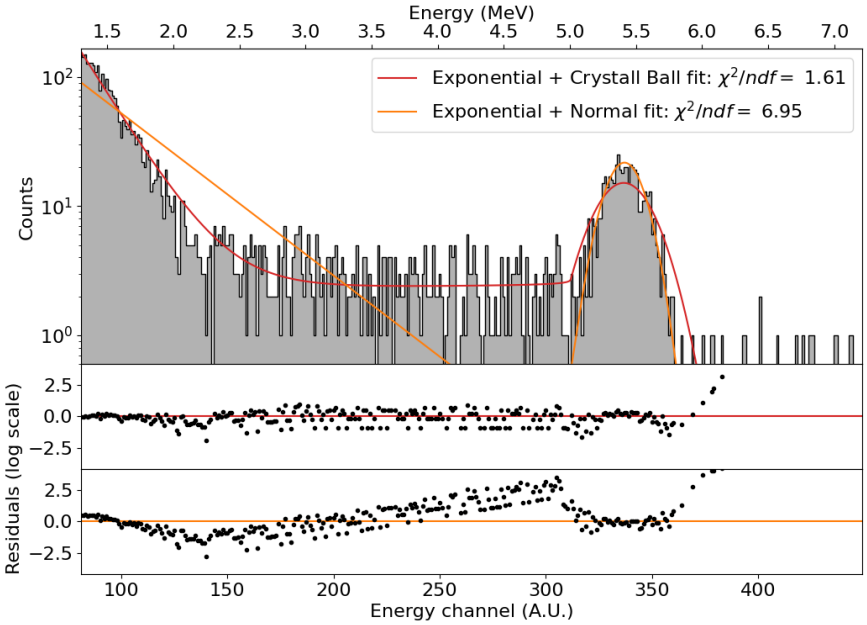

(b) Sample

6.5 Sample results

Each sample has been measured for $T \sim 1$ week and each different dataset is fitted separately since a small long term energy shift was observed. For each dataset a different ROI is defined based on the fitted μ and σ of each Crystall Ball function. We count the number of events N_{meas} that fall in the ROI in a measurement. To get the events coming only from the sample, one needs to subtract the ^{210}Po contribution from the diode itself N_{cont}. From the number of counts, we can extract the activity A in unit of time and sample surface. To do so, we have to apply two correction factors: c_{tail} for the tail losses and η for the geometrical efficiency (see equation 6.3). Finally, we want to normalize the activity for the surface of the sample $S = 18.25 \pm 0.08\,\mathrm{cm}^2$ and T. The total activity of a sample is:

$$A = \frac{N_{meas} - N_{cont}}{T \cdot c_{tail} \cdot \eta \cdot S} \tag{6.9}$$

Since N_{meas} is a simple counting experiment, $\sigma^2_{N_{meas}} = N_{meas}$ and its error is dominating over the error on N_{cont}, which is around 1 to 2%. Both S and η have a systematic uncertainty due to the fact that they are calculated based on length measurement performed with the same instrument, a caliber that has a systematic error of 0.1 mm. They are in fact anti-correlated: the smaller the distance, the smaller S but the bigger η (the sample is closer to the diode) and vice versa. The two errors are then calculated simultaneously in order to take into account this effect.

Table 6.4.: Unexposed sample disks used as blanks

Sample	T (days)	N_{meas}/T (events/day)	Average N_{cont} (events/day)	Difference (events/day)	Activity (mBq/m^2)
# 1: Side A	10.57	48 ± 2	34.8 ± 0.5	13 ± 2	250 ± 40 stat $^{+20}_{-30}$ sys
# 1: Side B	16.74	52 ± 2	32.1 ± 0.5	19 ± 2	360 ± 30 stat $^{+30}_{-40}$ sys
# 2: Side A	19.41	45 ± 2	25.0 ± 0.6	20 ± 2	370 ± 30 stat $^{+30}_{-40}$ sys
# 2: Side B	16.91	35 ± 1	21.8 ± 0.6	13 ± 2	240 ± 30 stat $^{+20}_{-30}$ sys

Table 6.5.: Exposed sample disks

Sample	T (days)	N_{meas}/T (events/day)	Average bkg (events/day)	Difference (events/day)	Activity (mBq/m^2)
MPIK Blank #1	5.78	70 ± 4	60.3 ± 0.4	10 ± 4	190 ± 70 stat $^{+20}_{-20}$ sys
MPIK Blank #2	6.75	80 ± 4	58.5 ± 0.3	22 ± 4	410 ± 70 stat $^{+40}_{-40}$ sys
MPIK Blank #2	26.33	58 ± 2	38.4 ± 0.4	20 ± 2	370 ± 30 stat $^{+30}_{-40}$ sys
Water tank (vertical)	6.70	70 ± 3	56.5 ± 0.3	14 ± 3	250 ± 60 stat $^{+20}_{-30}$ sys
Water tank (horizontal)	6.54	70 ± 3	51.7 ± 0.1	19 ± 3	350 ± 60 stat $^{+30}_{-40}$ sys
UG cleanroom #1	6.91	68 ± 3	50.82 ± 0.04	17 ± 3	320 ± 60 stat $^{+30}_{-30}$ sys
UG cleanroom #2	6.71	52 ± 3	46.53 ± 0.02	5 ± 3	100 ± 50 stat $^{+9}_{-10}$ sys

Tables 6.4 and 6.5 show the data for all the sample disks with and without exposure respectively. The unexposed samples have been measured on both sides, and it is possible to see in table 6.4 how sides A from #1 and B from #2 have similar activities and

vice-versa. This is an indication that one side of the PTFE used to manufacture the sample disks is more active than the other one. We conservatively only consider the two sides with the highest activity as unexposed blank. From these, we can construct a threshold for which we can affirm that we know with 95% confidence level that an event rate is consistent with the background ($CI_{95\%}$). Assuming that the number of measured events per day is normally distributed (since the total number of measured events > 100):

$$CI_{95\%} = \mu_B + 1.649 \cdot \sigma_B = 23\,\text{Events/day} \tag{6.10}$$

where $\mu_B = \frac{19+20}{2} = 19.5$ is the average of the two measurements and $\sigma_B = 2$ their standard deviation.

Comparing the data from tables 6.4 and 6.5, it is possible to see how all the measurements are consistent with each other. The only outlier from table 6.5 has been measured again and the second longer measurement is consistent with the background. Figure 6.20 shows a visual comparison of all the data and the threshold.

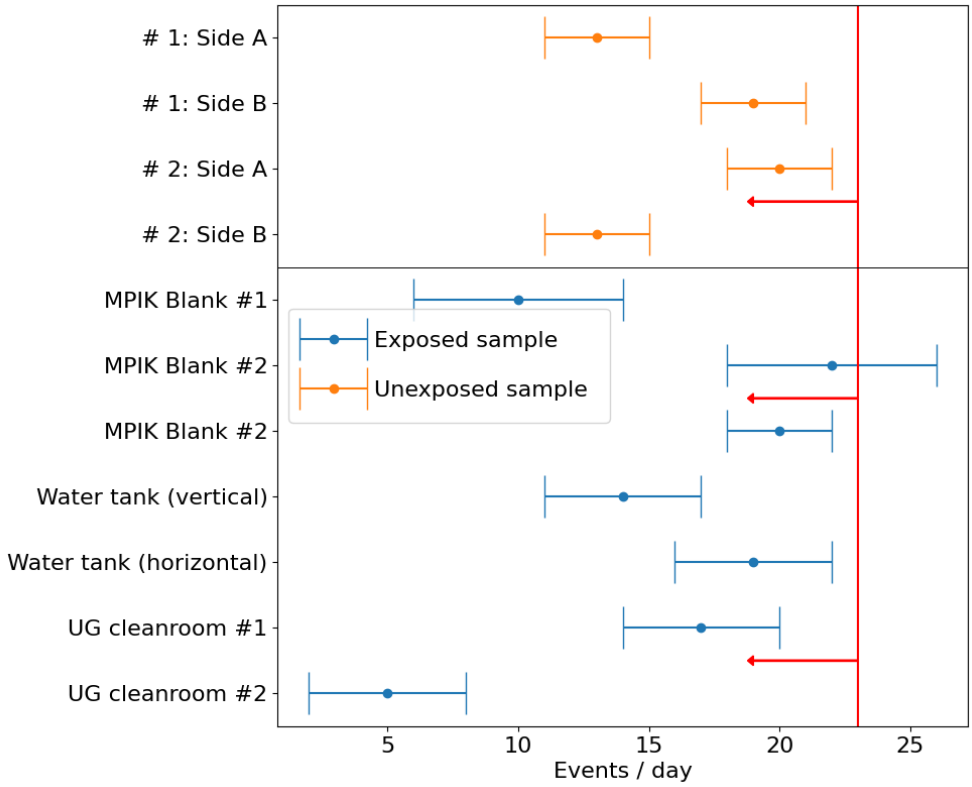

Figure 6.20.: Collection of all sample measurements, from table 6.4 (yellow) and table 6.5 (blue). The detection threshold at $CI_{95\%}$ is in red.

As written in the chapter introduction, from the ^{210}Po alpha decays we can monitor both ^{210}Po and ^{210}Pb. Since there was some time delay between the end of the exposure and the start of a measurement, we need to correct for the decay of ^{210}Po and in-grow of

^{210}Pb. We can then test the two extreme cases, one where only ^{210}Pb was deposited on the PTFE and one where only ^{210}Po was deposited, and see how the activity evolves in those two cases. The real deposited activity lies between these limits.

6.5.1 ^{210}Po deposition

^{210}Po decays with a half-life of 138 days, which is comparable with the exposure time of 131 days. We can not neglect the decay of ^{210}Po atoms that happens during the exposure phase. If we define R^{Po} the deposition rate of ^{210}Po atoms per day, we can approximate the amount of atoms deposited:

$$\begin{aligned}
\text{After 1 day} &\rightarrow R^{\mathrm{Po}} \\
\text{After 2 days} &\rightarrow R^{\mathrm{Po}} + R^{\mathrm{Po}}(\exp(-\lambda)) = R^{\mathrm{Po}}(1+\exp(-\lambda)) \\
\text{After 3 days} &\rightarrow R^{\mathrm{Po}}(1+\exp(-\lambda)+\exp(-2\lambda)) \\
&\cdots \\
\text{After } m \text{ days} &\rightarrow R^{\mathrm{Po}}(1+\exp(-\lambda)+\cdots+\exp(-\lambda(m-1))) \\
&\cdots
\end{aligned}$$

With $\lambda = \ln(2)\cdot day/t^{\mathrm{Po}}_{1/2}$. The total amount of ^{210}Po deposited after M days is:

$$A^{\mathrm{Po}}_0 = R^{\mathrm{Po}} \sum_{m=0}^{M-1} \exp(-\lambda m) \tag{6.11}$$

Once the sample is removed and the ^{210}Po collection stopped, ^{210}Po will keep decaying with an exponential. The measured activity will be:

$$A(N) = A^{\mathrm{Po}}_0 \exp(-\lambda N) \tag{6.12}$$

where N is the number of days between the removal and the measurement. Combining equation 6.11 and 6.12 we can relate the deposition rate R with the measured activity A:

$$R^{\mathrm{Po}} = \frac{A(N)}{\exp(-\lambda N)\sum_{m=0}^{M-1}\exp(-\lambda m)} \tag{6.13}$$

The results are presented in table 6.6 in the next section.

6.5.2 ^{210}Pb deposition

The half life of ^{210}Pb is 22.3 years, so we can ignore its decay during the deposition phase and assume that every day an amount of atoms R^{Pb} is deposited on the sample. For a sample exposed M days:

$$R^{\mathrm{Pb}} = \frac{A^{\mathrm{Pb}}_0}{M} \tag{6.14}$$

On the other end, there is no alpha decay from ^{210}Pb, so to monitor it we first need to wait until it decays into ^{210}Po. Ignoring any ion loss due to other effects (eg. ion recoil), and ignoring the bismuth since it has a half life of only 5 days, much shorter than lead and polonium, the lead-polonium system is described by the differential equations:

$$\begin{aligned} \frac{\mathrm{d}A^{\mathrm{Pb}}(t)}{\mathrm{d}t} &= -\lambda^{\mathrm{Pb}} A^{\mathrm{Pb}}(t) \\ \frac{\mathrm{d}A^{\mathrm{Po}}(t)}{\mathrm{d}t} &= -\lambda^{\mathrm{Po}} A^{\mathrm{Po}}(t) + \lambda^{\mathrm{Pb}} A^{\mathrm{Pb}}(t) \end{aligned} \tag{6.15}$$

The general solution of this system of differential equation for many nuclides was calculated by Bateman in [105]. In this particular case with only two decays and $A_0^{\mathrm{Po}} = 0$ as initial condition (no initial deposition of polonium) the solutions are:

$$A^{\mathrm{Pb}}(t) = A_0^{\mathrm{Pb}} \exp(-\lambda^{\mathrm{Pb}} t) \tag{6.16a}$$

$$A^{\mathrm{Po}}(t) = A_0^{\mathrm{Po}} \frac{\lambda^{\mathrm{Pb}}}{\lambda^{\mathrm{Po}} - \lambda^{\mathrm{Pb}}} [\exp(-\lambda^{\mathrm{Pb}} t) - \exp(-\lambda^{\mathrm{Po}} t)] \tag{6.16b}$$

Combining equations 6.14 and 6.16b, we can estimate the deposition rate of ^{210}Pb:

$$R^{\mathrm{Pb}} = \frac{A(N)}{M[\exp(-\lambda^{\mathrm{Pb}} N) - \exp(-\lambda^{\mathrm{Po}} N)]} \frac{\lambda^{\mathrm{Po}} - \lambda^{\mathrm{Pb}}}{\lambda^{\mathrm{Pb}}} \tag{6.17}$$

with N the number of days between the sample exposure and the start of a the sample measurement.

Table 6.6 presents the results on the upper limits for both R^{Po} and R^{Pb}. The measured activity A is the upper limit from equation 6.10 converted to mBq. With the increase of the time between the sample exposure and its measurement, the limits on ^{210}Po become weaker since the ^{210}Po decays, while the ones on ^{210}Pb become stronger since ^{210}Pb has time to increase.

The evolution of the best constrain of R^{Pb} compared to N is shown in figure 6.21. R^{Pb} is improving constantly and reaches a minimum of 225 mBq/m^{2}day around $N = 880$ days. At this point, the ^{210}Po decay takes over, making the limit worse.

Table 6.6.: Upper limits on the deposition rates of ^{210}Po and ^{210}Pb.

Sample	Threshold (mBq/m^2)	Exposure (M) (days)	N (days)	R^{Po} (mBq/m^{2}day)	R^{Pb} (mBq/m^{2}day)
MPIK Desk Blank #1	470	131	188	< 14	< 350
Water tank (stairs)	470	131	200	< 14	< 340
Water tank (PMT)	470	131	214	< 16	< 320
UG cleanroom (door)	470	131	221	< 16	< 320
UG cleanroom (opposite)	470	131	228	< 17	< 310
MPIK Desk Blank #2	470	131	257	< 19	< 300

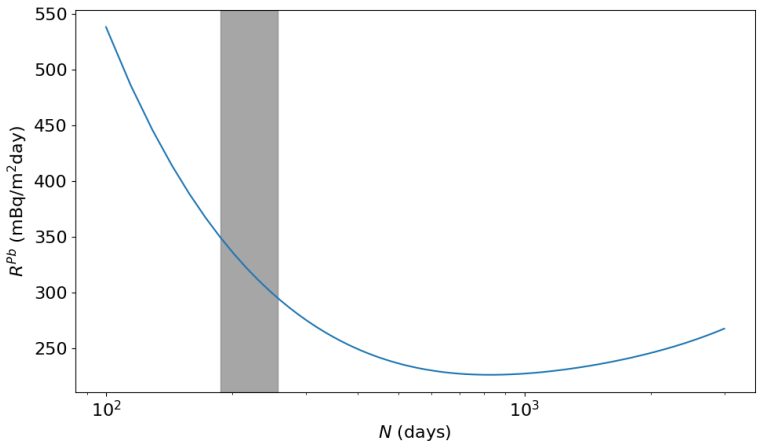

Figure 6.21.: Evolution of R^{Pb} as a function of N. The best possible constrain comes for measuring a sample after 880 days and it is 225 mBq/M^{m}day. The grey shaded area shows the time span of when the samples were measured for this work.

6.6 Summary and Outlook

In this chapter, the measurement of long-lived ^{222}Rn daughters was described using an alpha particle detector. The deposition rate on PTFE was constrained after more than 4 months exposure to:

- ^{210}Po-only deposition hypothesis: $< 14 - 19$ mBq/ m^{2}day
- ^{210}Pb-only deposition hypothesis: $< 300 - 350$ mBq/ m^{2}day

This study shows that there is no measurable contamination coming from storing PTFE in a cleanroom environment. The constraints on ^{210}Pb are weaker compared to the ones on ^{210}Po due to the long half-life of ^{210}Pb. The estimated activity in ^{210}Po in XENON1T is $\mathcal{O}(10\mathrm{mBq/m^2})$[106]. Using this value as a benchmark, we can affirm that storing PTFE does not add a sizeable amount of radioactive contamination for ^{210}Po. Unfortunately the weaker constraints on ^{210}Pb do not allow for a conclusive statement.

These limits can be improved by a dedicated background reduction. From the PIN diode specifications we expect only ~ 1 event per day in the ROI, which would mean a factor ~ 10 improvement on the sensitivity for both ^{210}Po and ^{210}Pb. The least problematic background is the ^{210}Po contamination on the diode itself, as explained in section 6.3. This decaying backgorund is well-constrained by the fit and its contribution to the error is sub-dominant. After eliminating this background, there are 15 to 20 events per day which can have two possible origins:

- The aluminum foil used to cover the shields.
- The PTFE itself. This hypothesis at least partially confirmed due to the fact that flipping a sample side changes the measured activity.

If we assume that all the excess events come from the PTFE, we have a final activity between 250 and 370 mBq/m^2, depending on the side. Compared to the ^{210}Po activity in XENON1T, which was between 6 and 22.4 mBq/m^2[106], the PTFE used in this work is much dirtier in either ^{210}Po or ^{210}Pb. For future measurement, one would need to screen and select the PTFE in advance, as it was done for XENON1T. For future detectors like DARWIN, ideally one would prepare and clean extra PTFE, so that the sample reflects exactly the one used for building the detector.

The setup is also promising in differentiating the contamination that comes from the surface and the one from the bulk of the PTFE. This can be used to screen for bulk-clean PTFE samples and test surface treatments to reduce further the ^{210}Po contamination.

Finally, the vacuum evaporation and deposition of ^{210}Po are confirmed. This phenomenon means that storing PTFE in vacuum has the risk of contaminating it with ^{210}Po if a source is present in the same environment. For these purposes, it is safer to employ a protection gas, like radon-clean air or nitrogen. A more dedicated study could be done for quantifying the phenomenon. Due to the fact that a strong ^{210}Po source would contaminate the PIN diode, one could create a dedicated vacuum vessel with the ^{210}Po source and several uncontaminated samples. By collecting and measuring the samples at different time, it is possible to construct a time profile of the ^{210}Po deposition. Finally, this study focussed on PTFE, but one should also see if the ^{210}Po vacuum deposition can happen for other important materials used in a TPC, such as stainless steel or copper.

Appendices

Appendix A

Calibration gases

Here is a collection of calibration gases used during this work. They were provided by AirLiquide. They have a shelf-time of 1 to 2 years, so several of them were used in this work. After their expiration date, they can still be used for qualitative analysis.

Table A.1.: Calibration gas #1. Base: helium 4.6

Component	**Concentration (ppm)**
Hydrogen	5.00 ± 0.15
Methane	5.50 ± 0.11
Nitrogen	11.4 ± 1.1
Oxygen	9.77 ± 0.29
Argon	5.1 ± 0.1
Carbon monoxide	4.881 ± 0.098
Krypton	11.60 ± 0.23
Xenon	5.38 ± 0.11

Table A.2.: Calibration gas #2. Base: helium 6.0

Component	**Concentration (ppm)**
Nitrogen	5.84 ± 0.58
Oxygen	5.06 ± 0.15
Krypton	5.99 ± 0.12

Table A.3.: Calibration gas #3. Base: helium 6.0

Component	**Concentration (ppm)**
Nitrogen	6.5 ± 0.7
Oxygen	5.73 ± 0.17
Krypton	6.21 ± 0.12

Table A.4.: Calibration gas #4. Base: helium 6.0

Component	**Concentration (ppm)**
Hydrogen	5.01 ± 0.15
Nitrogen	6.57 ± 0.66
Oxygen	4.92 ± 0.15
Krypton	4.871 ± 0.097

Appendix B

Unbiased estimate of the variance of a weighted mean

We have n independent measurements, distributed according to an unknown distribution Y with $E[Y] = \mu$ and $\mathrm{Var}[Y] = \sigma^2$. The weighted mean is also a random variable which has a distribution $X = \sum_i w_i X_i$. $E[X] = \sum_i w_i E[X_i] = \mu$ and $\mathrm{Var}[X] = \sum_i w_i^2 \mathrm{Var}[X_i] = \sigma^2 \sum_i w_i^2$.

We can define the estimator for μ as

$$\hat{\mu} \coloneqq \sum_i w_i x_i \tag{B.1}$$

with $\sum_i w_i = 1$. This estimator is unbiased, as

$$E[\hat{\mu}] = \sum_i w_i E[x_i] = \mu = E[X] \tag{B.2}$$

The general sample variance formula

$$\hat{\sigma}^2 \coloneqq \sum_i w_i (x_i - \hat{\mu})^2 \tag{B.3}$$

is however biased. To see this, we calculate

$$E[\hat{\sigma}^2] = \sum_i w_i E[(x_i - \hat{\mu})^2] = \sum_i w_i E\Big[\Big(\sum_j w_j (x_i - x_j)\Big)^2\Big] \tag{B.4}$$

We can write the argument of the expectation value

$$\Big(\sum_j (x_i - x_j)\Big)^2 = \sum_{j,k} w_j (x_i - x_j) w_k (x_i - x_k) = \sum_j w_j^2 (x_i - x_j)^2 + \sum_{j \neq k} w_j w_k (x_i - x_j)(x_i - x_k)$$

Passing the expectation value, the first term will become

$$E\Big[\sum_j w_j^2(x_i - x_j)^2\Big] = E[(x_i - x_j)^2] = 2E[x_i^2] - 2\mu^2 = 2\sigma^2$$

and the second

$$E\Big[\sum_{j\neq k} w_j w_k(x_i - x_j)(x_i - x_k)\Big] = E[x_i^2 - x_i x_j - x_i x_k + x_j x_k] = E[x_i^2] - \mu^2 = \sigma^2$$

Putting everything together

$$E[\hat{\sigma}^2] = \sum_i w_i\Big(2\sigma^2 \sum_{i\neq j} w_j^2 + \sigma^2 \sum_{i\neq j\neq k} w_j w_k\Big) = \sigma^2(1 - \sum_j w_j^2) \tag{B.5}$$

which shows that $E[\hat{\sigma}^2]$ is a biased estimator for σ. To get the unbiased estimator, we can divide for the extra term

$$\hat{\sigma}_u^2 \coloneqq \frac{\hat{\sigma}^2}{(1 - \sum_i w_i)} = \frac{\sum_i w_i(x_i - \hat{\mu})^2}{(1 - \sum_i w_i)} \tag{B.6}$$

List of Figures

List of Tables

List of Abbreviations

ΛCDM model Lambda cold dark matter model

APIMS Atmospheric pressure ionization mass spectrometry

BNC Bayonet Neill-Concelman connector

BPR Back pressure reducer

CMB Cosmic Microwave Background

DC Direct current

GC Trace GC Ultra

GXe Gaseous xenon

LHC Large Hadron Collider

LXe Liquid xenon

MFC Mass flow controller

MIM Multiple ion monitor

nEDM Neutron electric dipole moment

p.d.f. probability density function

PDD Pulse discharge detector

PMT Photo multiplier tube

PTFE Polytetrafluoroethylene

PTR Pulse-tube refrigerator

QCD Quantum chromodynamics

QMS quadrupole mass spectrometer

RF Radio frequency

ROI Region of Interest

SEM Secondary electron multiplier

SM Standard Model of Particle Physics

TPC Time Projection Chamber

WIMP Weakly Interactive Massive Particle

Acknowledgments

As for every human activity in the past 300,000 years, this work would not have been possible without the help of many people that surrounded me. Listing everyone is not possible, but I will try to do my best.

Foremost, I would like to thank Prof. dr. dr. h. c. Manfred Lindner for giving me a chance to work on this phd. It was a pleasure and privilege to work in his division at MPIK. It allowed me to pursue a long child dream of mine - find dark matter. And even though so far no dark matter is detected, I still had the chance to fulfill smaller dreams, like travel in an elevator with open doors and see what is behind the iron doors in the Gran Sasso tunnel. I would also like to thank Jun.-Prof. Dr. Loredana Gastaldo for agreeing to correct my thesis.

I would like to thank dr. Hardy Simgen. Without his help and guidance this work would not have been possible. I am particularly greatful that he never complained once even when I was stalking him outside the door of his office. I would also like to thank priz. doz. dr. Teresa Marrodan Undagoita for her help and support. Many thanks are also to dr. Stefan Bruenner and dr. Constanze Hasterok, whose projects are the starting point of this work. I would also like to thank Hardy, Dominick, Quim and Daniel for their help with the corrections.

Many thanks to all the XEMPI group: the ones still there, Dominick, Florian, Luisa, Mona, Andrii, Tim and Quim; and the ones who left, Sebastian, Stefan, Constanze, Guillaume, Daniel, Natascha. The nuclear bomb coffee discussions are a big part of my experience.

The experimental setup of this thesis would not have been possible to construct without the help of the technical team at MPIK: Benjiamin Gramlish, Steffen Form, Michael Reissfelder and Jonas Westermann. Many thanks also to the xenon collaboration, for the thrills and spills of doing science. It always made me feel at home with its loud atmosphere.

A huge thank goes to my friends, who gave me an amazing time in Heidelberg. I would like to thank present and past flatmates, Benni and Eleonora, who never complained for my lack of cleaning when close to a deadline. Many thanks go to Gianluca, Michaela, Ricardo and Sebastian and Leo. I would also like to thank the far away friends, Alessio and Hyoyin, with the hope that, as travelling becomes easier, we can meet again soon.

Finally, I would like to thank my family, my three siblings and my thirteen cousins. Finally, I would like to thank my parents and grandparents, without whom this journey would not have been started.

Bibliography

[1] Peter W. Higgs. "Broken Symmetries and the Masses of Gauge Bosons". In: *Phys. Rev. Lett.* 13 (16 1964), pp. 508–509. DOI: 10.1103/PhysRevLett.13.508.

[2] S. Chatrchyan et al. "Observation of a new boson at a mass of 125 GeV with the CMS experiment at the LHC". In: *Physics Letters B* 716.1 (2012), pp. 30–61. ISSN: 0370-2693. DOI: https://doi.org/10.1016/j.physletb.2012.08.021.

[3] G. Aad et al. "Observation of a new particle in the search for the Standard Model Higgs boson with the ATLAS detector at the LHC". In: *Physics Letters B* 716.1 (2012), pp. 1–29. ISSN: 0370-2693. DOI: https://doi.org/10.1016/j.physletb.2012.08.020.

[4] F. Zwicki. "Spectral displacement of extra galactic nebulae". In: *Helv. Phys. Acta.* 111.6 (1933).

[5] K. G. Begeman, A. H. Broeils, and R. H. Sanders. "Extended rotation curves of spiral galaxies - Dark haloes and modified dynamics". In: *Monthly Notices of the Royal Astronomical Society* 249 (1991), pp. 523–537.

[6] Douglas Clowe et al. "A direct empirical proof of the existence of dark matter". In: *The Astrophysical Journal* 648 (2006), pp. L109–L113.

[7] *Artistic image of the bullet cluster*. NASA. URL: http://apod.nasa.gov/apod/ap060824.html.

[8] D. J. Fixsen. "The Temperature of the Cosmic Microwave Background". In: *The Astrophysical Journal* 707 (Dec. 2009), pp. 916–920.

[9] C. L. Bennett et al. "Nine-year Wilkinson Microwave Anisotropy Probe (WMAP) Observations: Final Maps and Results". In: *The Astrophysical Journal* 208, 20 (2013).

[10] Nabila Aghanim et al. "Planck 2018 results-VI. Cosmological parameters". In: *Astronomy & Astrophysics* 641 (2020), A6.

[11] Timothy Clifton et al. "Modified gravity and cosmology". In: *Physics reports* 513.1-3 (2012), pp. 1–189.

[12] V. Springel, C. S. Frenk, and S. D. M. White. "The large-scale structure of the Universe". In: *Nature* 440.7088 (2006), pp. 1137–1144.

[13] Y. Fukuda et al. "Evidence for oscillation of atmospheric neutrinos". In: *Phys. Rev. Lett.* 81 (1998), pp. 1562–1567.

[14] Nathalie Palanque-Delabrouille et al. "Neutrino masses and cosmology with Lyman-alpha forest power spectrum". In: *Journal of Cosmology and Astroparticle Physics* 2015.11 (2015), p. 011.

[15] Stefano Gariazzo et al. "Light sterile neutrinos". In: *Journal of Physics G: Nuclear and Particle Physics* 43.3 (2016), p. 033001.

[16] G. Bertone. *Particle Dark Matter*. Cambridge University Press, 2010.

[17] Jonathan L Feng. "Dark matter candidates from particle physics and methods of detection". In: *Annual Review of Astronomy and Astrophysics* 48 (2010), pp. 495–545.

[18] Felix Kahlhoefer. "Review of LHC dark matter searches". In: *International Journal of Modern Physics A* 32.13 (2017), p. 1730006.

[19] Jennifer M Gaskins. "A review of indirect searches for particle dark matter". In: *Contemporary Physics* 57.4 (2016), pp. 496–525.

[20] Teresa Marrodan Undagoitia and Ludwig Rauch. "Dark matter direct-detection experiments". In: *Journal of Physics G: Nuclear and Particle Physics* 43.1 (2015), p. 013001.

[21] E. Aprile et al. "Dark Matter Search Results from a One Ton-Year Exposure of XENON1T". In: *Phys. Rev. Lett.* 121 (11 2018), p. 111302. DOI: 10.1103/PhysRevLett.121.111302.

[22] R.D. Peccei and Helen Quinn. "CP Conservation in the Presence of Pseudoparticles". In: *Physical Review Letters - PHYS REV LETT* 38 (June 1977), pp. 1440–1443. DOI: 10.1103/PhysRevLett.38.1440.

[23] C. Abel et al. "Measurement of the Permanent Electric Dipole Moment of the Neutron". In: *Phys. Rev. Lett.* 124 (8 2020), p. 081803. DOI: 10.1103/PhysRevLett.124.081803.

[24] F. Wilczek. "Problem of Strong P and T Invariance in the Presence of Instantons". In: *Phys. Rev. Lett.* 40 (5 Jan. 1978), pp. 279–282. DOI: 10.1103/PhysRevLett.40.279.

[25] Steven Weinberg. "A New Light Boson?" In: *Phys. Rev. Lett.* 40 (4 1978), pp. 223–226. DOI: 10.1103/PhysRevLett.40.223.

[26] Luca Di Luzio et al. "The landscape of QCD axion models". In: *Physics Reports* 870 (2020), pp. 1–117.

[27] H Primakoff. "Photo-production of neutral mesons in nuclear electric fields and the mean life of the neutral meson". In: *Physical Review* 81.5 (1951), p. 899.

[28] Peter W Graham et al. "Experimental searches for the axion and axion-like particles". In: *Annual Review of Nuclear and Particle Science* 65 (2015), pp. 485–514.

[29] 2021. URL: https://github.com/cajohare/AxionLimits.

[30] Kazuo Fujikawa and Robert E Shrock. "Magnetic moment of a massive neutrino and neutrino-spin rotation". In: *Physical Review Letters* 45.12 (1980), p. 963.

[31] Nicols Viaux et al. "Particle-physics constraints from the globular cluster M5: neutrino dipole moments". In: *Astronomy & Astrophysics* 558 (2013), A12.

[32] E. Aprile et al. "Excess electronic recoil events in XENON1T". In: *Phys. Rev. D* 102 (7 2020), p. 072004. DOI: 10.1103/PhysRevD.102.072004.

[33] Lutz Althüser. "Light collection efficiency simulations of the XENON1T experiment and comparison to data". MA thesis. WWU Münster, 2017.

[34] E. Aprile et al. "XENON1T dark matter data analysis: Signal reconstruction, calibration, and event selection". In: *Phys. Rev. D* 100 (5 2019), p. 052014. DOI: 10.1103/PhysRevD.100.052014.

[35] E Aprile and T Doke. "Liquid xenon detectors for particle physics and astrophysics". In: *Reviews of Modern Physics* 82.3 (2010), p. 2053.

[36] George Bakale, Ulrich Sowada, and Werner F Schmidt. "Effect of an electric field on electron attachment to sulfur hexafluoride, nitrous oxide, and molecular oxygen in liquid argon and xenon". In: *The Journal of Physical Chemistry* 80.23 (1976), pp. 2556–2559.

[37] J. Angle et al. "First Results from the XENON10 Dark Matter Experiment at the Gran Sasso National Laboratory". In: *Phys. Rev. Lett.* 100 (2008), p. 021303. DOI: 10.1103/PhysRevLett.100.021303.

[38] E Aprile et al. "Material screening and selection for XENON100". In: *Astroparticle Physics* 35.2 (2011), pp. 43–49.

[39] E. Aprile et al. "XENON100 Dark Matter Results from a Combination of 477 Live Days". In: *Phys. Rev. D* 94.12 (2016), p. 122001. DOI: 10.1103/PhysRevD.94.122001.

[40] J. Aalbers et al. "DARWIN: towards the ultimate dark matter detector". In: *JCAP* 11 (2016), p. 017. DOI: 10.1088/1475-7516/2016/11/017.

[41] Aprile, E. et al. "The XENON1T dark matter experiment". In: *Eur. Phys. J. C* 77.12 (2017), p. 881. DOI: 10.1140/epjc/s10052-017-5326-3.

[42] E. Aprile et al. "Search for Light Dark Matter Interactions Enhanced by the Migdal Effect or Bremsstrahlung in XENON1T". In: *Phys. Rev. Lett.* 123 (24 Dec. 2019), p. 241803. DOI: 10.1103/PhysRevLett.123.241803.

[43] E. Aprile et al. "Light Dark Matter Search with Ionization Signals in XENON1T". In: *Phys. Rev. Lett.* 123 (25 2019), p. 251801. DOI: 10.1103/PhysRevLett.123.251801.

[44] E. Aprile et al. "Search for inelastic scattering of WIMP dark matter in XENON1T". In: *Phys. Rev. D* 103 (6 Mar. 2021), p. 063028. DOI: 10.1103/PhysRevD.103.063028.

[45] E. Aprile et al. "Observation of two-neutrino double electron capture in 124Xe with XENON1T". In: *Nature* 568.7753 (2019), pp. 532–535. DOI: 10.1038/s41586-019-1124-4.

[46] Evan Shockley. "Study of Excess Electronic Recoil Events in XENON1T". PhD thesis. University of Chicago, 2020.

[47] E. Aprile et al. "XENON1T dark matter data analysis: Signal and background models and statistical inference". In: *Phys. Rev. D* 99 (11 2019), p. 112009. DOI: 10.1103/PhysRevD.99.112009.

[48] E. Aprile et al. "Projected WIMP sensitivity of the XENONnT dark matter experiment". In: *Journal of Cosmology and Astroparticle Physics* 2020.11 (Nov. 2020), pp. 031–031. DOI: 10.1088/1475-7516/2020/11/031.

[49] Dongming Mei and A. Hime. "Muon-induced background study for underground laboratories". In: *Phys. Rev.* D73 (2006), p. 053004.

[50] E. Aprile et al. "Conceptual design and simulation of a water Cherenkov muon veto for the XENON1T experiment". In: *JINST* 9 (2014), P11006. DOI: 10.1088/1748-0221/9/11/P11006.

[51] E. Aprile et al. "Lowering the radioactivity of the photomultiplier tubes for the XENON1T dark matter experiment". In: *The European Physical Journal C* 75.11 (2015), p. 546. DOI: 10.1140/epjc/s10052-015-3657-5.

[52] Aprile, E. et al. "Material radioassay and selection for the XENON1T dark matter experiment". In: *Eur. Phys. J. C* 77.12 (2017), p. 890. DOI: 10.1140/epjc/s10052-017-5329-0.

[53] S. Bruenner et al. "Radon daughter removal from PTFE surfaces and its application in liquid xenon detectors". In: *Eur. Phys. J. C* 81.4 (2021), p. 343. DOI: 10.1140/epjc/s10052-021-09047-2.

[54] E. Aprile et al. "Intrinsic backgrounds from Rn and Kr in the XENON100 experiment". In: *Eur. Phys. J. C* 78.2 (2018), p. 132. DOI: 10.1140/epjc/s10052-018-5565-y.

[55] E. Aprile et al. "Removing krypton from xenon by cryogenic distillation to the ppq level". In: *The European Physical Journal C* 77.5 (2017), p. 275. DOI: 10.1140/epjc/s10052-017-4757-1.

[56] E. Aprile et al. "Physics reach of the XENON1T dark matter experiment." In: *Journal of Cosmology and Astroparticle Physics* 2016.04 (2016), pp. 027–027. DOI: 10.1088/1475-7516/2016/04/027.

[57] V. Pizzella. "Purity control of the XENON1T gas inventory prior to initial filling and studies of mixing properties of impurities in gaseous xenon". MA thesis. Rome: Università degli studi di Roma Tor Vergata, 2016.

[58] E. Aprile et al. "^{222}Rn emanation measurements for the XENON1T experiment". In: *Eur. Phys. J. C* 81.4 (2021), p. 337. DOI: 10.1140/epjc/s10052-020-08777-z.

[59] E. Aprile et al. "Online ^{222}Rn removal by cryogenic distillation in the XENON100 experiment". In: *The European Physical Journal C* 77.6 (2017), p. 358. DOI: 10.1140/epjc/s10052-017-4902-x.

[60] U.S. Department of Commerce. *National Institut of Standard and Technology*. URL: https://webbook.nist.gov/chemistry/.

[61] C. Hasterok. "Gas Purity Analytics, Calibration Studies, and Background Predictions towards the First Results of XENON1T". PhD thesis. Heidelberg: Ruprecht-Karls-Universität, 2017.

[62] J.E. Campana. "Elementary theory of the quadrupole mass filter". In: *International Journal of Mass Spectrometry and Ion Physics* 33.2 (Mar. 1980), pp. 101–117.

[63] Raymond E. March. "Ion Trap Mass Spectrometers". In: *Encyclopedia of Spectroscopy and Spectrometry*. Oxford: Elsevier, 1999, pp. 1000–1009. ISBN: 978-0-12-226680-5. DOI: https://doi.org/10.1006/rwsp.2000.0143. URL: http://www.sciencedirect.com/science/article/pii/B0122266803001435.

[64] GW Goodrich and WC Wiley. "Continuous channel electron multiplier". In: *Review of Scientific Instruments* 33.7 (1962), pp. 761–762.

[65] *Channeltron electron multiplier handbook for mass spectrometry applications*. Burle.

[66] E. C. Horning D. I. Carroll I. Dzidic and R. N. Stillwell. *Atmospheric Pressure Ionization Mass Spectrometry*. Applied Spectroscopy Reviews, 1981. DOI: https://doi.org/10.1080/05704928108060409.

[67] Francis W. Karasek, Martin J. Cohen, and David I. Carroll. "Trace Studies of Alcohols in the Plasma Chromatograph-Mass Spectrometer". In: *Journal of Chromatographic Science* 9.7 (July 1971), pp. 390–392. DOI: 10.1093/chromsci/9.7.390. URL: https://doi.org/10.1093/chromsci/9.7.390.

[68] Hideki Harano and Chikara Ito. "Application of atmospheric pressure ionization mass spectrometry to cover gas analysis in fast reactors". In: *Nuclear Instruments and Methods in Physics Research Section A: Accelerators, Spectrometers, Detectors and Associated Equipment* 492.1-2 (2002), pp. 317–323.

[69] Rokibul Islam, Patrick D Pedrow, and Karl R Englund. "Phenomenology of corona discharge in helium admixtures inside a point-to-point electrode geometry". In: *IEEE Transactions on Plasma Science* 45.10 (2017), pp. 2848–2856.

[70] Kevin Siefering, Walter Whitlock, and Henry Berger. "Improved Atmospheric Pressure Ionization Mass Spectroscopic Methods: II. Extending the Range of Accuracy Through Nonlinear Calibration Techniques". In: *Journal of the Electrochemical Society* 140.4 (1993), p. 1165.

[71] URL: https://www.thermofisher.com/order/catalog/product/APIMSXANLYZ.

[72] David R. Whitfield. *private communication*. david.whitfield@thermofisher.com.

[73] URL: https://www.pfeiffer-vacuum.com/en/products/vacuum-generation/turbopumps/hybrid-bearing/hipace-80/.

[74] Katja Dettmer-Wilde and Werner Engewald. "Practical gas chromatography". In: *A Comprehensive Reference*. Springer, 2014, p. 902.

[75] URL: http://tools.thermofisher.com/content/sfs/brochures/Thermo-Scientific-TRACE-GC-Ultra.pdf.

[76] W.E. Wentworth, Huamin Cai, and Stanley Stearns. "Pulsed discharge helium ionization detector universal detector for inorganic and organic compounds at the low picogram level". In: *Journal of Chromatography A* 688.1 (1994), pp. 135–152. ISSN: 0021-9673. DOI: https://doi.org/10.1016/0021-9673(94)00913-9.

[77] URL: http://apnglobal.ca/wp-content/uploads/2018/05/DIAPHRAGM-VALVES-ELDV-MDVG-SERIES.pdf.

[78] *An Installer's Pocket Guide for VCR Metal Gasket Face Seal Fittings and Micro-Fit Weld Fittings*. Swagelok.

[79] Ivan Markovsky and Sabine Van Huffel. "Overview of total least-squares methods". In: *Signal processing* 87.10 (2007), pp. 2283–2302.

[80] URL: https://www.restek.com/globalassets/pdfs/literature/PCTS1472-UNV.pdf.

[81] D. Winkler. "Determination of the Krypton-Impurity Evolution in the XENON1T Detector and Optimization of Separation Columns for Krypton in Xenon Assays". MA thesis. Heidelberg: Ruprecht-Karls-Universität, 2020.

[82] A Curioni et al. "A regenerable filter for liquid argon purification". In: *Nuclear Instruments and Methods in Physics Research Section A: Accelerators, Spectrometers, Detectors and Associated Equipment* 605.3 (2009), pp. 306–311.

[83] Shigefumi Okada and Noriyuki Momoshima. "Overview of tritium: characteristics, sources, and problems." In: *Health physics* 65.6 (1993), pp. 595–609.

[84] Wolfango Plastino et al. "Tritium in water electrolytic enrichment and liquid scintillation counting". In: *Radiation Measurements* 42.1 (2007), pp. 68–73. ISSN: 1350-4487. DOI: https://doi.org/10.1016/j.radmeas.2006.07.010.

[85] Ch Zhang et al. "Cosmogenic activation of materials used in rare event search experiments". In: *Astroparticle Physics* 84 (2016), pp. 62–69.

[86] K. Jousten. *Handbook of Vacuum Technology*. Wiley-VCH, 2008.

[87] Yuichi Ishikawa and Vincenc Nemanič. "An overview of methods to suppress hydrogen outgassing rate from austenitic stainless steel with reference to UHV and EXV". In: *Vacuum* 69.4 (2003), pp. 501–512. ISSN: 0042-207X. DOI: https://doi.org/10.1016/S0042-207X(02)00562-6.

[88] R Calder and G Lewin. "Reduction of stainless-steel outgassing in ultra-high vacuum". In: *British Journal of Applied Physics* 18.10 (1967), pp. 1459–1472. DOI: 10.1088/0508-3443/18/10/313.

[89] M Bernardini et al. "Air bake-out to reduce hydrogen outgassing from stainless steel". In: *Journal of Vacuum Science & Technology A: Vacuum, Surfaces, and Films* 16.1 (1998), pp. 188–193.

[90] Paolo Chiggiato. "Materials and Properties IV Outgassing". In: *CERN Accelerator School (CAS) on Vacuum for Particle Accelerators* (2017).

[91] Aprile, E. et al. "Material radioassay and selection for the XENON1T dark matter experiment". In: *Eur. Phys. J. C* 77.12 (2017), p. 890. DOI: 10.1140/epjc/s10052-017-5329-0.

[92] International Atomic Energy Agency. *Chart of Nuclides*. URL: https://www-nds.iaea.org/ (visited on 2021).

[93] *The PIN diode circuit designers' handbook*. Microsemi-Watertown. 1998.

[94] P Pagelkopf and J Porstendörfer. "Neutralisation rate and the fraction of the positive 218Po-clusters in air". In: *Atmospheric Environment* 37.8 (2003), pp. 1057–1064. ISSN: 1352-2310. DOI: https://doi.org/10.1016/S1352-2310(02)00997-4.

[95] URL: https://www.ortec-online.com/-/media/ametekortec/other/introduction-charged-particle-detectors.pdf?la=en.

[96] URL: https://www.ortec-online.com/-/media/ametekortec/brochures/ultra.pdf?la=en&revision=09eb5ed1-936c-452e-90ee-c28506808499.

[97] Pablo Herrero Gomez. "Investigation of surface cleaning procedures for the removal of radon daughters from PTFE surfaces and their applicability in liquid xenon detectors." MA thesis. Heidelberg: Ruprecht-Karls-Universität, 2018.

[98] James F. Ziegler. "SRIM-2003". In: *Nuclear Instruments and Methods in Physics Research Section B: Beam Interactions with Materials and Atoms* 219-220 (2004). Proceedings of the Sixteenth International Conference on Ion Beam Analysis, pp. 1027–1036. ISSN: 0168-583X. DOI: https://doi.org/10.1016/j.nimb.2004.01.208.

[99] Florian Jörg. "Investigation of coating-based radon barriers and studies towards their applicability in liquid xenon detectors". MA thesis. Heidelberg: Ruprecht-Karls-Universität, 2017.

[100] Guillaume Eurin, Florian Jörg, and Hardy Simgen. "Production and characterization of a ^{226}Ra implanted stainless steel radon source". In: *in preparation* (expected 2021).

[101] B Eichler. *Volatility Properties of Polonium*. Tech. rep. Paul Scherrer Inst., 2002.

[102] Emilio Andrea Maugeri et al. "Adsorption of volatile polonium species on metals in various gas atmospheres: Part III–Adsorption of volatile polonium on stainless steel 316L". In: *Radiochimica Acta* 106.2 (2018), pp. 125–134.

[103] James M Goode. "Physical properties of polonium". In: *TID* (1956), p. 18.

[104] Tomasz Skwarnicki. "A study of the radiative CASCADE transitions between the Upsilon-Prime and Upsilon resonances". PhD thesis. Cracow, INP, 1986.

[105] H. Bateman. "Solution of a system of differential equations occurring in the theory of radioactive transformations". In: *Proc. Cambridge Philos. Soc* 15 (1910), pp. 423–427.

[106] N. Rupp. "Radon Induced Background in the XENON1T Dark Matter Search Experiment and Studies on Xenon Purity in the HeXe System". PhD thesis. Heidelberg: Ruprecht-Karls-Universität, 2021.